Technical Report of LCGT

10-August, 2005

LCGT Collaboration

]

LIGO-T050231-00-Z

Preface

During the period of constructing TAMA, the Japanese gravitational wave group began to study a plan for a large-scale interferometer succeeding the technique of TAMA. At the very beginning of the study, the basic idea of the interferometer was only to scale the baseline of TAMA up to 3 km. After a while, we decided to upgrade the target sensitivity by a cryogenic technique, and started R&D of the cryogenic mirror, where the basic idea was to extract heat by suspension fibers of the main mirror. The cryogenic technique had been experienced by elder researchers who developed the resonant antenna for the continuous gravitational wave signal from the Crab pulsar at KEK. Fortunately after two years of research, we found that the basic idea of cryogenic mirror is applicable to a practical interferometer. At this stage, the original plan of LCGT (Large-scale Cryogenic Gravitational wave Telescope) was established. The plan was approved by a Steering Committee of ICRR, the University of Tokyo and the action of demanding funds was initiated by the Institute in 1998. Also, the plan was announced in the Physics Community of Science Council of Japan, and widely introduced to neighboring communities of cosmic-ray physics. Finally the LCGT plan was recognized by the relevant committee of the academic advisory board under the Ministry of Education as a significant science project that requires prompt R&D. After this decision, we conducted much more practical R&D for LCGT and revised the original design according to R&D results. We now believe that we have already established the technology necessary for constructing LCGT.

KURODA, Kazuaki
The Project Leader of LCGT

Contents

1. Overview of LCGT

The objective of LCGT is to directly observe the gravitational wave signals that are produced by the coalescence of binary neutron stars more than once a year. According to a recent analysis of the occurrence rate of coalescence, the detectable range of LCGT should be more than 200 Mpc at its optimum angle arrangements of the inclination angle of the orbit, the polarization of the gravitational wave and the directivity angle of the propagation. Keeping this range in mind, we have designed LCGT that can be built by existing techniques. The main points of its design are:

- adopting a 3 km baseline
- utilizing a cryogenic mirror
- constructing an underground site
- two parallel interferometers installed in a vacuum chamber

Due to the limit of the scale of the underground site, we designed its baseline length to be 3 km. By utilizing a cryogenic mirror, we need to adopt sapphire as the mirror substrate material in place of synthetic silica that is widely used. Although there is an alternative substrate of calcium fluoride, it requires a lower temperature than sapphire to attain the target sensitivity, which is not acceptable due to the cooling power of refrigerators. The adoption of sapphire has let us determine the adoption of the Resonant-Sideband-Extraction (RSE) method with a Suspension Point Interferometer (SPI). The SPI is an insurance against a possible malfunction of the anti-vibration system due to the cryogenic system. Although the cooling efficiency increases by short and thick fibers that suspend the main mirror, mechanical isolation becomes better by long and thin fibers. Since the heat links are designed to touch an auxiliary mirror, which is located just above the main mirror, in order to extract heat produced in the main mirror, it is difficult to make small the mechanical noise directly introduced through these heat links. The working principle of the SPI has been confirmed by a prototype experiment. The RSE method also guarantees low-power heat production in the near mirrors while maintaining both a high optical power inside the cavities and leaving the frequency bandwidth unchanged. Since sapphire has a larger optical loss, it is important to decrease the optical power passing through the near mirror. Two parallel interferometers are installed in a vacuum chamber in order to remove fake events by the coincidence analysis of data. Since the stochastic noise is reduced by coherent observation, while assuming the independence of these interferometers, the detectable range can be scaled up by a square root of two for coalescence events.

The exact detectable range of one interferometer is 185 Mpc for the coalescence of binary neutron stars of 1.4 $M_{\odot}$ each with a signal-to-noise ratio of 10 averaging on directivity pattern, polarization, and the inclination angle of the orbit. Considering coherent observation, LCGT can detect events occurring at 257 Mpc in its optimum condition, which may produce 7.9-times the gravitational wave signal per year, assuming an occurrence frequency of 10^{-5} per galaxy such as ours.

2. Design Summary of LCGT

[Author: KURODA, Kazuaki]
ICRR, Univ. of Tokyo, Kashiwa, Chiba 277-8582

Early in 2004, TAMA [1], LIGO (with three interferometers) [2] and GEO [3] conducted their third collaborative observation with a time scale of two months. However, the ultimate sensitivity attained by these interferometers was not sufficient for the frequent detection of coalescence gravitational wave signals, because of the low occurrence rate, which is estimated to be 1-10 events per million years for such a matured galaxy as our own. TAMA can observe events occurring within our local group of galaxies by its design sensitivity. However, LIGO(I) and VIRGO [4] cover up to 20 Mpc, based on their design sensitivity (in Fig. 1).

Although LIGO has very recently improved its sensitivity to be close to the design value [5], we need to increase the sensitivity of the detector to detect more events, which can be attained by expanding its scope range to cover more galaxies in the remote universe.

The original design concept of LCGT was to increase the baseline length of TAMA by one order, and to decrease the displacement noise of the mirrors by one order both by cryogenics and by locating the detector underground in Kamioka mine. This original plan was revised so as to consider technical developments and the experience obtained in a series of data-taking runs by TAMA.

Cryogenic mirrors are adopted for the main cavities in the interferometer of LCGT. Unfortunately, in place of synthetic silica, sapphire crystal has to be used for the mirror substrate, which has a higher internal optical loss due to scattering and absorption [7]. This causes higher heat production inside the near mirror of the Fabry-Perot cavity. In order to reduce a problem arising from the higher optical loss inside the near mirror, we have applied the technique of the resonant sideband extraction (RSE) scheme [8] with a relatively low-power recycling gain. The other item that characterizes LCGT is the suspension point interferometer (SPI), which is insurance against a possible malfunction of the anti-vibration system according to the mechanical noise inevitably introduced by cooling heat links connected with the mirror suspension system [9].

The data collected by TAMA was usually contaminated by non-Gaussian noise, and many fake events resulted [10]. To reduce these fake events, two interferometers will be installed in the same vacuum system, which is a change of the previous revised design. [11] From the report of LIGO, Hanford, the cross talk of two interferometers in the same vacuum tube was not seriously large. Even if there is some correlation between the two interferometers in LCGT, the simulated rejection ratio about the known wave-form signal is practically high enough [12].

The cryogenic mirror allows us to design the sensitivity of the interferometer, limited only by quantum noises: shot noise and pressure noise of the photon recoil force. If we can establish this quantum-limited sensitivity, the sensitivity of the observational band is altered only by the signal bandwidth and the optical power in the cavity. By optimizing these two parameters, we can increase the detectable distance of the gravitational wave events of coalescences of a 1.4 $M_{\odot}$ neutron star binary with a signal-to-noise ratio of 10. Considering the achievable technical condition, we fixed the optimum point at a power of 780 kW and a signal bandwidth of 230 Hz, which are realized based on the parameters listed in Table 1. From the maximum detectable distance of 257 Mpc, in consideration of two identical interferometers, we modestly expect to observe 7.9 events per year for the recently revised occurrence rate of the coalescence [13].

Since two independent sets of interferometers are placed in a system comprising a vacuum chamber, optical beams are arranged so as not to interfere with each other, as shown in Fig. 2

Each interferometer consists of both an auxiliary (suspension point) interferometer and the main interferometer. In the main interferometer, a 150-W Nd:YAG laser source is introduced through two stages of mode cleaners to an RSE-type power-recycled Fabry-Perot-Michelson interferometer with a 3-km baseline length. A laser of much less power is used for the auxiliary interferometers. Four main mirrors and four auxiliary mirrors are made of sapphire crystal, and the main mirrors are cooled down to 20 K. Other optical pieces than these main and auxiliary mirrors are made of fused silica, and are maintained in vacuum chambers at room temperature. Figure 3 represents the noise limit attained by the design of the first phase. The sensitivity in the observation band is certainly limited only by photon quantum noises: photon shot noise and photon pressure recoil noise.

The cryogenic mirror is made of sapphire, and is suspended by sapphire fibers that extract heat produced at the mirror due to optical loss inside the mirror substrate. The near mirror produces more heat than the end mirror due to optical loss arising from the transmitted laser beam power, while the heat production due to optical loss at reflections is assumed relatively negligible. The suspension fibers are connected to an auxiliary mirror that is cooled down at 10 K. This auxiliary mirror is cooled by fine heat links made of pure aluminum fibers connected to an anchor point inside the inner radiation shield of 4 K in the cryostat. Since the heat conductivity

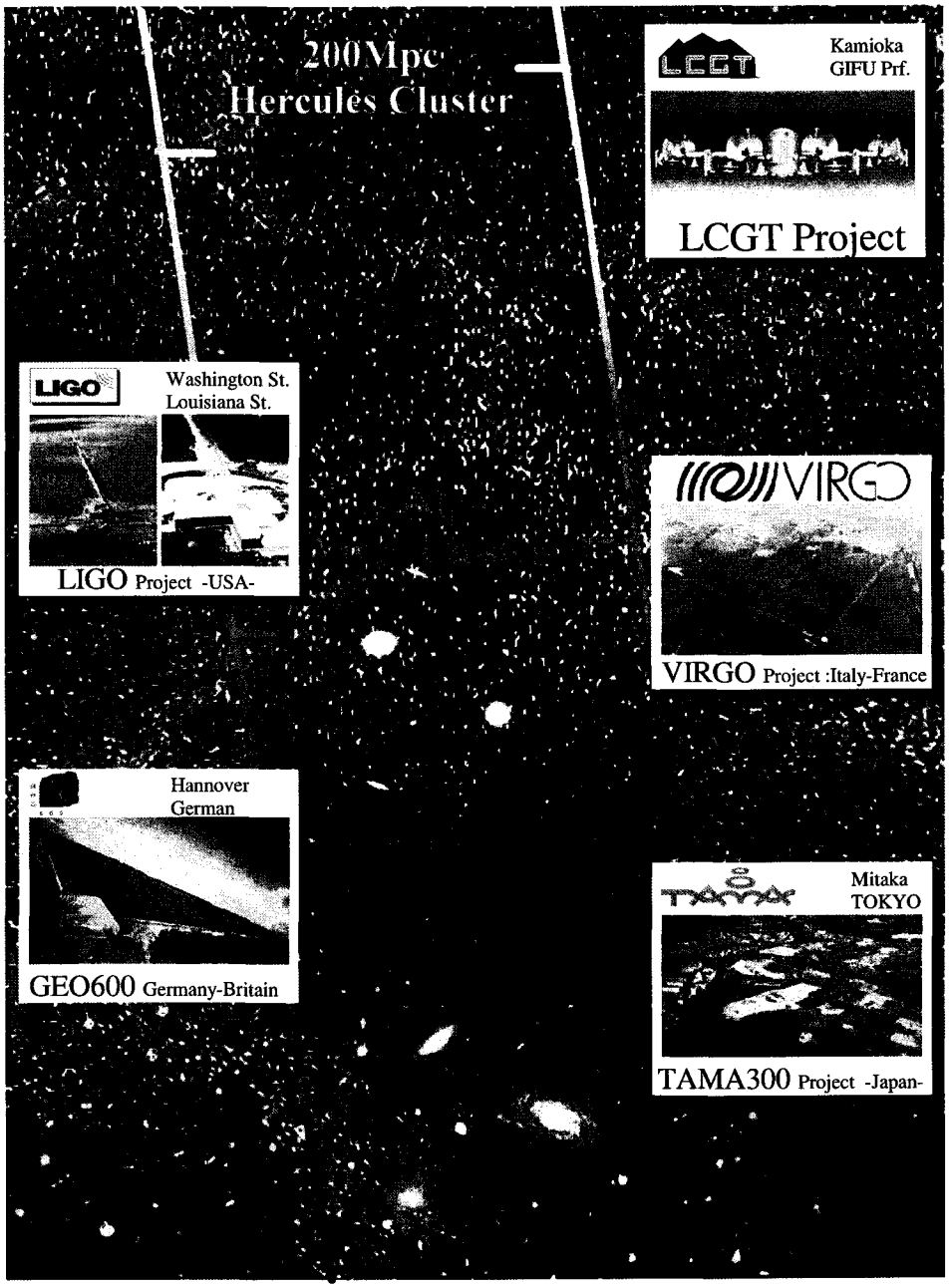

Fig. 1. The maximum scope range of the LCGT is 260 Mpc in terms of the detection of signals of the coalescence of binary neutron stars. LIGO(I) and VIRGO detectors cover up to 20 Mpc in their final sensitivities, whereas TAMA can see events occurring within our local group of galaxies based on its design sensitivity.

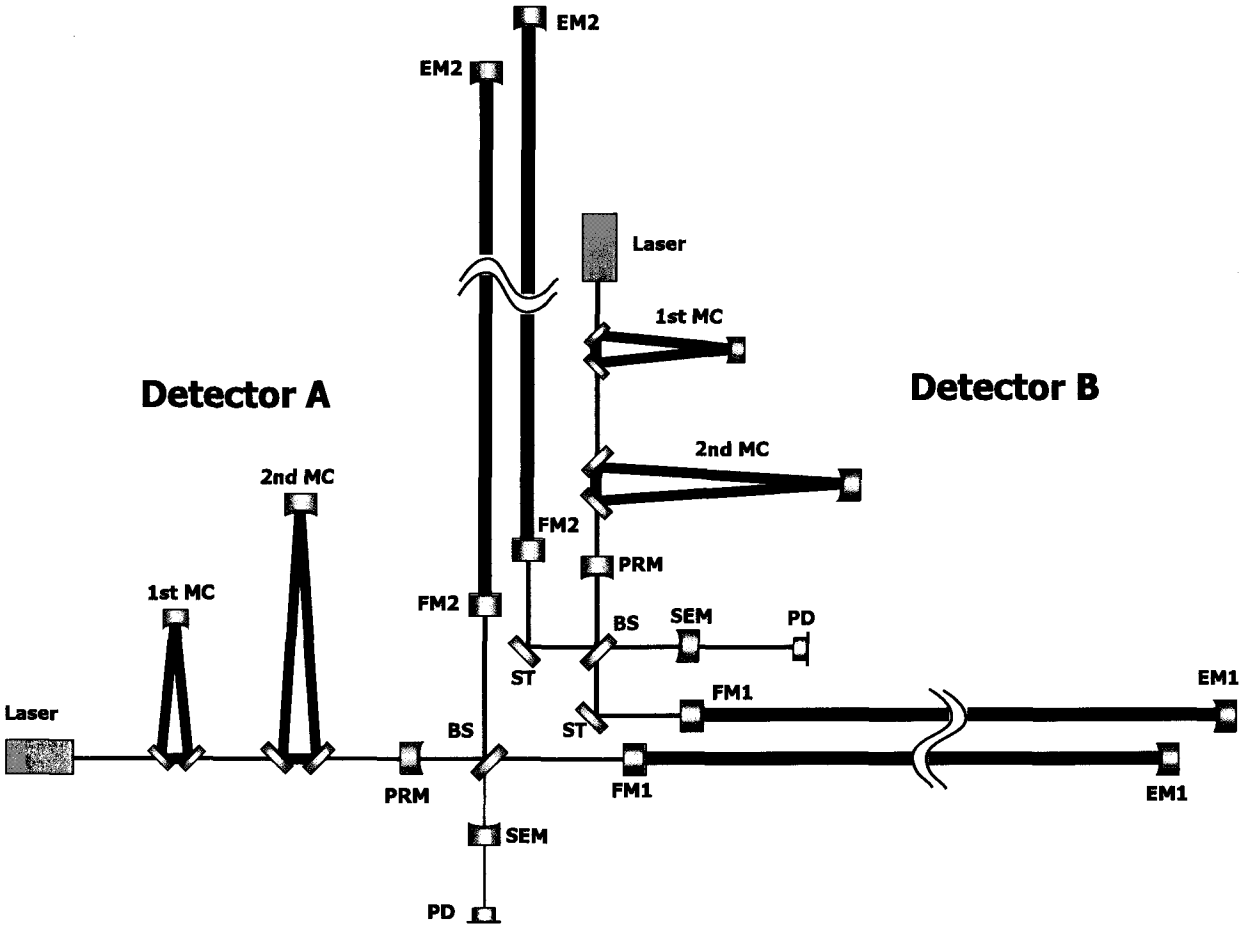

Fig. 2. Two interferometers (Detector A and Detector B) are placed in a system of the vacuum chamber. The beams moving towards a beam splitter from near mirrors in the Detector B are folded so as not to interfere with beams of the Detector B. The abbreviations are: MC, mode cleaner, PRM, power recycling mirror, BS, beam splitter, FM, front mirror, EM, end mirror, ST, steering mirror, SEM, signal extraction mirror.

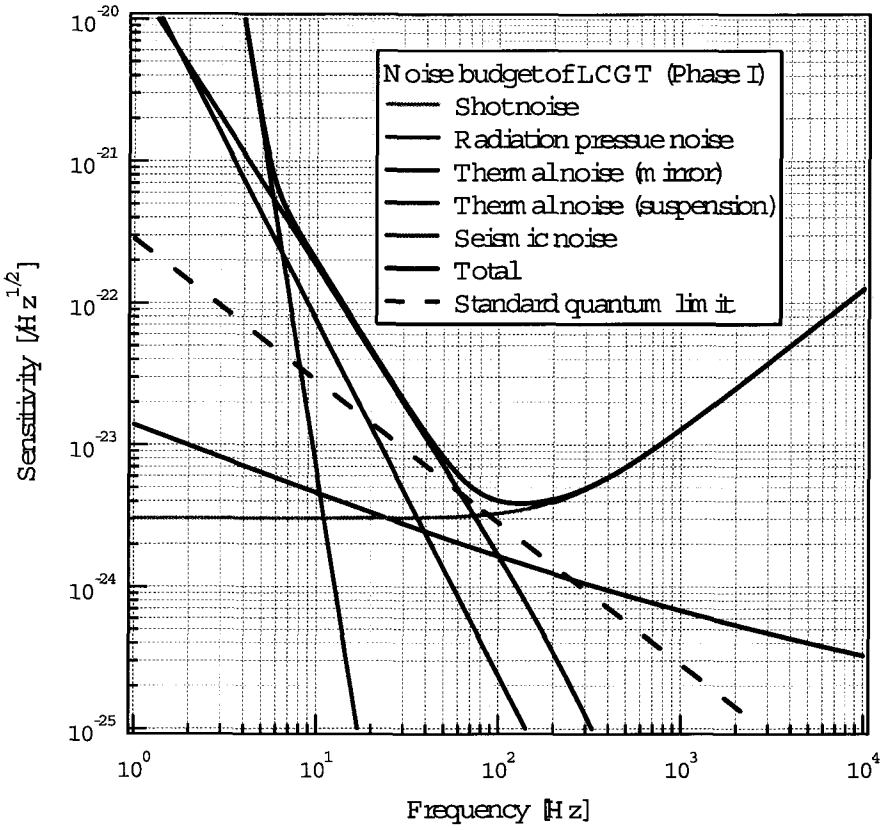

Fig. 3. Sensitivity curve of the first phase of LCGT. It is limited by quantum noises in the observational frequency range.

Table 1. Main parameters of the design of LCGT.

Item	Parameter
Baseline	3 km
Interferometer	Power recycled Fabry-Perot Michelson with RSE
Optical Power	Laser: 150 W, Input Power: 75 W, Cavity Finesse: 1550,
	Power Recycling gain: 11, Effective power: 780 kW
Signal bandwidth	230 Hz, Signal recycling gain: 15
Mirror	Diameter: 25 cm, Thickness: 15 cm
	Mass: 30 kg, material: Sapphire crystal
Pendulum	length: 40 cm, 4 sapphire fibers, 1.8 mm in diameter
Acoustic loss angle	Mirror internal: 1×10^{-8}, Pendulum: 2×10^{-7}
	Optical coating: 4×10^{-4}
Temperature	Mirror: 20 K, Suspension: 10 K (20 K for noise estimation)
Vacuum	$\leq 2 \times 10^{-7}$ Pa

of sapphire is optimum at around 20 K, the temperature of the main mirror is designed to be 20 K. The auxiliary mirror is suspended by heat-resistive wires through two-fold radiation shields from a control platform situated at room temperature in the common vacuum chamber. Heat production at the auxiliary mirror is negligible. The platform has adequate damping of the pendulum motion of the suspension system.

The interferometer system, the sensitivity of which is limited only by quantum noises, requires a highly sophisticated isolation system in addition to a suspension system of similar quality. According to the original grand design of the suspension and anti-vibration system, we install the suspension system into the cryostat and mount the seismic attenuation system (SAS) in the room-temperature vacuum chamber mounted over the cryostat. The prototype system of the SAS was originally developed at VIRGO [4] and later at CALTECH under collaboration with TAMA members [1].

A practical suspension system for testing this original design is applied to an one-hundred-meter cryogenic interferometer (CLIO project [15]) without the SPI system.

The design details, including a viewpoint of cost, are summarized here for the tunnel construction, the vacuum system and the cryostat with the suspension system, as follows:

1. Tunnel construction
   The interferometer is placed underground at Kamioka. The seismic noise underground is less by two orders of magnitude than at Mitaka, Tokyo (TAMA site), and we have confirmed that the site is suitable for stable operation of the interferometer [16]. A 3km×3km long tunnel will be dug, which will lie inside a mountain 1300 m high above sea level. The sea level of the tunnel is about 350 m. The mountain is composed of hard rock that contains zinc ore. Although there are several faults inside, the tunnel is stable and safe. The center room of the site is positioned horizontally, intruded from an access road at 350 m high above sea level. Both end rooms of the tunnel are designed to be not too far from the mountain slope side for convenient access to the tunnel. The dug tunnel will be reinforced by supporting steel bars anchored in the ceiling of the tunnel. Blasting concrete will be applied to the wall of the tunnel to prevent the rock surface from breaking down. The surface is to be finished by blast painting. The cost of the construction consists of mainly digging the tunnel.

2. Vacuum System
   To reduce the refractive fluctuation noise of the residual gas molecules, the vacuum pressure should be less than 10^{-6} Pa to achieve the design sensitivity. This vacuum pressure is not the ultimate value, but an achievable one utilized in advanced scientific instruments. However, the vacuum volume is extraordinarily large. Therefore, it is important to apply a baking procedure. If we adopt stainless steel, baking must be applied unless electro-chemical polishing is applied to the raw plates of the vacuum tubes. Electro-chemical buffing was used for the TAMA vacuum tubes, and we are confident that the gas-release rate of the surface has been effectively suppressed. However, it is not cost effective if we adopt this technique to the vacuum tubes of the LCGT, because of the speed of the process. We may need a very large facility that may not be used after the construction of LCGT. Therefore, baking is indispensable if we use stainless steel. On the other hand, titanium is an alternative material that has been in the spotlight recently as a vacuum material due to its better surface characteristics in spite of its high material cost. Its good quality reduces the baking process, and may also reduce the maintenance cost.

3. Cryostat and suspension
   Although the main mirrors are cooled at 20K, the

vacuum tubes are mainly held at room temperature. The mirror is housed in a cryostat with radiation shield tubes extending in the direction of both laser beams by more than 5 m long, which reduces the number of hot molecules coming from the vacuum tubes. Since two independent interferometers are installed in one vacuum system, four laser beams are passed inside the vacuum tube. Two of them are for the main interferometers and two of them are auxiliary ones (suspension point interferometers). We devised a vacuum system that can handle two independent interferometers without disturbing each other for maintenance. The design of the cryostat has been fixed, except for the details [17]. The prototype design of the cryogenic suspension system was tested at Kashiwa campus using a 7 m baseline cryogenic Fabry-Perot cavity. The detailed design of the suspension will be fixed by analyzing the result of the CLIO suspension system. The inner radiation shield is cooled by a pulse-tube refrigerator that has a cooling design power of 1 W at 4 K; the outer shield with extensions is cooled by another pulse-tube one that has a power of 30 W at 40 K.

Bibliography

[1] Ando M. *et al.*, 2001, Phys. Rev. Lett. **86**, 3950

[2] Abramovici A. *et al.*, 1992, *Science* **256**, 325

[3] Danzmann K. *et al.*, 1994, *Max-Plank-Institut fur Quantenoptik Report* (Garching, Germany), 190

[4] Bougleux E. *et al.*, 1998, Phys. Lett. A **409**, 480

[5] Rana Adhikari, 2005, *in the Fourth TAMA symposium*, Osaka, Japan

[6] Kuroda K. *et al.*, 1999, Int. J. Mod. Phys. D **8**, 557

[7] Tomaru T. *et al.*, 2001, Phys. Lett. A **283**, 80

[8] Mizuno J. *et al.*, 1993, Phys. Lett. A **175**, 273

[9] Aso Y., 2002 *Master Thesis* (The University of Tokyo)

[10] Tagoshi H., *et al.*, 2001, Phys. Rev. D **63**, 062001

[11] Kuroda K., *et al.*, 2003, Class. Quantum Grav. **20**, S871

[12] Kanda N.,2004, *in LCGT collaboration meeting*

[13] Kalogera V. *et al.*, 2004, Astrophysical J. **614**, L137

[14] Takamori A., 2003 *Doctoral Thesis* (University of Tokyo)

[15] Ohashi M, *et al.*, 2003, Class. Quantum Grav. **20**, S599

[16] Sato S, *et al.*, 2004, Phys. Rev. D, **69**, 102005

[17] Uchiyama T. *et al.*, 2004, Class. Quantum Grav. **21**, S1161

3. Data Analysis: Gravitational Wave Sources and Physics

[Author: KANDA, Nobuyuki]

Department of Physics, Graduate School of Science, Osaka City University

The main task of data analysis is to identify gravitational wave events in data streams. Search targets in first scientific operation of LCGT are gravitational waves from the coalescence of compact binaries, black-hole quasi-normal mode oscillation, stellar core-collapse, and pulsar and stochastic sources. (Figures 1 and 2).

Due to the weakness of gravitational waves, we must treat data carefully by searching for any small evidence of them. The search methods will be designed to achieve a higher signal-to-noise ratio (SNR) for true gravitational wave events. The evaluations of noise characteristics and systematic errors of detector instruments are also important to guarantee the robustness of searches and to determine the accuracy of waveform parameters. Moreover, two interferometers of LCGT promise better statistical treatments in event searches.

On the other hand, what kind of physics can be extracted from gravitational wave analysis is very interesting not only in fundamental physics, but also in astrophysics and astronomy.

We consider these key issues of data analysis in the following sections, according to the gravitational wave sources.

3.1. Inspiral Gravitational Waves from Binary Coalescence

The coalescence of compact star binaries, i.e. neutron-star pairs, black-hole pairs, or neutron star - black-hole pairs are promising sources of gravitational waves. The gravitational wave radiation will become to have a stronger amplitude and higher frequency as each rotating star drops to inner orbits. This is called binary *"inspirals"*. After closely approaching each other, stars will merge into one object. A complex gravitational wave will be radiated during this *"merger"* phase, the waveform of which is hard to analytically calculate. Finally, a black-hole or larger mass object will be formed.

In the inspiral phase, where stars are isolated each other, so as to be treated as a point-like object, the waveform is well predicted by the post-Newtoninan approximation. The gravitational wave amplitude and frequency evolution are well characterized by masses at the beginning. The matched-filter method is optimal filtering with a known waveform and with a known noise-power spectrum. Using the expected waveform template, $h(t)$, the correlation between the gravitational wave and the observed data, $s(t)$, can be given as

$$c(\tau) = (h,s) = 2\int \frac{\widetilde{h}^*(f)\cdot\widetilde{s}(f)}{S_h(f)}\,df \qquad (1)$$

	Range (SNR$\geq$ 10, 1.4-1.4$M_\odot$, optimal incident) [Mpc]	Expected Rate of Detection [events/yr]
single LCGT	185	$2.8\ ^{+7.2}_{-2.3}$
two LCGT	257	$7.9\ ^{+20.4}_{-6.5}$

Table 1. LCGT detectable range and expected number of events for binary coalescence.

where $\widetilde{h}(f)$ and $\widetilde{s}(f)$ are the Fourie transformation of $h(t)$ and $s(t)$, and $S_h(f)$ is the noise-power spectrum of the detector. If there is a gravitational wave in the data at t_0 in the time domain, $c(t_0)$ will have an excess in the time series. The signal-to-noise ratio (SNR) is just given as $c(t_0)$. To ensure the variation of polarizations of gravitational waves, we use the quadratic sum of two orthogonal bases, h_+ and $h_\times$, in inspiral gravitational wave search:

$$\begin{aligned}\rho(\tau) &= \sqrt{(h_+,s)^2+(h_\times,s)^2}\\ &= \sqrt{2}\ \mathrm{SNR}.\end{aligned} \qquad (2)$$

The possible detectable range of inspiral gravitational wave sources should be determined by the detector noise-power spectrum, $S_h(f)$. According to the LCGT design sensitivity, the detectable range, R_{max}, with SNR $\geq$ 10 for inspiral gravitational waves from 1.4-1.4$M_\odot$ neutron star binaries reaches 185 Mpc for a single interferometer. A coherent addition of two interferometer signals or a coincidence condition for noise suppression will extend the range to 257 Mpc. Figure 3 displays the detectable range for a single LCGT interferometer as a function of the star's mass in solar mass units. In this figure, we assume the optimal source location: zenith direction and optimal azimuth angle of polarization. In the case of binary inspiral gravitational waves, the whole sky root-mean-square range for source direction and polarization is analytically calculated as $0.4 \times R_{max}$. Also, a simulation adjudicates detection on the threshold estimates that the equivalent spherical volume of the search region is $\frac{4\pi}{3}(0.441... \times R_{max})^3$. Thus, the search volume is about 2.3×10^6[Mpc^3].

The rate of binary coalescence in the galaxy is estimated[1] as $83\ ^{+209}_{-56}$[events/Myr]. According to this and the number density of galaxies[2], the expected number of events in a single LCGT interferometer range is $2.8\ ^{+7.2}_{-2.3}$ events/year[3]. If we use the information from two detectors to extend the range, the rate is expected to be increased by $(\sqrt{2})^3$ times; $7.9\ ^{+20.4}_{-6.5}$ events/year.

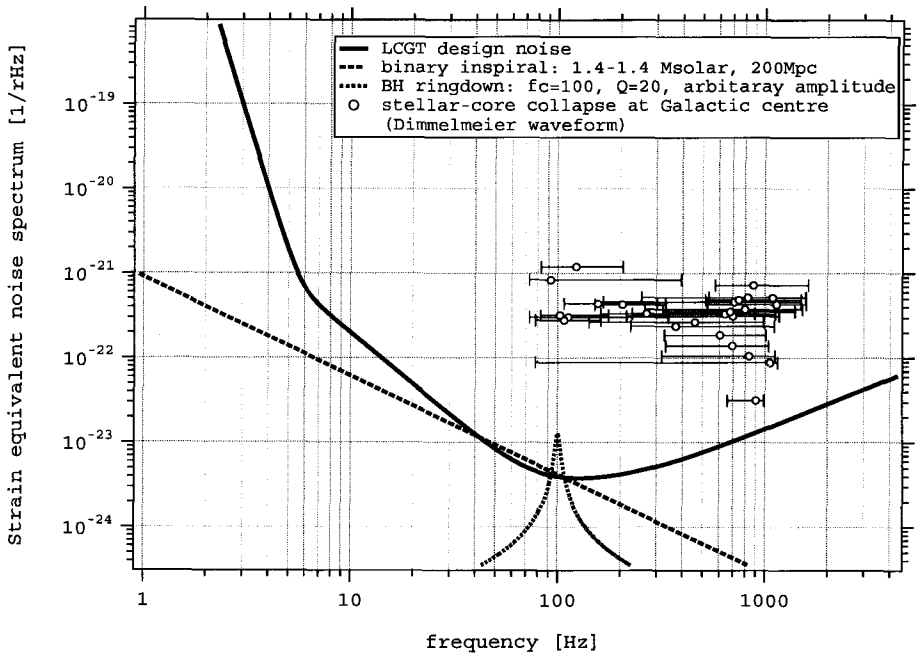

Fig. 1. LCGT Sensitivity and Gravitational Wave Sources. black solid line is the design noise of the LCGT interferometer. green dashed line is inspiral gravitational waves from $1.4 - 1.4 M_{\odot}$ binary from the optimal direction at 200 Mpc away. The brown dotted line is a gravitational wave from a black-hole quasi-normal mode ringdown with Q=100 and an arbitrary amplitude. The red dots are burst gravitational waves from stellar-core collapse, h_{RSS}, using the Dimmelmeier waveform. The blue points are known pulsar's, h, with 1 year integration of the theoretical maximum allowed amplitude.

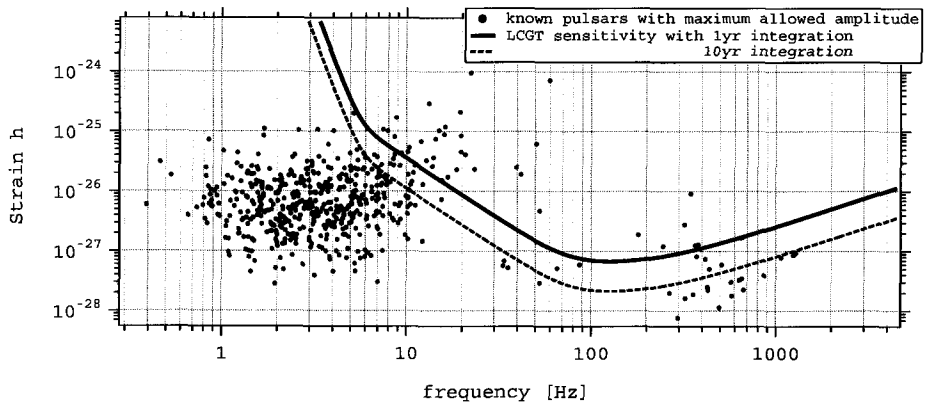

Fig. 2. LCGT sensitivity and known pulsars. The blue points are known pulsarsf theoretical maximum allowed amplitude of gravitational wave radiation. The black solid line displays the LCGT strain sensitivity for 1 year of integration, and the dashed line is 10 years of integration.

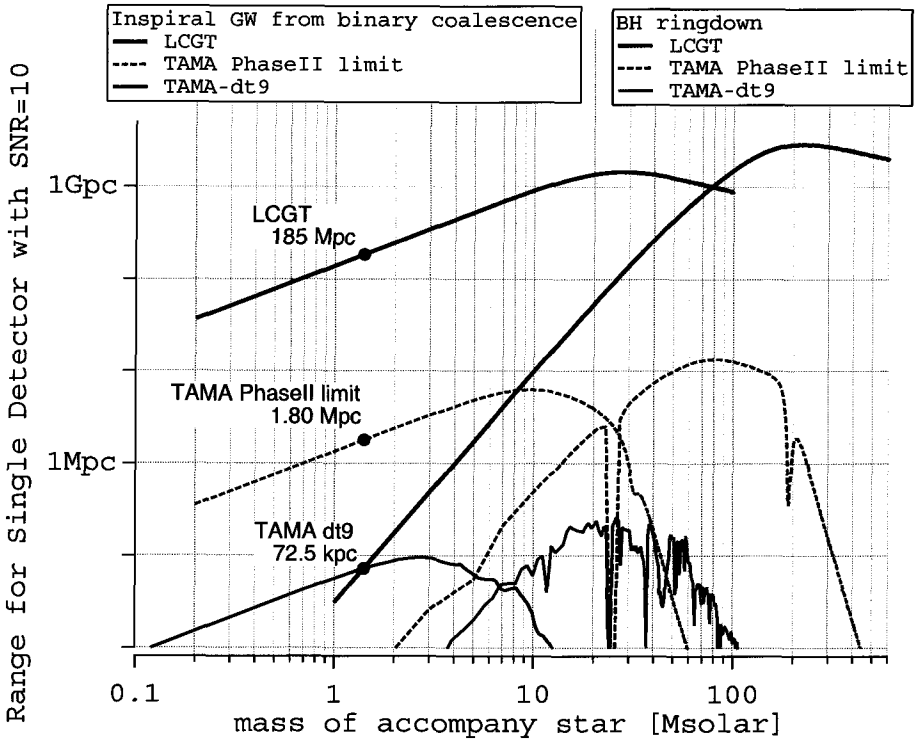

Fig. 3. Detectable range with SNR=10 of a single LCGT interferometer for the optimal incident direction

Physics on binary coalescence investigates strong gravitational fields, and the studies for dynamics of binary systems and compact objects. We can extract t knowledge about the masses, angular momentum, radius of neutron stars, viscosity of neutron stars, equation of state etc. For example, recently the formation of a hypermassive neutron star after the merging of a binary is expected based on a numerical study[4]. It is possible to confirm such a dynamical formation of a binary system when we detect inspiral gravitational waves.

If we succeed to resolve the polarization and absolute amplitude of a gravitational wave (in collaboration with the international network of detectors), they would determine the distance to the binary. With many events, the determination of the Hubble parameter or some other consistency check of gravitational wave propagation might be expected.

In searches for the inspiral gravitational wave events, we try to find the best matching for a bank of templates with the variations of source parameters. The required number of templates, N_{temp}, and the CPU computing power, P_{comp}, depend on the search parameter region[5]: smallest mass, m_{min}, minimal match SNR, MM, best sensitivity frequency, f_0, frequency cut-off lower side, f_s, and higher side, f_u. These are scaled as follows:

$$N_{temp} \sim (1-MM)^{-1}\, m_{min}^{-8/3}\, f_0^{-8/3}, \quad (3)$$

$$P_{comp} \sim (1-MM)^{-1}\, m_{min}^{-8/3}\, f_0^{-5/3}, \quad (4)$$

If we choose the smallest mass of a search as $N_{temp} \sim 1.0 M_\odot$, the required number of templates is 9.7×10^4 and $P_{comp} \sim 1.2 \times 10^{11}$ flops with χ^2 statistical testing. Therefore, we need to prepare ~ 1 Tflops of computing power for real time processing to independently analyze the output from the two interferometers of LCGT.

3.2. Ringdown Gravitational Waves from Black-Hole Quasi-Normal Mode

Perturbation theory around a black-hole predicts gravitational wave emission from the quasi-normal mode of the black-hole. The waveform is predicted to be dumped sinusoidal, which is characterized by the mass and Kerr parameter of the black-hole,

$$h(t) \propto \exp\left(-\frac{\pi f_c}{Q}(t-t_0)\right)\sin\left(2\pi f_c(t-t_0)+\phi_0\right), \quad (5)$$

where f_c, Q, ϕ_0, t_0 are the central frequency, the quality factor of the ringing, the initial phase, and the arrival time, respectively. Echeverria have given analytic expressions for f_c and Q as functions of the black hole mass, M, and the non-dimensional angular momentum (the Kerr parameter), $a = [0,1)$,, as [6]

$$f_c\,[\mathrm{kHz}] \simeq 32\left(\frac{M}{M_\odot}\right)^{-1} \times \left[1-\alpha(1-a)^\beta\right], \quad (6)$$

$$Q \simeq 2(1-a)^\gamma, \quad (7)$$

where $\beta = 3/10, \gamma = -9/20$ and $\alpha = 63/100$. These expressions give ring-down parameters (f_c, Q) with accuracies of $\sim 5\%$. For black holes with masses of $10 \sim 200 M_\odot$, the ringdown frequencies fall in the observational band 100Hz $\sim$ kHz of ground-based laser interferometric detectors. The matched filtering technique is useful to find ring-down signals in the outputs of gravitational wave detectors since their waveforms are modeled in a simple form as anequation (5) in terms of the parameters (f_c, Q) that can be easily converted into the black hole parameters (M, a).

The search range for ring-down gravitational waves from the black-hole quasi-normal mode strongly depends on the amplitude of the waves, which cannot be predicted by perturbation theory. Assuming a 3% fractional energy of the black-hole mass radiates as gravitational waves[7], LCGT is capable to detect beyond 1 Gpc away, around $100 M_\odot$, as displayed in Figure 3.

Ring-down waveform detection will give a new window as "black-hole mass spectroscopy". The accuracy of the mass and Kerr parameters is enough good to be studied. For example, the mass parameter accuracy is $\Delta M/M \simeq$ a few - 20% in the typical case[10]. This is remarkably good, compared with those estimated dynamically for know black-hole candidates in X-ray observations, $10 \sim 100\%$.

The template-banks are proposed references [8][9], and $\sim 10^3$ templates are required to search with a minimal match of $\leq 2\%$. The calculation cost is smaller than that for inspiral search, since its waveform (template) is shorter in the time domain. Using the 2.5 GHz Pentium IV processor, the research at TAMA gives a calculation time for 1000 hours of data as an empirical relation;

$$T_{1000\text{hours}} = 6.5 \left(\frac{N_{temp}}{682}\right) \left(\frac{16}{N_{\text{CPU}}}\right) [\text{days}], \quad (8)$$

where N_{CPU} is the number of CPU.

3.3. Burst Gravitational Wave

The "burst" gravitational waves are expected to be short transient gravitational waves from some candidate sources: supernovae, stellar-core collapse, black-holes, cusps of cosmic string, and so on. Since most of the scenario of burst sources does not predict an exact and generic gravitational waveform, burst-wave searches are made by a kind of excess filter of power, slope filter of the signal, or time-frequency spectrogram etc.

In another case, the search is checked by an anomaly of signals at an external trigger by other observations; e.g., gamma ray bursts, neutrino detectors, etc. In the meaning of coincidence with non-gravitational wave observations, the burst-wave search is important to establish credible detection of some evidence of gravitational waves.

The LCGT sensitivity is sufficient to detect burst gravitational waves from a stellar-core collapse in our galaxy. A numerical estimation of the waveforms[11] predicted $h \sim 10^{-20}$ in 100-1000 Hz for sources 10 kpc away. Figure 1 shows the expected burst signal, h_{RSS}, at the galactic center.

These predictions suggest that the burst waves are not only strong enough to be detected, but are also reliable enough to confirm the relativistic effect on the core dynamics.

3.4. Continuous Gravitational Wave Radiation

Pulsars might emit continuous gravitational waves according to their rotation, if the star has a local distortion of the form, precession, accretion gas, or has an R-mode radiation. Since the frequency of gravitational waves is expected to be twice (or higher harmonics) of the pulsar self-rotating period, it is able to search gravitational waves for known pulsars.

Considering known pulsars with its period P and spin-down rate $\dot{P}$, we expect the theoretically allowed maximum amplitude of gravitational radiation. Figure 2 shows the known pulsars and their maximum expected h with the integration 1 year of data. Table 2 lists the candidates of pulsars that radiate detectable gravitational waves. If these radiate the allowed maximum amplitude, LCGT can detect them with SNR ≥ 10 with one year of observation[12]. If there is no evidence, LCGT may give the upper limit of h as $10^{-27} \sim 10^{-26}$.

Pulsar	dist. [kpc]	freq [Hz]	h upper limit with 1 year of LCGT
Crab	2.0	60	1.1×10^{-27}
Vela	0.5	22	7.3×10^{-27}
1951+32	2.5	50	1.5×10^{-27}
1706-44	1.8	20	8.8×10^{-27}
1509-58	4.4	13	2.1×10^{-26}
0540-69	4.9	40	2.2×10^{-27}
1823-13	4.1	20	8.8×10^{-27}
1046-58	3.0	16	1.4×10^{-26}
1259-63	4.6	42	2.0×10^{-27}
1800-21	3.9	15	1.6×10^{-26}
	0.15	347	1.0×10^{-27}
1757-24	4.6	16	1.4×10^{-26}

Table 2. Typical pulsars and possible h limit with a 1 year observation of LCGT. These pulsars expect SNR ≥ 10 if its radiation is allowed to be maximum.

3.5. Stochastic Gravitational Wave background

The stochastic gravitational wave background can arise from some processes: inflation, cosmic string, first phase transition of Electro-Weak interaction. The gravitational wave background, Ω_{gw}, can characterize its spectrum as a fluctuation of the energy density ρ_{gw},

$$\Omega_{gw}(f) = \frac{1}{\rho_c} \frac{d\rho_{gw}(f)}{dlnf}, \quad (9)$$

where ρ_c is the critical density. Because of its stochastic nature of the amplitude and the phase of the background

waves, we need to use the cross correlation of data from two or more detectors.

Two independent interferometers of LCGT will give a detection limit of stochastic gravitational waves as $h_0^2\Omega_{gw}(100\text{Hz}) \sim 4.8 \times 10^{-10}$ for a one-year observation. This detection limit is better than the maximum possible limit from nucleosynthesis, string cosmology and a cosmic string[13]. If there are cross-talk noises between two interferometers of LCGT, they will contaminate the correlation spectrum (Table 3).

	$h_0^2\Omega_{gw}(100\text{Hz})$ (1yr)
single LCGT	$\sim 3.8 \times 10^{-5}$
two LCGT	$\sim 4.8 \times 10^{-10}$
(5% cross talk)	$(\sim 9.5 \times 10^{-8})$

Table 3. Possible upper limit for stochastic gravitational waves with a one-year observation

3.6. Advantages of Two Interferometers of LCGT in Data Analysis

Using two interferometers of LCGT, we can apply a consistency check between them in the case of a true gravitational wave signal. Using the coherent addition of signals from two interferometers, an SNR of gravitational wave will gain $\sqrt{2}$ times. This extends the detectable range of sources.

On the other hand, we can treat two detectors independently in the data analysis. After processing each signal, the coincidence of the list of candidates will be found for the case of a true gravitational signal, and will suppress the fake signals. Since non-stationary (non-gauss) noises are a crucial problem in the current event search analysis of ground-based detectors, coincidence is a very important technique to obtain a robustness of analysis. Two closely located interferometers can distinguish the time difference of gravitational waves within micro-second, in principle. The actual time resolution of event identification is typically $\leq$ 1msec for the case of an inspiral or ring-down gravitational wave. Assuming a 1 msec time window and fake suppression due to accidental coincidence $\leq 3\sigma(\sim 3\times10^{-3}$events/yr), a single detector allows a fake event rate of 3.0×10^{-4} [event/sec], which can be easily achieved in the current analysis of TAMA. This is because the LISM-TAMA coincidence study resulted in a 10^{-4} suppression of fake events in inspiral gravitational wave search[14].

If cross-talk noise exists between two interferometers, this will appear as coincidence signals. For the case of non-stationary noises (spike, glitch, etc.), the fake signal amplitude is proportional to the coupling between the detectors. By a careful treatment of the consistency in the amplitude and the waveform, or a tuning of the different electrical transfer functions of two detectors, we can reduce such cross-talk down to a negligible level. For the case of cross talk in stationary noises, i.e. seismic motions, the accidental coincidence in inspiral or ring-down search, it is not fatal. A simulation study predicts that the accidental coincidence will increase by 10 times with 30% cross-talk of the noise power, which is pessimistically large cross-talk. If the cross talk occurs only in the frequency band of the seismic noise, there would be less effective contamination for inspiral/ring-down searches (Figure 4).

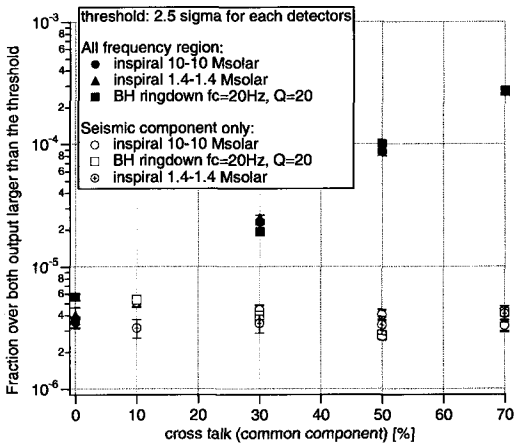

Fig. 4. Cross-talk noise and accidental coincidence for an inspiral/ring-down search

3.7. Work with International Detectors

We would like to comment about the world-wide network of gravitational wave detectors. The location of LCGT is important to complement any whole-sky coverage and for determining the source direction. Figure 5 displays the LCGT antenna pattern (response) on sky map. The azimuth direction (best sensitive direction) of the LCGT complements the insensitive direction of the interferometers located in the US or Europa.

Travel time between LCGT and the US/Europe sites makes possible a trigonometric survey of gravitational wave sources. The angular resolution is given as a function of the arrival-time resolution, ΔT, of each site[15]:

$$\delta\theta\ [\text{deg}] \simeq \sqrt{\Delta T\ \ [\text{msec}]} \times \begin{cases} 3.5 & \text{(whole sky average)} \\ 4.4 & \text{(galactic events).} \end{cases} \quad (10)$$

The existence of a world-wide network of gravitational wave is important not only to give confidence concerning detection, but also to ensure gravitational wave astronomy.

3.8. Our Experience and Resources for Executing the Search Tasks

We need human resources and computing costs to execute these search tasks. The computing requirements in some case are mentioned in above.

TAMA experiments provided good experiences and a legacy of our data analysis research in a run up to world-wide competition in this research field. For inspiral and burst searches, our activities have been displayed

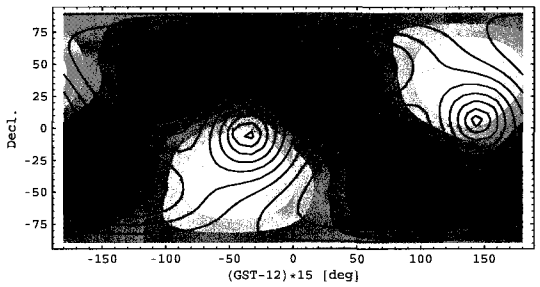

Fig. 5. LCGT antenna pattern on the whole-sky: The green contour line is same as LIGO Hanford detector. The x-axis is sidereal hours. The y-axis is the declination angle.

not only in TAMA data analysis, but also in the international cooperation. The ring-down search was well-implemented at TAMA for the first time in the world. We believe that these searches will be successfully execute in LCGT with sufficient computing power and employment of several post-doctoral staff members.

TAMA tried to search for a continuous signal from supernovae remnant pulsar, but did not survey all known candidates. Moreover, since TAMA consists of a single interferometer, a stochastic wave search was not executed. We should employ more experience for these searches.

Bibliography

[1] V.Kalogera et al., ApJ. **601**, L179-182 (2004) V.Kalogera et al., ApJ. **614**, L137-138 (2004)

[2] E.S.Phinney, ApJ. **380**, L17-21 (1991)

[3] internal report

[4] M.Shibata, Phys.Rev.Lett. **94**, 201101 (2005)

[5] internal report

[6] F.Echeverria, Phys.Rev.D **40**, 3194 (1989)

[7] E.E.Flanagan and S.A.Hughes, Phys.Rev.D **57**, 4535 (1998)

[8] J.D.E.Creighton, Phys.Rev.D **60**, 022001 (1999)

[9] H.Nakano et al., Phys.Rev.D **68**, 102003 (2003)

[10] T.Tsunesada et al., Phys.Rev.D **71**, 103005 (2005)

[11] H.Dimmelmeier et al., Astron.Astrophys. **393** 523-542 (2002)

[12] internal report

[13] M.Maggiore, gr-qc/0008027

[14] H.Takahashi et al., Phys. Rev. D **70** 042003 (2004)

[15] N.Kanda, Class. Quantum Grav., **20**, S761 (2003)

4. Infrastructure

[Author: OHASHI, Masatake]
ICRR, Univ. of Tokyo, Kashiwa, Chiba 277-8582

LCGT has three key characteristics: a 3 km baseline length, cryogenic mirrors and the underground site (in the Kamioka mine). The adoption of cryogenic sapphire mirrors to reduce the thermal noises is the most significant of these. Many feasibility studies have been carried out, and we have found no fatal problem. The complete cryogenic system was previously demonstrated by CLIK (Cryogenic Laser Interferometer in Kashiwa [1]).

Another feature of LCGT is the underground site in the Kamioka mine (one thousand meters below ground) to utilize a quiet and stable environment. Our 20 m Fabry-Perot type laser interferometer, LISM (Laser Interferometer Small observatory in kamioka Mine [2]), equipped with 25000 finesse cavities demonstrated that 120 hours of continuous operation was possible without any alignment control.

Based on this R&D, CLIO has been planned in order to demonstrate the feasibility of a cryogenic laser interferometer at a displacement sensitivity level of around $1 \times 10^{-19}\mathrm{m}/\sqrt{\mathrm{Hz}}$ by reducing the thermal noise of the sapphire mirrors.

This section describes the LCGT infrastructure.

4.1. advantage of underground site

The site of LISM, and CLIO, near the Super-Kamiokande neutrino detector, is shown in Figure 1. It is also the planned site of LCGT.

The bedrock of Kamioka mine is so hard that the elastic wave velocity reaches up to 5 km/s, and there are no serious dislocations that might produce unexpected phase delays or waveform distortions. This results in high common-mode rejection of the seismic noise up to 20 Hz in LISM. The variations of the temperature and humidity are within 0.1 degree and 1% per day, respectively, which contributes to the small drift of the mirror alignment and change in the cavity length.

The seismic noise in Kamioka mine is a hundredth part of that in a metropolitan area, as shown in Figure 2.

Under the favor of this quietness, we succeeded to improve the sensitivity of LISM at the low frequency region, as shown in Figure 3.

In the same tunnel of CLIO, L-shaped laser strainmeters with a 100 m baseline for geophysical study were accomplished in 2003. The aim is to detect faint geodynamic signals, such as the fluid core resonance of the earth. It consists of two Michelson interferometers and a Fabry-Perot cavity, whose mirrors are attached to the bedrock to trace the ground motion. These interferometers have confirmed to record high-quality data for geophysics during two years [3].

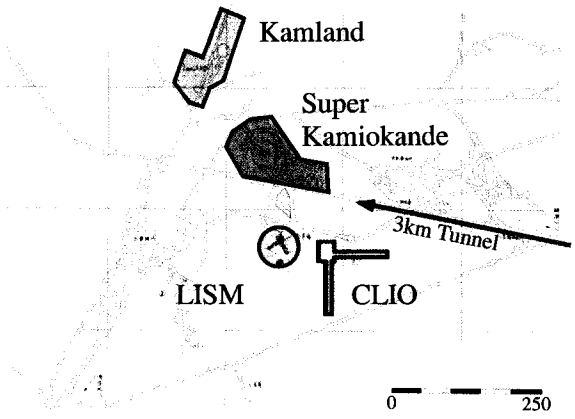

Fig. 1. CLIO and LISM site and nearby facilities in the Kamioka mine. Super-Kamiokande and KamLAND are world-famous neutrino detectors.

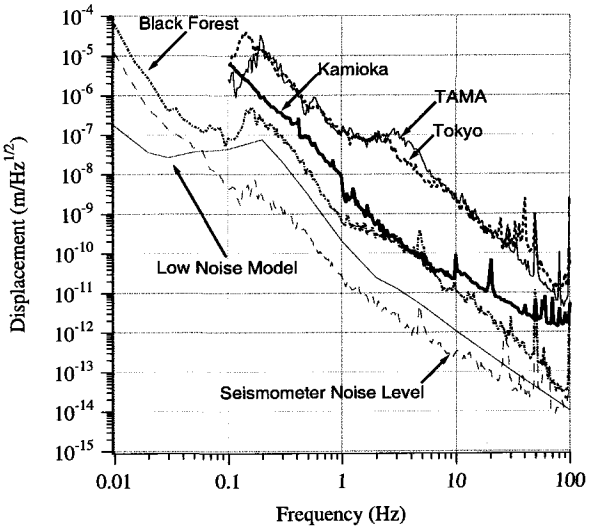

Fig. 2. Low seismic noise environment at the Kamioka site. Displacement noises at Kamioka, TAMA site, Tokyo, Black Forest and Low Noise Model (a hybrid spectrum of quiet sites in the world) are described.

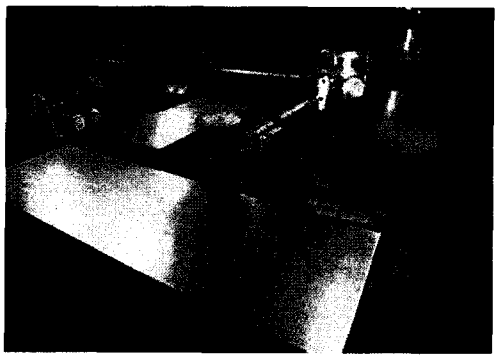

Fig. 3. 20 m interferometer in the Kamioka Mine (LISM)

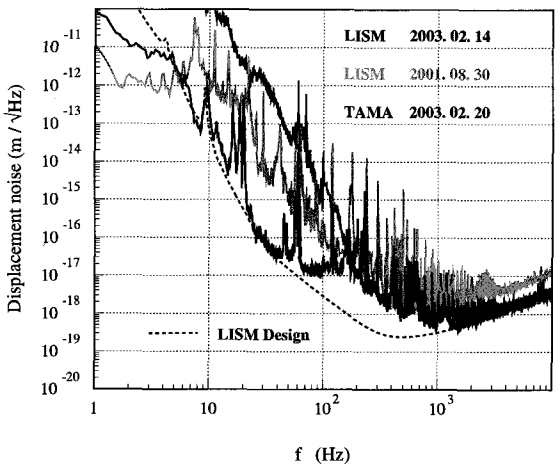

Fig. 4. Final displacement sensitivity of LISM compared with TAMA and former LISM

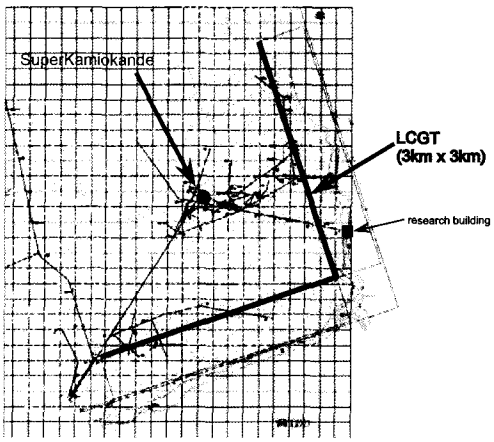

Fig. 5. Location of LCGT tunnel

Based on the above results, we believe the advantage of the underground site has been confirmed.

4.2. LCGT tunnel and research building

The location of the LCGT tunnel is shown in Fig. 5. The planned cross section is 4 m in height and 4.5 m in width, which is almost the same as that of the CLIO tunnel. The digging period is assumed to be about two and a half years. No difficulties to dig it are supposed, except for cases of serious water flow or flushing.

A research building will be constructed near to the tunnel entrance. It will have about twenty rooms for interferometer control, data analysis, monitor, assembling, experiments, etc.

Bibliography

[1] Miyoki S et al. 2003 *submitted to RSI*

[2] S. Sato, et al. Phys. Rev. D 69 (2004) 102005.

[3] S. Takemoto, et al. Jour. of Geodynamics 38 (2004) 477.

5. Vacuum system

[Author: SAITO, Yoshio]
KEK-High Energy Accelerator Research Organization, Tsukuba, Ibaraki 305-0801
In collaboration with TAKAHASHI, Ryutaro
National Astronomical Observatory of Japan, Mitaka, Tokyo 181-8588

5.1. Overview

The aimed sensitivity of LCGT is $1 \times 10^{-20}\mathrm{m}/\sqrt{\mathrm{Hz}}$ at 100 Hz. According to the result of a direct measurement of residual gas effects in TAMA300[1], the predicted noise due to the residual gas (water molecules) is $1 \times 10^{-21}\mathrm{m}/\sqrt{\mathrm{Hz}}$ at 2×10^{-7} Pa. Then, we can obtain a safety factor of 10.

The specifications of the vacuum system are as follows (*for one arm*):

Aimed pressure	2×10^{-7} Pa	
Beam tube		
Total Length	3 km	
Diameter	1 m	
Unit length	11 m	
Material	Pure Ti or SS304L	
Connection	Welding on site	
Pumping system		
Initial pumping	Root pump ($100\,\mathrm{m^3\ h^{-1}}$)	10 sets
Main pumping	Turbo pump ($1\,\mathrm{m^3\ s^{-1}}$)	30 sets
Vacuum keeping	Ion pump ($1\,\mathrm{m^3\ s^{-1}}$)	30 sets
Baffle		
Height	35-50 mm	
Surface	DLC coatings	
Number	90	

5.2. Beam tube

The stainless-steel material SS316 is among the most available for use as long tubes of 3 km long and 1.0 m in diameter. Since baking over the entire system of long tubes is not easy, further requiring a large electric power supply, some kinds of surface processing methods for reducing outgas are necessary to be applied to the unit tubes before installation in the tunnel; the length of the unit tube is 11 m, or less, according to Japanese traffic regulations. Several methods of surface treatment, such as electro-chemical buffing (ECB)[2], electrolytic polishing (EP)[3], chemical polishing (CP)[3] and TiN-coatings[4], are effective to remove/modify a surface deteriorated layer. The ECB method is practically advantageous for large-chamber applications, because it can be performed without any large liquid reservoir or large coating system. This method was successfully applied to the TAMA300 system; the vacuum pressure was kept on the order of 10^{-7} Pa without baking[5].

A further investigation concerning the water-molecule adsorption was carried out for an ECB-treated surface. The oxidized surface layer formed after ECB processing was found to be improved by in-vacuum heating at 250 °C, becoming more passive for water-molecule adsorption. In order to obtain a lower outgassing rate in the LCGT system than in TAMA300, every unit tube of stainless steel should be followed by a heat treatment after the ECB process.

A titanium material has generally been used as a getter pump because of its active surface without an oxidized layer. Since, once oxidized, the surface becomes chemically passive and stable, it is widely used as a corrosion-proof material. The humidity inside the mining tunnel to be offered to LCGT is high, and titanium seems to be a more suitable material than stainless-steel. The chemically stable surface is also expected to be effective to reduce the outgassing rate of water molecules, and, recently, the titanium material has been applied to vacuum chambers[6].

An additional process of heating is expected to, further, affect the chemical stability. Heating at 200 ^{0}C in a vacuum or in an inert gas is, in practice, found to be the most effective method for outgas reduction[7]. The thickness of the processed layer is 10 nm, which is not so different as in the natural layer, but the microstructure can be observed as being amorphous. This indicates that the processed layer is dense and becomes passive to water-molecule adsorption. A much thicker layer of 100 nm formed by heating at 450 ^{0}C, or more, shows a higher outgassing rate; the layer structure is in rutile and shows cracks.

Figure 1 shows the outgassing rates measured for stainless-steel and titanium ducts of 1 m long and 150 mm in diameter. The ECB-processed stainless-steel duct, followed by in-vacuum heating, shows a rate of 1×10^{-8} Pa $\mathrm{m^3\ s^{-1}\ m^{-2}}$ (50-h pumping), while the 10 nm oxidized titanium is 5×10^{-9} Pa $\mathrm{m^3\ s^{-1}\ m^{-2}}$. From the results of a residual-gas analysis, the partial pressure of the water in the titanium duct is lower than that in the stainless-steel one, showing a passivated titanium surface to water molecules. Since molecules of higher polarizability, such as water, should be pumped out for minimizing any laser-beam scattering disturbance[1], titanium seems to be more suitable material for the LCGT beam tubes; the residual pressure is desirably reduced to be 2×10^{-7} Pa, or less, for water molecules, while it is 1×10^{-5} Pa for hydrogen.

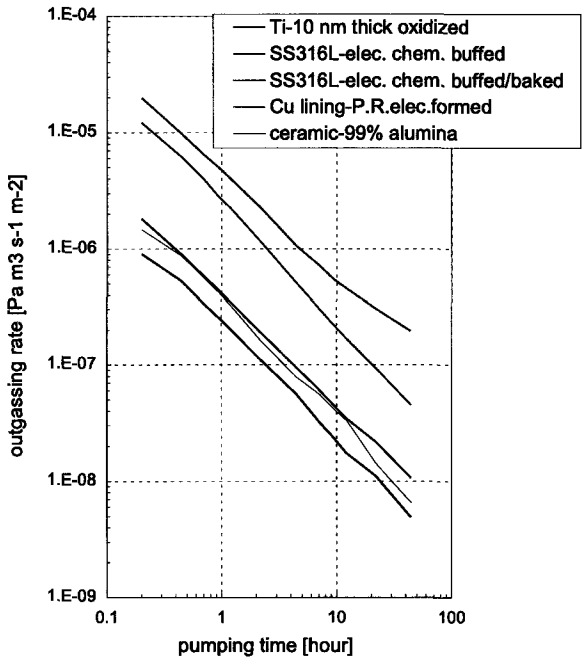

Fig. 1. Outgassing rates measured for several kinds of materials and surface processings. Test ducts are 1 m long and 150 mm in diameter.

5.3. Tube installation

The on-site welding of unit tubes for producing a km-long tube is considered to be a practical way, rather than using flange joints with gaskets, from the view point of cost. However, carefulness in controlling shield gas flow is necessary to avoid any unnecessary oxidization at/adjacent to the weld beads, whether the unit tube is made of titanium or stainless-steel. Leak testing is to be performed immediately after welding without any pumping inside the tubes; a test may be carried out by a sniffing technique.

Since four beams are to be operated inside a tube of 1000 mm in diameter, the straightness of the 3-km long beam tube is required to be within 10 mm. A GPS[8] can not be applied for tube alignment; all of the LCGT system will be installed under a mountain. A laser tracker, having an accuracy of 0.1-mm transverse deviation for every 20-m long base line, is possibly the most useful way. The accumulated deviation is to be within 15 mm in 3 km, which seems to meet the requirement.

5.4. Pumping system

From atmospheric pressure to several tens of Pa, a mechanical pump is first operated. A dry pump of the roots type equipped with multi-stages, recently being developed to reach a lower ultimate pressure of several Pa, is available. With an additional booster-roots pump, a pumping speed of 100 m^3 h^{-1} can be obtained. A pump-down period before switching on a turbo-molecular pump, is estimated to be a few days, when ten of the roots pumps are installed in each 3-km tube; the re-adsorbing effect of water molecules is taken into account concerning the pump-down time constant.

After the tube pressure is reduced to be on the order of 10^{-5} Pa by operating turbo-molecular pumps, an ion pump is considered to be most convenient for further pumping and keeping the vacuum.

Supposing the outgassing rate per unit area, q, to be uniform in the beam tube surface, the pressure distribution along the tube of L-m long can be expressed as[9]:

$$p(x) = -\frac{qAL}{2cN^2}\left(\frac{x}{L/N}\right)^2 + \frac{qAL}{2cN^2}\left(\frac{x}{L/N}\right) + p_{\min}, \quad (11)$$

$$p_{\min} = \frac{qA}{SN}, \quad (12)$$

$$\frac{p_{\max}}{p_{\min}} = \frac{SL}{8cN} + 1, \quad (13)$$

where a number of pumps, N, having a pumping speed of S [m^3 s^{-1}] for each, are installed at equal distance; c is the conductance per meter, and A is the surface area of the entire tube. In case of $q = 1 \times 10^{-8}$ Pa m^3 s^{-1} m^{-2}, which is a typical value for a stainless-steel surface after 50 hours of pumping (without bake), the pressures in the tube are estimated to be

$$p_{\min} = 3.8 \times 10^{-6}\text{Pa}, p_{\max}/p_{\min} = 1.06, \quad (14)$$

where $S = 1\,m^3$ s^{-1} and $N = 30$. The pressure can possibly be reduced by an order of magnitude, after a duration of 500 hours pumping; in a titanium tube it may be reduced further during the early stage of pumping.

5.5. Scattered light noise

The light scattered from the arm cavity mirrors will make multiple reflections from the inside wall of the polished tube back onto the mirrors causing phase noise on the interferometer output beam. By vibrating one of the tubes of TAMA300, we directly observed the effect of scattered light on the displacement sensitivity[10].

The geometry of the scattering path is shown schematically in Fig.2. The main beam, which is resonant on the axis of the cavity consisting of two mirrors, has a power of P_0. The light power scattered from the near mirror and reflected only once from the beam tube surface toward the far mirror is proportional to the scattering properties of the mirror surface, described by the bi-directional reflection distribution function, BRDF(ϕ), to the magnitude of the incident light power, to the reflectivity of the beam tube surface, and to the magnitude of the solid angle into which the light is scattered. The power ratio of the scattered light incident on the far mirror was calculated for a single reflection at the middle of the beam tube. In this expression, $R(\phi_i)$, is the reflectivity of the beam tube wall, and ϕ_i is the average scattering angle related to the incident angle, θ, by equation $\phi_i = \pi/2 - \theta$.

$$\frac{P}{P_0} = R(\phi_i)\int_{\phi_{min}}^{\phi_{max}} \text{BRDF}(\phi) 2\pi\phi \mathrm{d}\phi, \quad (15)$$

The BRDF of the TAMA mirrors is not known. We used the typical BRDF of mirrors in LIGO:

$$\mathrm{BRDF}(\phi) = \frac{1000}{(1+5.302\times10^8\phi^2)^{1.55}}. \quad (16)$$

The minimum and maximum scattering angles are determined by the radius of the beam tube, r_{tube}, the cavity length, L, the average scattering angle, and the length of the reflection region of the tube wall, ΔL, as follows:

$$\phi_{min} = \frac{2r_{tube} - 2\sin(\phi_i)\Delta L}{L}, \quad (17)$$

$$\phi_{max} = \frac{2r_{tube} + 2\sin(\phi_i)\Delta L}{L}. \quad (18)$$

The incidence angle at the far mirror, which is also the average scattering angle from the near mirror, is

$$\phi_i = \frac{2r_{tube}}{L}. \quad (19)$$

Next, the scattered light incident on the far mirror re-scatters within the diffraction angle of the main beam, and combines coherently, causing phase noise. The diffraction angle of the main beam, ϕ_{main}, is proportional to the wavelength, λ, and inversely proportional to the radius of the beam waist, $\omega_0 = \sqrt{L\lambda/2\pi}$,

$$\phi_{main} = \frac{\lambda}{\pi\omega_0}. \quad (20)$$

Finally, the fraction of light power scattered into the interferometer beam is

$$\frac{P_{scat}}{P_0} = \frac{P}{P_0}\int_{\phi_i-\phi_{main}}^{\phi_i+\phi_{main}} \mathrm{BRDF}(\phi)2\pi\phi\mathrm{d}\phi. \quad (21)$$

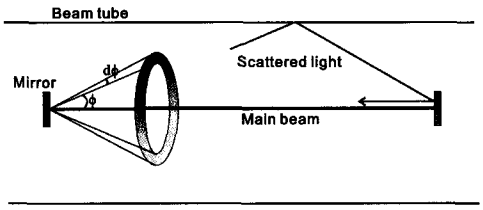

Fig. 2. Geometry of the scattered light path from the arm cavity mirrors. A part of lights reflected from the beam tube surface recombines within the main beam.

Since the path difference traveled by the scattered light is much greater than the wavelength of light, it is difficult to know the static phase difference, $\Delta\Phi_{scat}$, of the scattered electric field vector, E_{scat}, in Fig.3. However, the maximum phase fluctuation, $\delta\Phi_{comb}$, of the combined noisy electric field vector, E_{comb}, occurs when $\Delta\Phi_{scat}$ is equal to zero or π. Both mirrors scatter light into the interferometer beam. Then,

$$\delta\Phi_{comb} = 2\frac{E_{scat}}{E_{main}}\delta\Phi_{scat}. \quad (22)$$

The square of E_{scat}/E_{main} corresponds to the scattered power ratio, P_{scat}/P_0, exactly. The optical path length of the scattered light—as it traverses between the near mirror, the reflecting surface at the midpoint of the beam tube, and the far mirror—fluctuates by the peak amount $\delta\ell$ when the beam tube undergoes a peak radial displacement of δz,

$$\delta\ell = 4\frac{r_{tube}}{L}\delta z. \quad (23)$$

The average radial displacement for the half-period of the sinusoidal axial mode between the tube supports is approximately $1/\sqrt{2}$ smaller than the peak amplitude, so the mirror displacement noise is correspondingly smaller. The round-trip phase fluctuation, $\delta\Phi_{scat}$, is proportional to this optical path fluctuation. Therefore the maximum average mirror displacement noise, δx, caused by the scattered light is

$$\delta x = \sqrt{\frac{P_{scat}}{P_0}}\cdot\delta\ell. \quad (24)$$

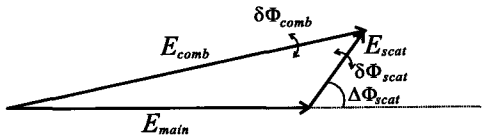

Fig. 3. Relation between the main beam, E_{main}, and the scattered light, E_{scat}. The static phase difference, $\Delta\Phi_{scat}$, is unreliable.

Actually, we must consider multiple reflections from the tube wall. Since two interferometers with suspention point interferometers use a common beam tube, mirrors are put with an offset of 0.34 m from the tube center and put at a distance of 0.6 m from each other. Using the parameters for LCGT ($\delta\tilde{z} = 1\times10^{-11}\mathrm{m}/\sqrt{\mathrm{Hz}}$, $r_{tube} = 0.5\,\mathrm{m}$, $L = 3{,}000\,\mathrm{m}$, and 0.125 m for the radius of the mirror) the calculated displacement noise for multiple reflections from the tube wall was found to be $\delta\tilde{x} = 4.2\times10^{-21}\,\mathrm{m}/\sqrt{\mathrm{Hz}}$. The tube vibration amplitude was assumed to be the same as the typical seismic motion in the Kamioka mine. LCGT requires a radiation pressure noise-limited strain of $\tilde{h} = 1\times10^{-23}/\sqrt{\mathrm{Hz}}$ at 30 Hz. This corresponds to a horizontal displacement noise of $\delta\tilde{x} = 3\times10^{-20}\,\mathrm{m}/\sqrt{\mathrm{Hz}}$. The calculation indicates that the displacement noise due to scattered light reflecting from the tube wall will have a safety factor of 7 smaller than the requirement.

5.6. Baffle

Figure 4 shows the integrated noise shaded by baffles from light with reflections less than the indicated number as well as the noise with the indicated reflection number, itself. To reduce the integrated scattered light noise by 1/10 ($2\times10^{-22}\mathrm{m}/\sqrt{\mathrm{Hz}}$ for one mirror), 45 baffles are necessary.

To avoid re-scattering from the surface of a baffle, the surface should be treated with a "black" coating without

increasing the outgassing rate. We found that Diamond-Like Carbon (DLC) coatings are suitable for this aim[11]. The outgassing rate was better than that at a surface of SUS316 with baking. The reflectivity of the DLC surface was 5% at the minimum for a laser beam of Nd:YAG ($\lambda = 1064\,\mathrm{nm}$).

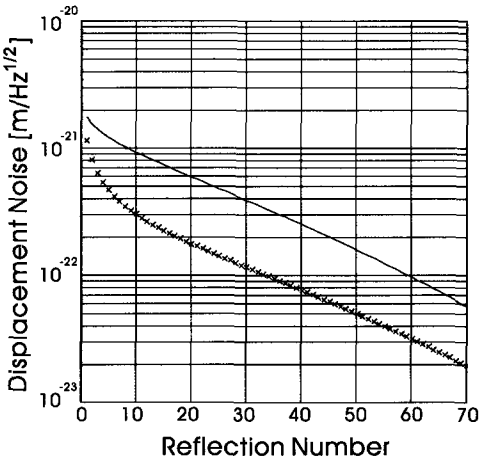

Fig. 4. Integrated noise shaded by baffles from the light with reflections less than indicated number (solid line) as well as the noise with indicated reflection number itself (×).

Bibliography

[1] R. Takahashi *et al.*, J. Vac. Sci. Technol. **A20**, 1237 (2002).

[2] Y. Saito *et al.*, Vacuum **53**, 353 (1999).

[3] S. Inayoshi *et al.*, J. Vac. Soc. Japan **41**, 96 (1998).

[4] Y. Saito *et al.*, Vacuum **47**, 609 (1996).

[5] Y. Saito *et al.*, Vacuum **60**, 3 (2001).

[6] M. Minato *et al.*, J. Vac. Soc. Japan **41**, 335 (1998).

[7] H. Morimoto *et al.*, J. Vac. Soc. Japan **45**, 665 (2002).

[8] W. E. Althouse *et al.*, Rev. Sci. Inst. **72**, 3086 (2001).

[9] Y. Saito *et al.*, Vacuum **44**, 535 (1993).

[10] R. Takahashi *et al.*, Phys. Rev. **D70**, 062003 (2004).

[11] R. Takahashi *et al.*, Vacuum **73**, 145 (2004).

6. Main interferometer

[Author: ANDO, Masaki]

Department of Physics, Univ. of Tokyo, Hongo, Tokyo 113-0033

6.1. Design concept

LCGT is comprised of two independent sets of interferometers. Each interferometer has an optical configuration of resonant-sideband extraction (RSE) with power recycling.

6.1.1. *Tandem interferometer design*

In order to reduce fake events and to declare the detection of gravitational-wave signals with high confidence, LCGT is comprised of two sets of interferometers. They are constructed with an identical conceptual design, and placed about 50 m away from each other with co-aligned arm directions. They are constructed to be as independent as possible: independent laser sources, input optics, seismic isolation and suspension systems, and photodetection optics. Though the 3 km vacuum ducts for the arm cavities are used commonly in two interferometers, the beam axes are sufficiently separated from each other to avoid cross correlations.

Since the distance between the interferometers is much smaller than the wavelength of target gravitational waves (3000 km for a 100 Hz signal), gravitational-wave signals appear in the output of two interferometers almost simultaneously with the same waveform. On the other hand, these interferometers are built to be as independent as possible so as to have different responses to various kind of noises. For example, the resonant frequencies of seismic isolation systems are slightly shifted in two interferometers so as to reduce the correlations of seismic disturbances. With this design, fake events by external disturbances are rejected effectively by checking the consistency of the output of two interferometers. In a rough estimation, the fake rate will be reduced by a factor of the coincidence window time, which can be the same order of the light-traveling time between two interferometers, in principle. Thus, we expect a fake reduction rate of about 10^{-6} (see 'Data analysis' section for detailed estimation).

6.1.2. Resonant-sideband extraction with power recycling

The interferometer has an optical configuration of resonant-sideband extraction (RSE) [1] and power recycling [2] (Fig. 1). In the RSE configuration, in which a signal-extraction mirror is placed at the output port of a Fabry-Perot Michelson interferometer, high laser power is stored in high-finesse arm cavities, while the optical component that contains gravitational wave signal information is effectively extracted to the dark port where the main photo-detector is placed. The effectiveness of RSE

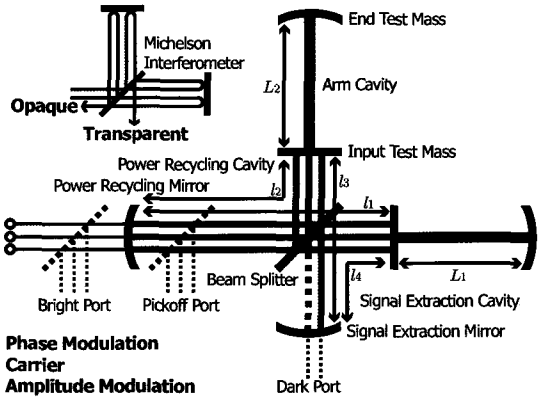

Fig. 1. Schematic of the optical configuration of the LCGT detector. The interferometer has an optical configuration of resonant-sideband extraction (RSE) and power recycling.

is described by a signal bandwidth gain, which is defined as the ratio of the signal bandwidth with and without a signal-extraction mirror. On the other hand, power recycling, in which a power-recycling mirror is placed between the input optics and the beam splitter of the main interferometer, is a technique used to increase the laser power in an interferometer. The effectiveness of power recycling is described by an optical power gain, which is defined as the ratio of the laser power in an interferometer with and without a power-recycling mirror.

Originally, the RSE scheme was adopted in LCGT because it is indispensable to meet two contrary requirements: a high laser power in the interferometer to reduce optical-readout noise, and small heat absorption in the front mirror substrates so as to keep the interferometer at a cryogenic temperature. The heat absorption is a critical problem because sapphire, which is used as the mirror substrate in LCGT, has much larger heat absorption than fused silica, which is mainly used in the current room-temperature interferometers. In the RSE configuration, optical power is stored in the high-finesse arm cavities, and the power-recycling gain is designed to be moderate. Thus, we can make the laser power that passes through the mirror substrate small, while keeping high laser power in the arm cavities. As a result, heat absorbed in the mirror substrates can be within the heat-pumping ability of the cryocoolers.

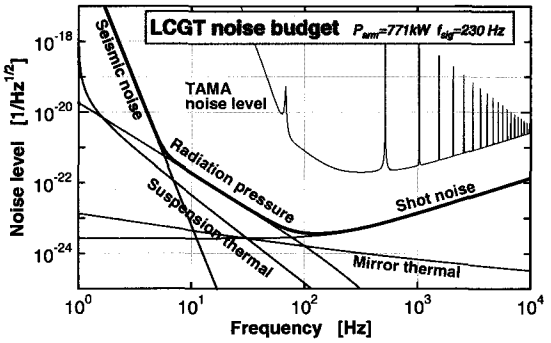

Fig. 2. Design sensitivity of LCGT. The floor level is $4 \times 10^{-24}/\sqrt{\text{Hz}}$ at around 100 Hz. The sensitivity is dominated by the optical readout noise (shot noise and radiation-pressure noise) at most of the observation frequency band. The observation band is limited by seismic noise at a low-frequency band below 10 Hz. Thermal noise does not limit the LCGT sensitivity, thanks to the cryogenic interferometer design.

Table 1. Main parameters of the LCGT interferometer.

Item	Parameter
Input laser power	75 W
Power in cavities ($P_{\rm arm}$)	780 kW
Signal bandwidth ($P_{\rm sig}$)	230 Hz
Cavity Finesse	1550
Power recycling gain	11
Signal bandwidth gain	15

6.2. Interferometer parameters

The optical parameters of a LCGT interferometer are given in Table 1. These parameters are determined to optimize the interferometer noise level.

6.2.1. Optical readout noise

Figure 2 shows the design sensitivity of each interferometer of LCGT. The strain sensitivity is $4 \times 10^{-24}/\sqrt{\text{Hz}}$ at around 100 Hz. The sensitivity curve is dominated by the optical readout noise at most of the frequency band. Thermal noise, which is one of fundamental noise sources in room-temperature detectors [3, 4, 5, 6], does not limit the LCGT sensitivity, thanks to the cryogenic interferometer design. The observation band is limited by the seismic noise at a low-frequency band below 10 Hz.

Optical readout noise contains two types of noises: shot noise and radiation-pressure noise. As shown in Fig. 2, the LCGT design sensitivity is dominated by the shot noise in the high-frequency region and by the radiation-pressure noise in the low-frequency region. These noise levels are determined by the laser power in arm cavities and the signal bandwidth. Shot noise is understood to be photon-counting noise at the photo detector, and the noise level is inverse-proportional to the square-root of the laser power. On the other hand, radiation-pressure noise is caused by fluctuation of the photon number reflected by the mirror. The radiation-pressure noise level is proportional to the square-root of the laser power.

6.2.2. Optimization of noise level

Since the main target of LCGT is gravitational waves from a $1.4\,M_\odot$-$1.4\,M_\odot$ neutron star binary inspiral, the noise curve is optimized for their detection.

Figure 3 shows a contour map of the observable distance in a units of Mpc as a function of laser power in arm cavities ($P_{\rm arm}$) and signal bandwidth ($f_{\rm sig}$). The observable distance is defined as the distance with which a $1.4\,M_\odot$-$1.4\,M_\odot$ neutron star binary inspiral event is detected with a signal-to-noise ration (SNR) of 10, for the optimal direction and polarization of the source. This contour shows that there is a ridge from the left-bottom region to the right-upper region. This ridge represents the optimal $f_{\rm sig}$ for a given $P_{\rm arm}$. The solid line in Fig. 3 is the relationship between $P_{\rm arm}$ and $f_{\rm sig}$ for a Fabry-Perot-Michelson interferometer (without RSE and power recycling) with various finesse of the arm cavities. With power recycling and RSE, $P_{\rm arm}$ is increased by the power-recycling gain, and $f_{\rm sig}$ is increased by the signal-bandwidth gain.

The optical parameters of LCGT are selected while considering this $P_{\rm arm}$-$f_{\rm sig}$ relationship and practical constrains (optical losses in the interferometer and controllability of the interferometer). We selected a finesse of arm cavities of 1550, power recycling gain of 11, and signal-band gain of 15. The reflectivity of the mirrors to realize these optical parameters is summarized in Table 2

Table 2. Designed reflectivity of mirrors.

Mirror	Reflectivity
Front mirror	99.6%
End mirror	99.995%
Power-recycling mirror	80.0%
Signal-extraction mirror	77.0%

6.3. Length sensing scheme

6.3.1. Optical path length to be controlled

The LCGT Detector Length Sensing and Control (LSC) subsystem is responsible for maintaining optical resonance in the interferometer, such that a linear signal, proportional to the metric strain, is available at the readout. To accomplish this, LSC must determine and control five independent length degrees of freedom. The optical configuration is shown in Fig. 1; for reference, the test masses, recycling mirrors, cavities and the interferometer output ports are also defined. The five longitudinal degrees of freedom are listed in Tab. 3.

6.3.2. Modulation scheme

The sensing system that is used to read-out the main interferometer length degrees of freedom is modified from

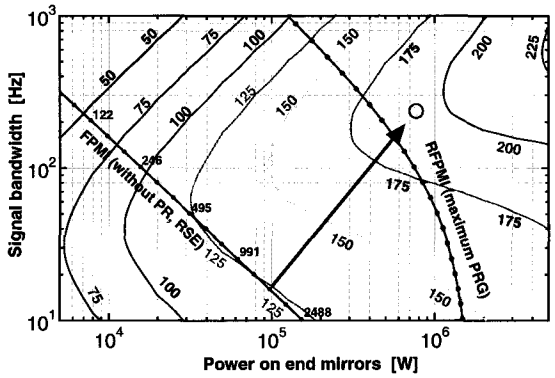

Fig. 3. Contour map of the observable distance in units of Mpc as a function of the laser power in arm cavities ($P_{\rm arm}$) and signal bandwidth ($f_{\rm sig}$). The black numbers along the curve of FPMI represent the finesse of the main cavity. The observable distance is defined as the distance at which a $1.4\,M_\odot$-$1.4\,M_\odot$ neutron star binary inspiral event is detected with a signal-to-noise ration (SNR) of 10, for an optimal direction and polarization of the source.

Table 3. The definition of length degrees of freedom

Name	Symbol	Definition
Common arm length	L_+	$L_1 + L_2$
Differential arm length	L_-	$L_1 - L_2$
PRC length	$l_{\rm P}$	$l_1 + l_2$
Michelson length	l_-	$l_1 - l_2$
SEC length	$l_{\rm S}$	$l_3 + l_4$

that used in power-recycled Fabry-Perot-Michelson interferometer [3, 4, 6] to allow efficient operation with RSE. The light from the laser source is modulated at 2 frequencies and light from the interferometer is analyzed at 3 points: the main output from the detector (Dark port), the light reflected from the power recycling mirror (Bright port) and a small fraction of the light picked off inside the power recycling cavity (Pickoff port). The highlights of the sensing scheme are:

- Double modulation; Phase modulation (PM) and Amplitude modulation (AM)
- Michelson interferometer is completely transparent to PM; PM is resonant in PRC+SEC
- Michelson interferometer is completely opaque to AM; PM is resonant only in PRC

6.3.3. Sensor signals

The error signals for differential and common degrees of freedom of arm cavities (L_+, L_-) are extracted from the beat between the carrier and the PM. On the other hand, the signals of the central part of the interferometer ($l_{\rm P}$, l_-, $l_{\rm S}$) are obtained from the beat between the PM and the AM with double-demodulation technique. The baseline plant a matrix is shown in Tab. 4. L_+, L_-, and l_-signals are extracted in diagonal way, while $l_{\rm P}$ and $l_{\rm S}$ are almost orthogonal.

Table 4. Sensor signal matrix

	δL_+	δL_-	$\delta l_{\rm P}$	δl_-	$\delta l_{\rm S}$
$V_{\rm B}$	1	0	−.0037	0	.0027
$V_{\rm D}$	0	1	0	.0010	0
$V_{\rm P}$	.0017	0	1	0	.73
$V_{\rm D}$	0	.0010	0	1	0
$V_{\rm D}$	−.00032	0	−1.3	0	1

6.4. Control and operation system

6.4.1. Control loop design

In order to keep the interferometer at the operational point, the extracted length-deviation signals are fed back to corresponding optical components. The L_- signal is fed back to the arm-cavity mirrors differentially. The L_- control loop should have high gain at low frequency to suppress residual mirror motion. In order to avoid the effect of the laser intensity noise, the residual motion should be less than 1×10^{-14} m. On the other hand, the control gain should be smaller than 10^{-8} at the resonant frequencies of the mirror substrate at around 10 kHz so as not to excite the mirror resonance. Thus, the unity gain frequency is designed to be 500 Hz, and the low-frequency control gain is designed to be 10^8.

The L_+ signal is fed back to the arm-cavity mirrors commonly at a low frequency, and also fed back to the input optics and the laser source for frequency stabilization in a high frequency. The l_- signal is fed back to the beam splitter to keep the fringe of the Michelson interferometer. The unity gain frequency of l_- is set to be lower than the observation band of the interferometer, to avoid control noise from being introduced as the beam splitter motion. The l_P and l_S signals are fed back to the power-recycling mirror and the signal-extraction mirror, respectively. Since the gravitational-wave signal is hardly contaminated by these control noises, we can select high unity gain frequencies for these degrees of freedom, around 500 Hz.

6.4.2. Mirror actuator

The position of a main mirror is mainly actuated with multi-stage actuators: a coil-magnet actuator for the main mirror, that for the upper mass forming the suspension-point interferometer, and actuators of the seismic isolation system at the room-temperature. The coil-magnet actuator for the main mirror is formed with small magnets attached to the mirror and coils supported by a recoil mass. Since the noise of this actuator appears directly as the noise of the interferometer, the noise level should be very low, less than $3 \times 10^{-20}\,\mathrm{m}/\sqrt{\mathrm{Hz}}$ at 10 Hz. A requirement for the dynamic range of this actuator is 1 μm so as to keep the interferometer at the operational point. Since the noise of the actuator for the suspension-point interferometer is suppressed by controlling the suspension-point interferometer, the requirement for the noise level is relaxed, to less than $6\times10^{-16}\,\mathrm{m}/\sqrt{\mathrm{Hz}}$ at 10 Hz. This actuator has a dynamic range of 100 μm. The actuators at the room-temperature seismic isolation system are used for local control of the suspension system and interferometer length correction low frequency, less than 0.1 Hz.

6.4.3. Control system implementation

The signal sensing and control schemes of an interferometer have been developed with prototype interferometers and current interferometric detectors. In TAMA300 [6], the interferometer is stably operated with a Fabry-Perot-Michelson configuration with power recycling. On the other hand, signal sensing and control schemes for a RSE interferometer have been developed in prototype interferometers, a 4 m interferometer at NAOJ [7, 8] and a 4 m interferometer at Caltech [9]. These interferometers have been operated with the RSE configuration.

The LCGT interferometer has over 100 degrees of freedom to be controlled, including the input optics and the output optics. These control loops are implemented as a hybrid system of analog and digital circuits: analog circuits for high-speed controls, and digital circuits for low-frequency controls. These control loops are supervised by a set of master control computers, which organize the switching, gain changing, and monitoring of the control circuits.

6.4.4. Observation system

In a long-term (over a few month) continuous observation for gravitational waves, the detector operation is often disturbed by environmental drifts (changes in temperature, atmosphere pressure, and ground tilt, etc.) and sudden excitations (earthquakes and blasts in the Kamioka mine). The observation system monitors the detector condition and keeps a high duty cycle and the best sensitivity of the detector. The system is comprised of an automatic lock-acquisition system, an automatic interferometer-adjustment system, a monitor and diagnosis system, and operators (Fig. 4).

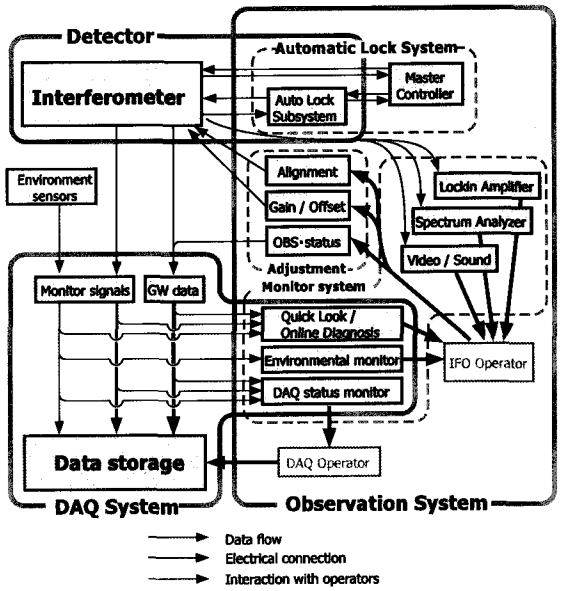

Fig. 4. Conceptual diagram of an observation system of LCGT. The observation system monitors the detector condition and keeps a high duty cycle and the best sensitivity of the detector.

During observations, the interferometer occasionally goes out of the operational condition because of external disturbances. The automatic lock-acquisition system recovers the operational condition and adjusts the interferometer automatically in such a case. The automatic adjustment sequence is also exercised when there are large drifts in the control loops, and when the detector sensitivity is degraded. Automatic lock acquisition and adjustment are realized by a master control computer, which monitors and organizes the control system.

The monitor and diagnosis system provide the operators tools to check the detector condition: real-time monitors of the detector status (laser power in the interferometer, feedback signals of the control loops, status of the data-acquisition system, the cryogenic system, and the vacuum system, etc.), information that is helpful for detector improvement (monitor for non-stationary noises, etc.) and fundamental information for data analysis (environmental disturbances, etc.).

Such an automatic observation system has been realized during the observation run of TAMA300. In the

ninth observation run of TAMA, the detector was operated for over two weeks with only a little help from the operators [10].

Bibliography

[1] J. Mizuno *et al.*, Phys. Lett. A **175** 273 (1993).

[2] R. W. P. Drever, Fabry-Perot cavity gravity-wave detectors, *The detection of gravitational waves*, ed. D. G. Blair, Cambridge University Press (1991) p. 306–328.

[3] A. Abramovici *et al.*, Science **256** 325 (1992).

[4] The VIRGO collaboration, *VIRGO Final Design Report* VIR-TRE-1000-13 (1997), C. Bradaschia, *et al.*, Nucl. Instrum. Meth. A **289** 518 (1990).

[5] K. Danzmann *et al.*, *Proposal for a 600m Laser-Interferometric Gravitational Wave Antenna* (Max-Planck-Institut für Quantenoptik Report) 190 (1994).

[6] M. Ando *et al.*, Phys. Rev. Lett. **86** 3950 (2001).

[7] O. Miyakawa, *'Development of Variable-Bandwidth Laser Interferometer for Gravitational Wave Detection'*, Ph. D thesis, Institute for Cosmic Ray Research, the University of Tokyo (2002).

[8] K. Somiya, *'Investigation of radiation pressure effect in a frequency-detuned interferometer and development of the readout scheme for a gravitational-wave detector'*, Ph. D thesis, Department of Advanced Materials Science, the University of Tokyo (2004).

[9] O. Miyakawa, S. Kawamura, B. Abbott, R. Bork, P. Fritschel, L. Goggin, J. Heefner, A. Ivanov, F. Kawazoe, C. Mow-Lowry, A. Ourjoumtsev, S. Sakata, M. Smith, K. Strain, R. Taylor, D. Ugolini, S. Vass, R. Ward, and A. Weinstein, *'Sensing and Control of the Advanced LIGO Optical Configuration'*, Optical Fabrication, Metrology, and Material Advancements for Telescopes, Edited by Atad-Ettedgui, Eli; Dierickx, Philippe, Proceedings of the SPIE, Volume 5500, pp. 92-104 (2004).

[10] M. Ando and the TAMA collaboration, *'Current status of the TAMA300 gravitational-wave detector'*, Proceedings of the 9th Gravitational Wave Data Analysis Workshop (December 15-18, 2004, Annecy, France), to be published in Class. Quant. Grav. (2005).

7. Laser Source

[Author: MIO, Norikatsu]

Department of Advanced Materials Science, Univ. of Tokyo, Kashiwa, Chiba 277-8561

The requirements for the laser system for LCGT are listed as:

- Wavelength : 1064 nm,
- Output power: 150 W (single frequency),
- Optical mode: TEM_{00},
- Polarization: Linear,

with extremely small fluctuations in its frequency and amplitude; the noise levels must be :

- Frequency noise $\delta\nu/\nu < 10^{-22}/\sqrt{\mathrm{Hz}}$,
- Intensity noise $\delta I/I < 10^{-8}/\sqrt{\mathrm{Hz}}$.

These parameters are determined in order to realize the projected sensitivity of LCGT. Among them, the power of the laser is the most important because it limits the fundamental noise level of LCGT, which can be achieved by using an effective light power (incident power times the power recycling gain) of 800 W at 1 μm. The LCGT system is designed to realize the optimum sensitivity, limited by the quantum noise of light. Since the RSE configuration needs high finesse in the arm cavities (approximately 1000), the projected power recycling gain is not very high; we assume that the gain is 10.6. Thus, the power of the laser light must be 75 W at the input of the interferometer. Since the transmittance of the input optics, including cascaded mode-cleaner cavities, is estimated to be 0.5, the power of the laser is larger than 150 W.

As shown in Fig. 1, there are several schemes for high-power solid-state lasers. We chose a side-pumped rod laser system because of its simplicity. Since the thermal lens effect and the thermal birefringence in the laser medium induced by pumping become significant problems for high-power lasers, we must compensate them. The simplicity of the rod system is the merit for obtaining the desired power because the compensation method is also simple. As for the thermal birefringence, there is the solution to use two identical laser rods and a polarization rotator (Fig. 2). Since the thermal lens caused in the rods is almost axial symmetric, it is easy to compensate the thermal lens effect by the cavity design.

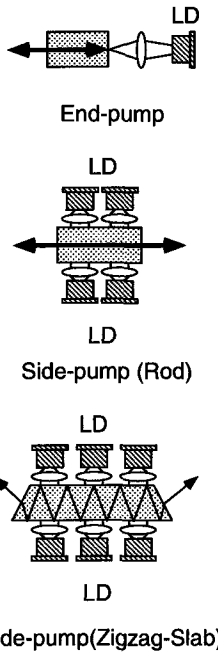

Fig. 1. Pumping method for high-power solid state lasers.

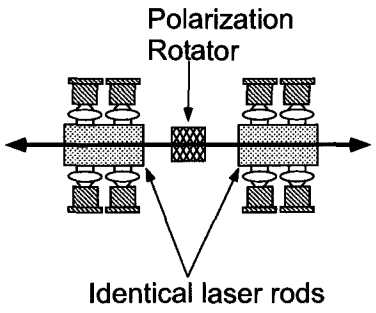

Fig. 2. Thermal birefringence compensation by two laser rods and a polarization rotator.

7.1. Design concept

The above requirements can be fulfilled by a laser-diode(LD)-pumped Nd:YAG laser. In order to obtain single-frequency oscillation, an injection-locking system[1, 2] and a master-oscillator-and-power-amplifier

(MOPA) system[3] are being developed, and are used for first-generation gravitational wave detectors. Although the injection-locking technique has been well established for 10-W output lasers, the control of a higher power laser is rather difficult because the intrinsic fluctuations become larger for obtaining higher power. As for injection locking, the power ratio between the master laser (P_{master}) and the slave laser (P_{slave}) becomes small; this ratio determines the frequency range where the injection locking is maintained (ν_{lock}), expressed as

$$\nu_{\mathrm{lock}} = \Delta\nu \sqrt{\frac{P_{\mathrm{master}}}{P_{\mathrm{slave}}}}, \tag{25}$$

where $\Delta\nu$ is the width of the slave-laser cavity[4]. Also, the power amplifier operated in the linear regime has an excess-noise problem, even at a higher frequency band. If the amplifier can be operated as a saturated amplifier, this problem can be eliminated. These problems must be considered for the LCGT laser system.

The system design for LCGT is shown in Fig. 3; this is based on the combination of the injection locking and MOPA. The first stage of the system is an injection-locked laser of 100 W output power; this comprises a master laser (2-W NPRO) and an 100-W slave laser. The second stage of the system is a power amplifier that can increase the power from 100 W to 150 W. Since it is possible to operate the amplifier with saturated amplification at this power level, the noise-amplification problem that arises due to unsaturated amplification can be reduced, as mentioned above.

Since the maximum power that has been achieved by the injection-locking system so far is 195 W[5], it is possible to realize a laser of 150-W output power based only on injection locking. However, we chose this combined system because of the following two reasons. Firstly, we can control the frequency and intensity of the output light by using independent subsystems. The frequency can be controlled by tuning the frequency of the injection-locked laser, and the intensity can be controlled by changing the gain of the amplifier. By using the two independent systems, the cross-coupling between two quantities can be reduced. Also, since the control width for the intensity is not affected by the laser cavity width, it is possible to obtain a wider control width if the amplifier is used as a control device for the laser intensity. Secondly, we can obtain more output power by adding additional power amplifiers; the output power of the power amplifiers has reached 200 W, and can possibly be extended to 300 W.

The development of high power lasers requires a large amount of money because pumping LDs and other optical parts are expensive. Also, the development needs quite a long time and much know-how concerning pumping, cooling and so on. In order to save cost and time, it is best for us to use a laser module that has been developed for precision laser manufacturing. Moreover, we can maintain the performance of the laser system by renewing the module, just like a commercial laser system for a manufacture. This is quite advantageous for the

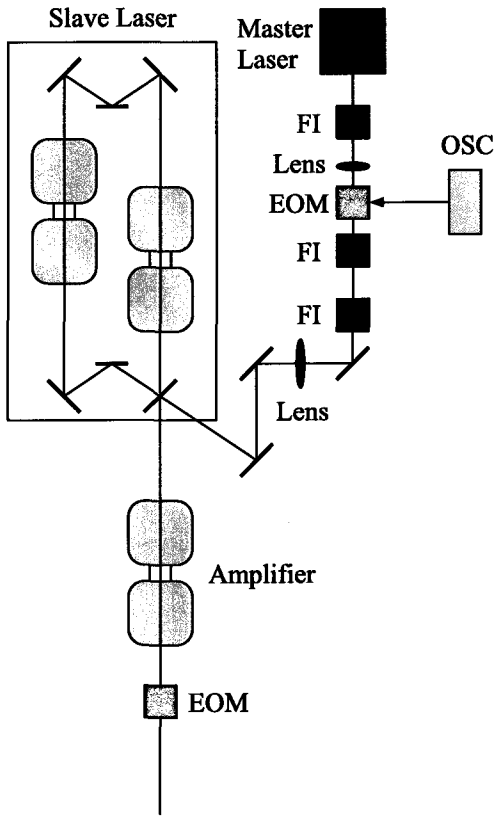

Fig. 3. Schematic view of one of the plans for the LCGT laser system. All of lasers and amplifiers are assembled using LD-pumped Nd:YAG crystals. As a master laser, a non-planer ring oscillator of 2 W is used. The slave laser, which has two laser modules, is used to obtain the power of 100 W; this can be achieved by means of high-power LD pumping systems. We will use a saturated power amplifier system for 150-W output.

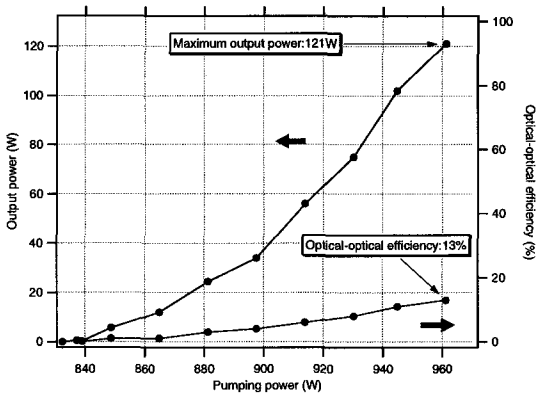

Fig. 4. Output power of the prototype laser in free-running.

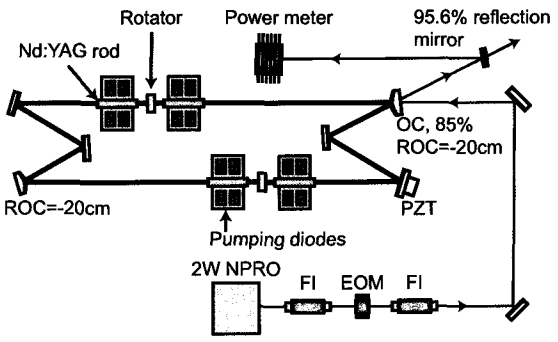

Fig. 5. Optical system of the injection locking experiment.

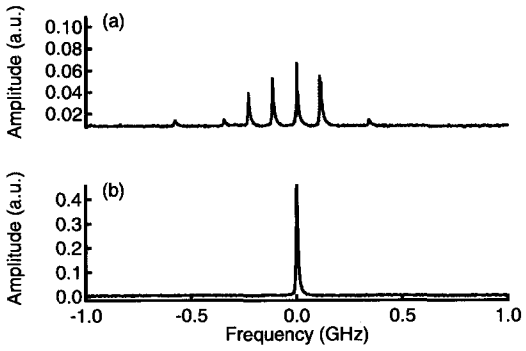

Fig. 6. Oscillation (longitudinal) mode of the slave laser measured by a scanning Fabry-Perot cavity. While the laser is in free-running state, several longitudinal modes oscillate (upper trace). Once the injection locking is realized, the single mode oscillation can be observed (lower trace).

light source of interferometric gravitational wave detectors because the system must be operated for 24 hours a day, 365 days a year.

7.2. Prototype system

In order to show the feasibility of the laser system, a prototype system has been designed and is being tested in collaboration with the Mitsubishi group, which has been developing high-power lasers with excellent beam quality for laser processing[6] .

The prototype laser system uses laser modules made by Mitsubishi. One laser module contains two laser rods and a quarts rotator, and each laser rod is pumped by several LDs. The rod is surrounded by a diffusive reflector in order to obtain a uniform pumping intensity; this is quite important to obtain good thermal birefringence compensation. Both the laser rods and the pumping LDs are cooled with chilled water; the modules are tuned to be operated at 25 °C.

We have developed a ring laser as a slave laser; we used two identical laser modules that are mentioned above in the laser cavity. In the free-running state, the laser that oscillated in both rotational directions had an output power of 121 W with a single transverse mode, as shown in Fig. 4.

For an injection-locking experiment, we used a maser laser (2-W NPRO) and related optics, such as Faraday ioslators, an electro-optic modulator (EOM), and a mode-matching lens as shown in Fig. 5. The Pound-Drever method was adopted for controlling the laser frequency; the error signal was fed back to a piezo-electric transducer (PZT) used for mounting one of the mirrors of the slave laser cavity in order to keep the frequency difference between the master and slave lasers within the locking range. Since the mechanical resonant frequency of the PZT limited the bandwidth, the unity gain frequency (UGF) of the control loop was 7 kHz.

When the injection locking was applied, we confirmed that the laser oscillated in a single frequency at the single direction determined by the injected light; the maximum power of the prototype was about 100 W, obtained by single-stage injection locking[7]. Figure 6 shows the oscillation mode measured by a scanning Fabry-Perot cavity; plural modes during free-running disappeared, and a single mode was observed when the injection lock was achieved. As for long-term operation, the laser could maintain the injection-locking for over 6 hours at a power level of 100 W, (Fig. 7). The beam quality expressed by M^2 parameter, was almost diffraction limited ($M^2 < 1.2$). The degree of the polarization was better than 40 : 1; this value was dependent on the alignment of the laser cavity.

The intensity noise of the laser is shown in Fig. 8. We found that the noise level was almost the same as that of a linear-cavity laser assembled with the same laser module. Also, it is much higher than that of the master. The free-running laser frequency noise was evaluated from the signal applied to the PZT for maintaining the injection lock; this corresponds to the fluctuation of the cavity length. Figure 9 shows the spectra that were measured when there was no lasing (below threshold) and lasing (above threshold). Since two spectra coincided well, we found that the fluctuation level was independent of the existence of the lasing, and thus could be improved by reducing the external noises such as acoustic noise and vibration noise.

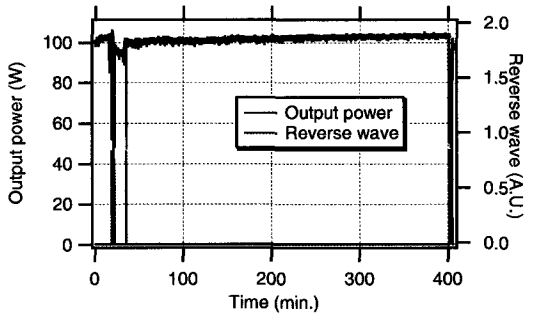

Fig. 7. Output power of the injection locked laser. The power of 100W can be kept for more than 6 hours.

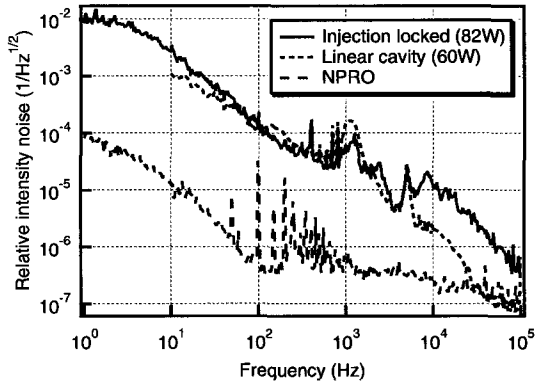

Fig. 8. Relative intensity noise of the injection locked laser.

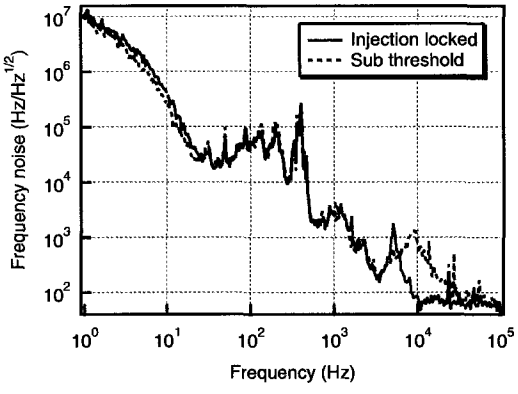

Fig. 9. Fluctuation of the cavity evaluated from the feedback signal to the PZT of the injection locked laser.

7.3. **Further development**

We are now developing a frequency-stabilization system for the protype. In order to achieve frequency stability, the attainable control band width should be as wide as possible. Although the salve cavity has a PZT for length control, the band width, which is limited by its mechanical resonance, is not very wide. Thus, we must look for an actuator for the frequency control. Since an EOM made of $LiNbO_3$ (LN) is widely used for this purpose, we are investigating the possibility to use it for our prototype. However, it is well known that the power level at which the LN can be used is not very high because of its photo-refractive damage. Thus, we are trying to use a stoichiometric LN (SLN), which is considered to have a much higher damage threshold than an ordinary LN crystal. If the EOM can be used inside the laser cavity, we can obtain a quite high UGF in the frequency-stabilization system.

As for the power amplifier, there is an experimental demonstration also by the Mitsubishi group[8]. We are now testing an amplifier system that is made of a small laser module for intensity stabilization; the injection-current control system is being developed. By the end of this year, another laser module that will have 50-W amplification capability will be available in our laboratory. The amplification performance and the beam quality as well as the noise levels will be evaluated.

In summary, we are now confident to build a laser system that can satisfy the requirements of LCGT.

Bibliography

[1] S. T. Yang et al., Opt. Lett. **21** (1996), 1676.

[2] I. Zawischa et al., Class. Quantum Grav. **19** (2002), 1775.

[3] F. Raab, Class. Quantum Grav. **18** (2001), 4107.

[4] A. E. Siegman, *Lasers* (University Science Books, California, 1986) Chapter 29.

[5] M. Frede, R. Wilhelm, D. Kracht, C. Fallnich, F. Seifert, B. Willke, CLEO2005, CMA1.

[6] S. Fujikawa, T. Kojima, and K. Yasui, IEEE J. Sel. Top. Quantum Electron. **3** (1997) 40.

[7] K. Takeno, T. Ozeki, S. Moriwaki and N. Mio, Opt. Lett. **30** (2005) (in press).

[8] S. Konno, S. Fujikawa and K. Yasui, Appl. Phys. Lett. **79** (2001), 2696.

8. Mode Cleaner

[Author: TELADA, Souichi]

AIST, 1-1-1, Umezono, Tsukuba, Ibaraki 305-8563

8.1. Optical Configuration

The purposes of the input mode cleaner are to clean the wave-front of the laser beam, to reduce the beam jitter, pre-stabilization of the laser frequency, and so on[1][2]. In LCGT, there are two input Mode Cleaners (MC) for each interferometer. One is the 1st MC, which is for reducing RF noises around the modulation frequencies for the main interferometer. The other one is the 2nd MC, which transmits the modulations for the main interferometer. These are shown in Fig 1.

8.1.1. 1st Mode Cleaner

The 1st MC is a triangle-shaped optical resonator, whose round trip is about 20 m and whose finesse is about 1700. The cavity pole frequency becomes 4.5 kHz. There are two modulations for the main interferometer, whose frequencies are 15.025 MHz and 49.5825 MHz. Since the FSR for 20 m round trip is 15 MHz, the round trip sets a slightly longer or shorter distance to avoid according the FSR with 15.025 MHz. Since this 1st MC should reduce the RF noise around the modulation frequencies for the main interferometer, a large separation is needed for the frequency difference between the modulation frequencies and the FSR of the 1st MC.

8.1.2. 2nd Mode Cleaner

The 2nd MC is also a triangle-shaped optical resonator. This 2nd MC transmits light of two kinds of modulation side-band together with light of carrier. One is 15.025 MHz phase modulation, and the other is 49.5825 MHz amplitude modulation. In order to transmit both frequencies, the round trip needs to be integral multiple of 60 m. We chose a 360 m round trip. The finesse is about 1000. The cavity pole becomes 416 Hz.

8.2. Specifications

Both MCs have a narrow triangle shape. Two mirrors, which are named input-mirror and output-mirror, are located inside one vacuum tank, another mirror, which is named the end-mirror, is located inside another vacuum tank. The incident angles of the laser beam to the input-mirror and the output-mirror are nearly 45 degree, and these mirrors have a planer curvature. The incident angle of the laser beam to the end-mirror is almost at a right angle, and the mirror is spherical. The optical specifications of both MCs are listed in Table 1.

8.3. Servo Control

A servo control system to keep operating the MCs is shown in Fig 2. At first, the laser frequency is stabilized by the 1st MC. The error signal from the 2nd MC is fed back to the 1st MC with electric servo filters. The lower frequency component from the 2nd MC is fed back to the end-mirror displacement of the 1st MC, and the higher frequency component from that is fed back to the error signal point of the 1st MC through a summation-amplifier. Similarly, a frequency-control signal from the main interferometer, which is called as δL_+ signal, is fed back to the end-mirror displacement of the 2nd MC and the error signal point of the 2nd MC.

8.4. Modulations

Phase modulation for the 1st MC is generated by an EOM located in front of the 1st MC. The method is as follows: The phase modulator for the 2nd MC and the modulators for the main interferometer are placed between the 1st MC and the 2nd one. A distortion of the wave-front caused by the modulators can be reduced by the mode cleaning-effect of the 2nd MC. Since the modulations for the main interferometer should be transmitted through the 2nd MC, the modulation frequencies need to be equal to multiple orders of the FSR of the 2nd MC. The modulations for the main interferometer are phase modulation and amplitude modulation. These are generated at a modulation unit, which consists of a Mach-Zehnder interferometer with a phase modulator (PM) and an amplitude modulator (AM) [3], is shown in Fig 1.

The phase-modulation frequency can be equal to the integral multiple of the FSR of the 2nd MC[4]. A frequency-modulation, whose frequency is a few kHz, is added to the laser source. The frequency modulation of the laser frequency is converted into amplitude-modulation in the transmitted phase-modulation side-band, if there is a difference between the phase-modulation frequency and the FSR of the cavity. The frequency of the phase modulation, which is generated by a synthesizer, is controlled so that the converted amplitude modulation will vanish. In this way, the phase-modulation frequency, which is close to 15.025 MHz, can be exactly equalized to an integral-multiple of the FSR.

On the other hand, in order to also transmit an amplitude-modulation side-band for the main interferometer, its frequency is generated by a synthesizer, which is locked as the reference of the synthesizer for the phase-modulation side-band, because the ratio of the amplitude-modulation frequency to the phase-modulation one is a ratio of thirty three to ten.

Bibliography

[1] A. Araya, N. Mio, K. Tsubono, K. Suehiro, S. Telada, M. Ohashi, and M-K. Fujimoto, Appl.

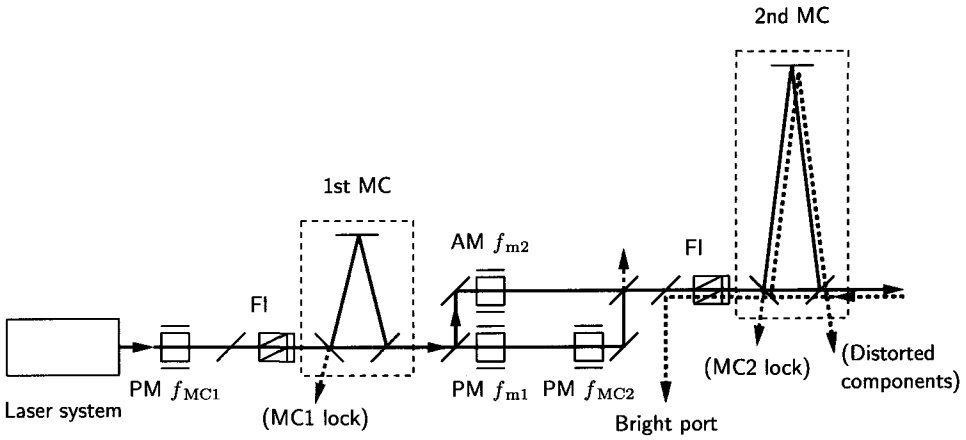

Fig. 1. Optical configuration of the input mode cleaners.

item	1st MC	2nd MC
curvature		
spherical mirror	15 m	300 m
reflectance		
plane mirror (S-pol.)	0.9982	0.9969
spherical mirror	> 0.9999	> 0.9999
finesse	1720	1000
mirror space		
plane to plane	0.2 m	0.5 m
plane to spherical	9.555 m	199.28 m
incident angle to spherical mirror	10.5 mrad	1.25 mrad
FSR	15.525 MHz	751.25 kHz
FSR	15.525 MHz	751.25 kHz
Beam half radios		
waist (horizontal)	1559.75 μm	6924.80 μm
waist (vertical)	1559.87 μm	6924.81 μm
on spherical mirror (horizontal)	2613.05 μm	11966 μm
on spherical mirror (vertical)	2612.99 μm	11966 μm
Higher-mode interval (horizontal)	4.60162 MHz	288.047 kHz
Higher-mode interval (vertical)	4.60126 MHz	288.047 kHz

Table 1. Specification of Two MCs.

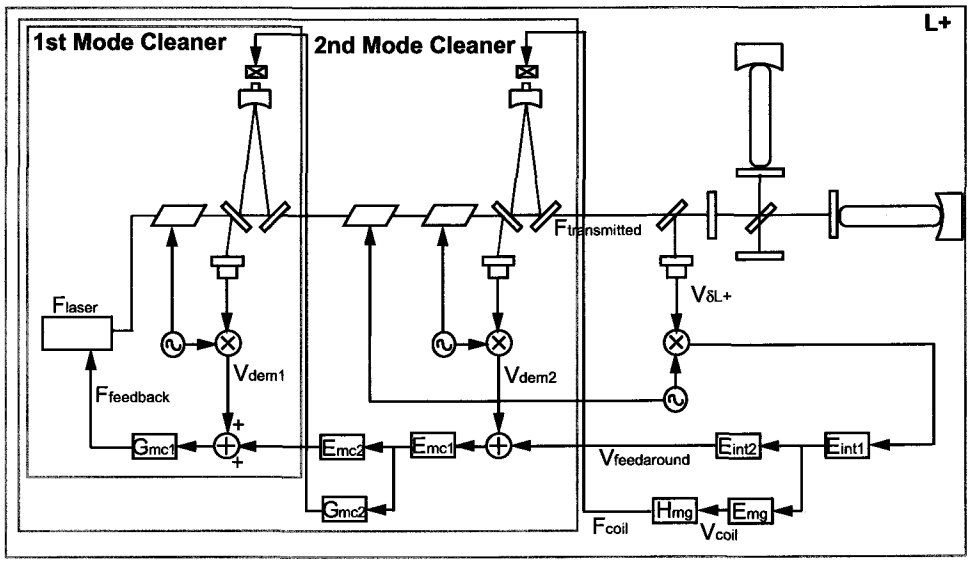

Fig. 2. Servo control topology for laser frequency stabilization.

Opt. **36**, 1446 (1997).

[2] S. Nagano, et al., Rev.Sci.Instrum. **73**, No 5, 2136 (2002).

[3] B. J. Cusack et al, Appl. Opt. 43, 5079 (2004)

[4] S. Telada and the TAMA collaboration, *Gravitational waves and experimental gravity*, Proc. of XXXIVth Rencontres de Moriond, 213 (1999).

9. Output Optical System

[Author: MORIWAKI, Shigenori]

Advanced Materials Science, Univ. of Tokyo, Kashiwa, Chiba 277-8561

The gravitational wave signal and other important signals to maintain the optimal operating point of the main interferometer are extracted from the output optical ports of the interferometer.

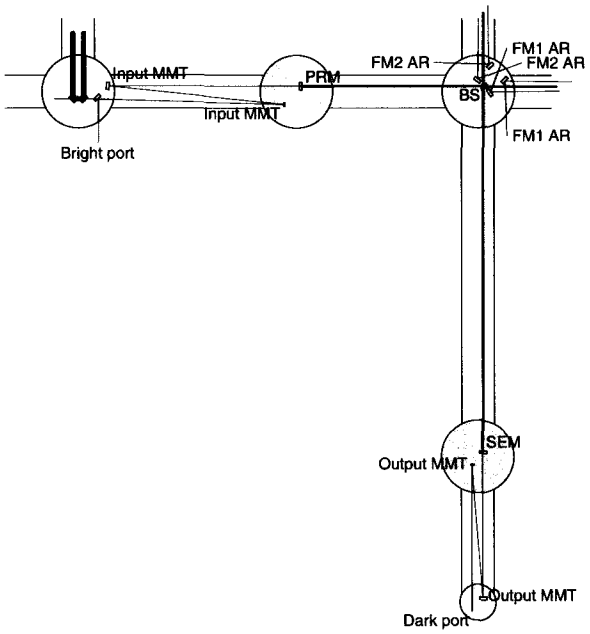

Fig. 1. Schematic layout of the optical output ports of the main interferometer. BS: beam-splitter, PRM: power recycling mirror, SEM: signal extraction mirror, MMT: mode matching telescope, FM: front mirror (not indicated in this figure area).

Figure 1 shows a schematic layout of the optical output ports. We use three types of optical ports, which are called the dark, bright and pick-off ports. The signal of the pick-off port is composed from the anti-reflection (AR) residual light at the front mirrors. A subsystem, called as an output optical system, consists of the equipment that process the the light signals from the optical ports and convert them to electric signals. The key parts are as follows:

- Photodetectors (PD),
- Output mode cleaner (OMC),
- Mode matching telescope (MMT),
- Wave front sensors (WFS).

For the successful operation of LCGT, we should consider thermal protection, vibration isolation and scattering light treatments. In an ideal Michelson interferometer, since a phase fluctuation on the recombined light does not cause a spurious signal, we do not need any test-mass-grade vibration-isolation in the output optical system. It is well known, however, that the scattered light from the anti-reflection surface of the optical components, or the photo detectors, can cause a degradation of the interferometer sensitivity through a coupling with mechanical vibration around the output optical system. This effect is apparently observed in the TAMA300 experiments. Therefore, we might use reflective optics rather than refractive ones ,and also prepare vibration isolators for the optics in the output optical system. In the following sections we overview the past developments and future perspectives concerning several principal items.

9.1. Photo Detectors

The output power of some ports reaches several hundred of milli-watts, or a few watts in the LCGT interferometer. It is not allowed to use an optical attenuator at the dark port, since optical loss directly leads a degradation of SNR of the gravitational wave signal. Unfortunately, a photodiode that can bare such high power is not currently available. We must therefore divide the light with beam-splitters and introduce these beams to multiple photodiodes in parallel, the photocurrents of which are combined. [1]. Too many divisions, however, cause a problem of scattering light or intrinsic electric noise; we have a trade-off here. We should leave flexibility in the mechanical layout design in order to tune the division number according to the contrast of the main interferometer.

We may encounter some thermal troubles of electric devices if we put photo-detectors in the vacuum tank. To avoid this effect, we will use a protection circuit [2] in the photodiode amplifier. In addition, we are planning to cool the individual photodiode to be protected from thermal damage.

Our aimed value of the quantum efficiency is higher than 0.9, which is typical value of InGaAs photodiodes. We must also pay attention to the RF sensitivity because one of the modulation frequencies in LCGT is higher than that in TAMA (15.235 MHz). We will develop photodiode amplifiers incorporating a technique to realize both a high-dynamic range and a wide bandwidth [3], or a summing technique for RF photocurrent signals [4].

Another important item to be developed is a quadrant photo-detector (QPD) for wave-front sensing. The QPD must be able to sense amplitude variation of light at the modulation frequencies. In several optical ports where RF detection is not desired, we need some special types of photo-detecotors; for example, low-noise photo-detectors for intensity stabilization and CCD cameras or QPDs for transmission light monitoring behind the MMT mirrors.

Parameter		Value
Round trip length		70 mm
Finesse		14
FSR		4282 MHz
Cavity bandwidth		304 MHz
Curvature radius	IC and OC	∞
	EM	230 mm
Reflectivity	IC and OC	0.80
	EM	> 0.99995
Mirror spacing	IC-OC	10 mm
	IC-EM and OC-EM	30 mm
Incident angle	EM	0.167 rad
Beam radius	at waist (horizontal)	166.5 μm
	at waist (vertical)	167.9 μm
	on EM (horizontal)	181.1 μm
	on EM (vertical)	182.1 μm
Geometric factor	horizontal	0.691
	vertical	0.699
Higher-mode interval	horizontal	0.1285
	vertical	0.1266
Suppression ratio	first-order modes	> 16 dB
	second-order modes	> 19 dB

Table 1. Selected parameters of an output mode cleaner for the LCGT requirements. IC, OC and EM denote input coupler, output coupler and end mirror, respectively.

9.2. Output Mode Cleaner

The signal corresponding to the gravitational wave is obtained at the dark port. An asymmetric imperfection of the interferometer can cause a degradation of the fringe contrast at the dark port, and increase the amount of junk light that does not contribute to the signal. This consequently increases the shot noise. This phenomena is expected to be partially relaxed by the mode-healing effect, because the LCGT interferometer contains the RSE cavity. However, the junk light may be increased by thermal distortion or by thermal lensing in the arm mirrors, since the internal light power is extremely high. In such a case, an improvement of the fringe contrast is obtained by using an output mode cleaner [5]. The OMC must transmit both carrier and modulation sidebands as dose the input mode cleaner. We designed the parameters of OMC as shown in Table 1 to be compatible with the LCGT requirements. We made a prototype OMC according to the parameters and evaluate its property combined with a simple Michelson interferometer. The spacer of the OMC consists of a super invar, and forms a triangular cavity with three mirrors. The end mirror is mounted on a spacer through piezoelectric actuators so that the optical path length can be tuned rapidly. This makes it possible to protect the down-stream photo-detectors from a flood of light when the main interferometer turns into the unlocked state.

Figure 2 shows an optical configuration to obtain an error signal of the OMC resonance. Here, we utilize the fact that the error signal is obtained from a change of

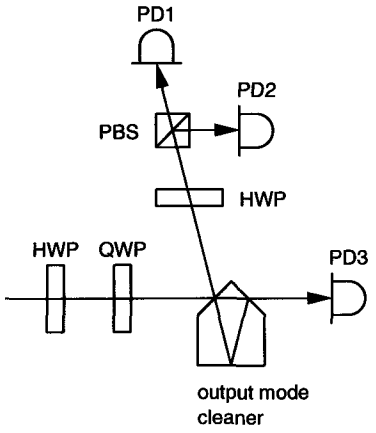

Fig. 2. Error signal extraction scheme for a prototype output mode cleaner. HWP, half wave plate; QWP, quarter wave plate; PBS, polarizing beam-splitter; PD, photo-detector.

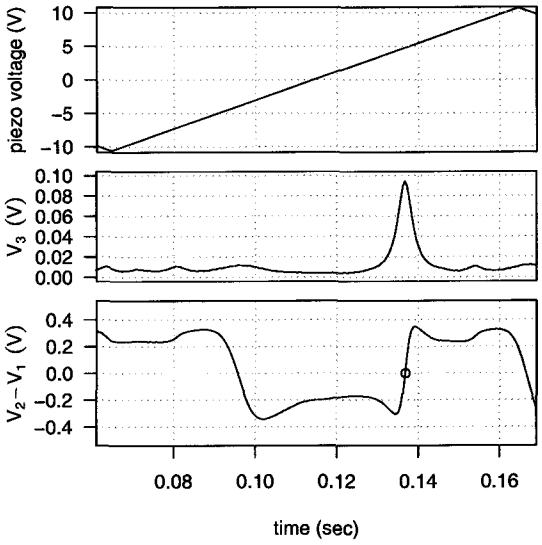

Fig. 3. Scanning property of a prototype output mode cleaner. Voltage V_3 corresponds to the transmission intensity of the cavity. $V_2 - V_1$ is differential signal of PD1 and PD2. A red circle shows a zero-crossing point of difference signal.

the polarization components of reflected light from the cavity if we introduce elliptically polarized light to a planar cavity that consists of an odd-number mirrors. We can obtain a zero-crossing error signal at the resonant points from the difference signal between PD1 and PD2 if we trim the orientation of HWP and QWP at the input port and HWP at the reflection port of OMC appropriately. Figure. 3 shows the reflection intensity and the error signal of the scanning OMC with the applied voltage of the piezoelectric actuator. Voltage V_3 denotes the output signal of PD3 which is proportional to the intensity transmission of the OMC. A voltage of $V_2 - V_1$ is

the differential signal of the OMC reflected intensity separated by PBS. We can see that the error signal, which is zero-crossing at the OMC resonant point, is obtained without RF demodulation or of synchronous detection with cavity length dithering. Using the error signal, we have confirmed simultaneous locking to the dark fringe of the Michelson interferometer and to the resonance point of OMC. For the OMC control loop, the unity gain frequency is measured as 1.3 kHz and the loop gain reaches 40 dB below 10 Hz.

We use piezoelectric actuators for OMC length control, which generally may degrade the thermo-mechanical stability. We have designed a unique configuration for actuator mounting to keep the stability as good as possible. Although the thermo-mechanical property has not yet been measured, we will investigate it in the near future.

9.3. Mode matching telescope

The design concept for an output (dark port) MMT is basically the same as that for an input (bright port) MMT. The requirement for scattering light of the dark port MMT is, however, more tight than that of a bright port MMT as mentioned in the previous section. In TAMA300, off-axis parabolic mirrors are used for the bright-port telescope, and a single convex lens for the dark-port telescope at of the year 2005. The former has room for improvement in the surface roughness and the latter has in the amount of scattered light. It is known that one can decrease the scattered light by replacing lenses with reflecting mirrors. For a telescope using spherical mirrors, astigmatism originating from the oblique incidence can be compensated by adjusting the incident angles of the mirrors [6]. For the LCGT telescopes, we will use spherical mirrors, but will not realize the condition described in [6] because of the layout limitation on the vacuum tanks. We chose small incident angles instead. A telescope for the CLIO 100 m interferometer has been designed based on this concept. We will reflect our knowledge of it to the LCGT telescope design.

Bibliography

[1] N. Uehara *et al.*, Opt. Lett. **19**, 728 (1994).

[2] N. Mio *et al.*, Jpn. J. Appl. Phys. **40**, 426 (2001).

[3] M. B. Gray *et al.*, Rev. Sci. Instrum. **69**, 3755 (1998).

[4] O. Jennrich *et al.*, Opt. Commun. **205**, 405 (2002).

[5] The VIRGO Collaboration, Class. Quantum. Grav. **19**, 1857 (2002).

[6] P. Hello *et al.*, Appl. Opt. **35**, 2534 (1996).

10. Overview of the cryogenic suspension

[Author: UCHIYAMA, Takashi]
ICRR, Univ. of Tokyo, Kashiwa, Chiba 277-8582

A mirror-suspension system requires the following items:

- Realizing a free test-mass.
- Behaving as a good vibration isolation system.
- Attaining low thermal noise.
- Actuating the test-mass.
- Cooling the test-mass.

Figure 1 shows a schematic view of the LCGT mirror suspension system. It consists of a SAS vibration isolation system (in room temperature) and a cryogenic suspension. All the system is installed in a cryostat. Look at the section, "Seismic isolator" for SAS and the section, "Cryogenic system" for the cryostat. The cryostat is cooled by vibration-free pulse-tube refrigerators and the detail of the refrigerators is described in the section, "Cooling system".

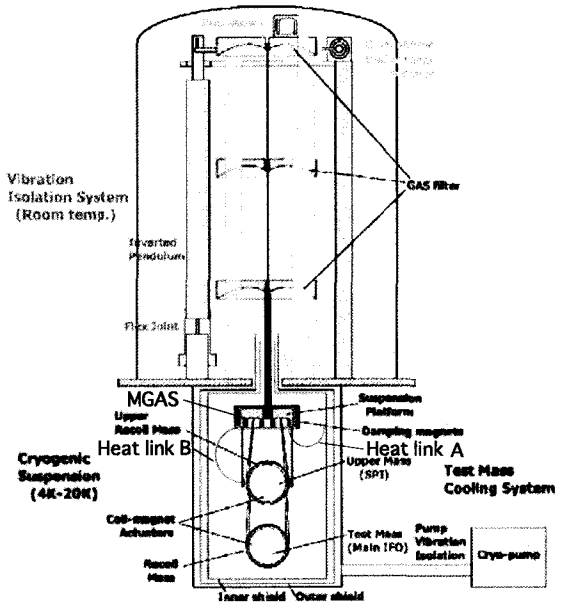

Fig. 1. Schematic view of the LCGT suspension system.

The cryogenic suspension is suspended by a low thermal conductivity wire from the SAS and installed in the cryostat. A Bolfur[1] wire of 1.5 mm in diameter is one of candidates. A Bolfur wire of 0.1 mm in diameter is tested for the suspension system of Cryogenic Laser Interferometer Observatory (CLIO). This cryogenic suspension system consists of six masses, a suspension platform, a damping magnet stage, an upper mass, a recoil mass for the upper mass, a test mass and a recoil mass for the test mass.

The substrate of the test mass is a block of sapphire cylinder,ϕ 250 mm in diameter, 150 mm in thickness and 30 kg in weight. The substrate is polished and optically coated. The mechanical Q factor of the substrate[2] and the energy dissipation of the coating[3] at a cryogenic temperature have been already measured and they are 10^8 and 4×10^{-4}, respectively. According to these experimental results and material properties of sapphire, we have confirmed that mirror thermal noise satisfies the required sensitivity of LCGT when the mirror is cooled at 20 K. An investigation of the optical properties of sapphire is on-going (the section "Cryogenic mirror"). Polishing and coating techniques were also established during the development of the mirror for CLIO. The substrate supplier is Crystal Systems Inc. USA.

The mirror is suspended by four sapphire fibers from the upper mass. The sapphire fiber provides a high mechanical Q factor of 5×10^6[4]. As the result, we obtain a high pendulum Q factor of 10^8. The mirror is heated by the laser beam absorption. An estimation of the heat is 290 mW in the near mirror. The detail is described in the section, "Heat link design". The sapphire fiber provides not only high Q factor but also high thermal conductivity. The heat is transfered to the upper mass by thermal conduction[3]. The suspension length is 400 mm and the diameter of sapphire fiber is 1.8 mm. Such a thick fiber is difficult to be bent for suspending the mirror. A sapphire-sapphire bonding technique has been developed for attaching the fiber to the mirror and see the section, "Suspension of cryogenic mirrors - application of sapphire bonding for constructing suspension structure".

Coil-magnet actuators are used for length and alignment control for the mirror. The coils are installed in the recoil mass. The recoil mass weighs 30 kg as much as the mirror. The recoil mass is suspended from the upper mass by four sapphire fibers or aluminum wires. Since heat of the recoil mass is much less than that of the mirror, temperature gradient between the upper mass and the recoil mass is negligibly small.

The upper mass is also made of sapphire and forms a part of a suspension point interferometer (SPI). The SPI is a kind of active vibration isolation system that is described in the section, "Suspension Point Interferometer". The purpose of the SPI is reducing the vibration induced by heat links that transfer the heat in the suspension to the radiation shield of the cryostat. The importance of the SPI is shown in the section, "Heat link design". Since the laser power for the SPI is small, the absorption heat of the upper mass is much less than that of the test mass.

Dimensions of the upper mass is the same as that of the test mass. The upper mass is suspended from the suspension platform through MGASs, vertical springs. Resonant frequency of the MGASs are 0.7 Hz. The MGAS is introduced in the section, "Seismic isolator". The purpose of the MGASs is to reduce the vertical vibration noise coming from the heat link. Since the MGASs do not have high thermal conductivity, heat links between the upper mass and the suspension platform are necessary to transfer the heat that comes from the mirror. The heat links (heat link B in fig. 1) are made of high purity aluminum wires.

Since the upper mass also needs to be controlled, there is a recoil mass for the coil-magnet actuator. This recoil mass is also suspended from the suspension platform by four sapphire or aluminum wires. The mass is 30 kg that is the same as other masses introduced in the above.

The suspension platform and the damping magnet stage are independently suspended from the final GAS filter of SAS. The suspension platform is suspended by the low thermal conductivity wires, as mentioned above. The magnet stage suspended by G-10 rods. G-10 is also low thermal conductivity material. The motion of the suspension platform is damped by eddy current damping method.

There is another heat link (heat link A in fig. 1) between the platform and the inner radiation shield. Since the shield vibrates as much as the ground level, stiffness of the heat link has to be small to avoid disturbing the mirror from the shield vibration. So the heat link A needs to have both sufficient high thermal conductivity and sufficient small mechanical stiffness. This heat link is also made of high purity aluminum wires. The magnet stage is cooled by another heat link (not shown in fig. 1). The heat generated in the mirror passes the sapphire fiber, from the heat link B to the heat link A and goes to the inner shield that is cooled at 8 K. The current heat link design can afford a heat power of about 1 W with a sufficient vibration isolation. Detail of the design is shown in the section, "Heat link design".

Even though the LCGT cryogenic suspension consists of many advanced techniques, its realization is not adventure, because all technical issues have been already investigated and tested by experiments and CLIO as described in the following sections.

Bibliography

[1] UNITIKA LTD.

[2] T. Uchiyama et al., Phys. Lett. A. **261**, 5 (1999).

[3] K. Yamamoto et al., Class. Quantum Grav. **21**, S1075 (2004).

[4] T. Uchiyama et al., Phys. Lett. A. **273**, 310 (2000).

11. Cryogenic system

[Author: UCHIYAMA,Takashi]
ICRR, Univ. of Tokyo, Kashiwa, Chiba 277-8582

11.1. Composition of the cryogenic housing system

The LCGT cryogenic housing system consists of three items: a cryostat, cryogenic pipes and refrigerator units.

LCGT uses cryogenic cooled mirrors in order to reduce the thermal noises. The design temperature of the mirrors is 20 K. The cryostat is a mirror tank and has a cryogenic environment inside. The LCGT cryostat has two layers of radiation shields (outer and inner), which are cooled by two sets of 2-stage 4K 1 W pulse-tube refrigerators. To these refrigerators is applied a vibration-isolation method. The refrigerators are installed in other small chambers (refrigerator units) for vibration isolation, and thermal conductors connect between the shields and the refrigerators (see cooling system section). Table 1 gives the target temperature of the cryogenic systems.

Item	temperature
Inner shield	8 K
Outer shield	100 K
Cryogenic pipe	100 K

Table 1. Target temperatures of the cryogenic systems.

Figure 1 shows an image of the LCGT cryostat and Fig. 2 shows a schematic view of the mirror suspension system. The mirror suspension system is installed in the cryogenic area of the cryostat, which is surrounded by an inner radiation shield. The suspension system is isolated by SAS installed in the room-temperature area of the cryostat. SAS stands on a stage built in the cryostat. LCGT uses a suspension point interferometer (SPI) for vibration isolation of heat links (see SPI section). This means that two laser beams pass inside the inner shield.

The cryogenic pipe is a 20 m length of vacuum pipe with a radiation shield. The purpose is to reduce the radiation heat and to avoid contamination of the mirror by particles from the room-temperature area. The radiation shield is maintained at a temperature of 100 K. The shield is cooled by two sets of pulse-tube refrigerators that have a cooling power of 80K, 100 W and are supplied with a vibration-isolation method. Since cryogenic pipes are necessary for both sides of the cryostat and two laser beams are used for one interferometer, four cryogenic pipes are attached to the cryostat.

LCGT has two sets of laser interferometers. We need to install an independent vacuum system for each interferometer for maintenance, but the interferometers share 3 km of vacuum pipe because of cost. Therefore, four laser beams pass through a vacuum pipe of 1000 mm diameter. Figure 3 shows the mirror arrangement. Since the beam separation of the interferometers is only 600 mm, all four laser beams pass inside the cryostat. Figure 4 shows a schematic view of near tanks of two interferometers and Fig. 5 shows the arrangement of all cryogenic system.

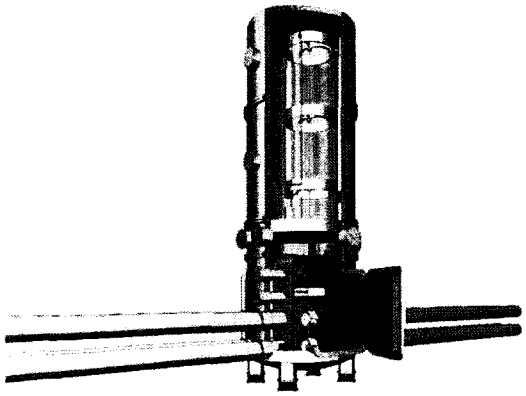

Fig. 1. Image of LCGT cryostat.

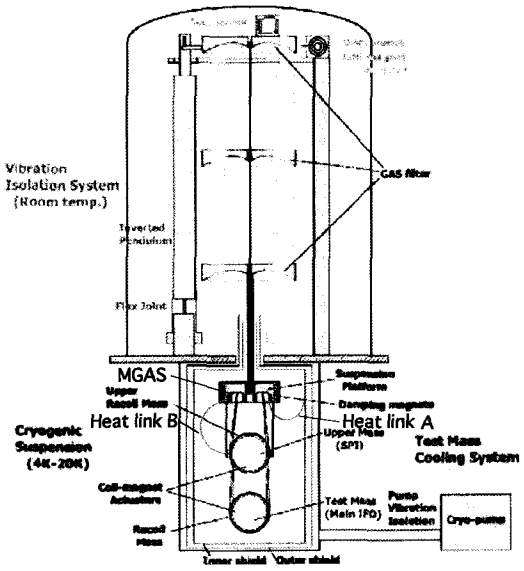

Fig. 2. Image of the LCGT suspension.

11.2. Dimensions of the cryogenic system

Here, summary figures of a cryostat made by TOSHIBA company, which is the maker of CLIO cryostat, are presented. Figures 6, 7, 8, 9, 10 show a front view, an inside view, a side view, a top view and a full

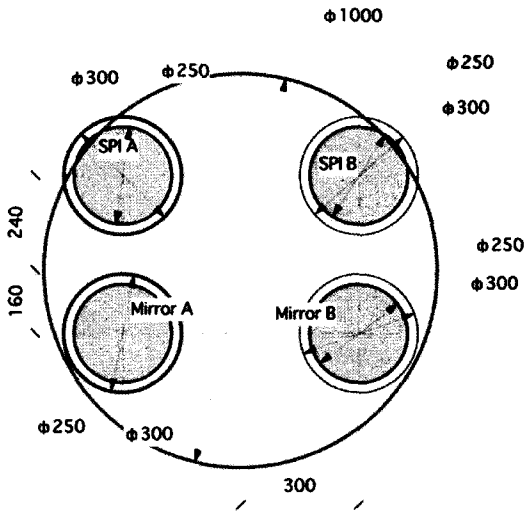

Fig. 3. Mirror arrangement. Four laser beams pass through the 3 km vacuum pipe. This shows that the beam separation between two interferometers is 600 mm. The mirror diameter is 250 mm and the diameter of radiation shield in the cryogenic pipe is the same. The diameter of the cryogenic pipe is 300 mm. The length of the fiber suspending the main mirror is 400 mm.

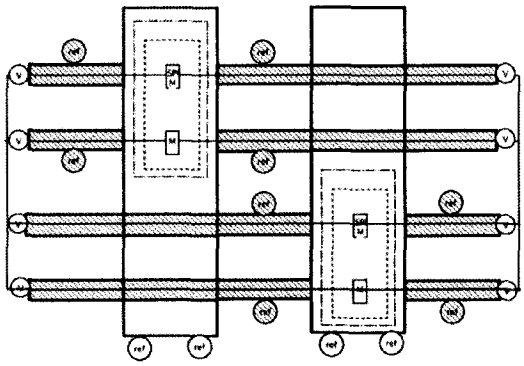

Fig. 4. Schematic view of near tanks for two interferometer, A and B. "V" means a gate valve. "ref" means a refrigerator. The blue dashed area is a cryogenic pipe. The red dashed area is a vacuum pipe, which is not cryogenic. This figure shows that two laser beams pass through the inner shield, and the mirrors and another two beams pass through a vacuum pipe that is inside of the cryostat. Thus, we can open the cryostat without breaking the vacuum of another interferometer.

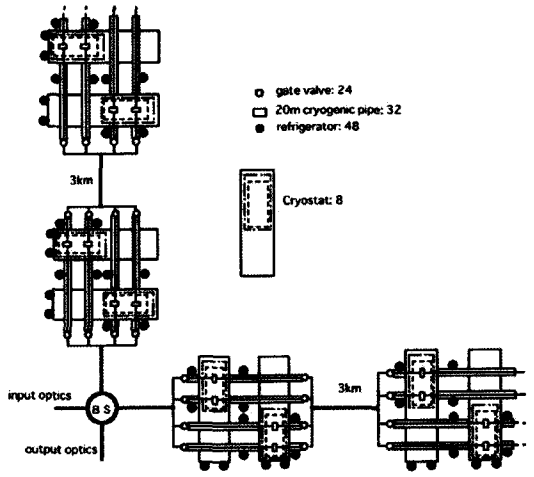

Fig. 5. Schematic view of all cryogenic systems of LCGT. The cryogenic system consists of 8 cryostats, 32 cryogenic pipes and 32 refrigerators.

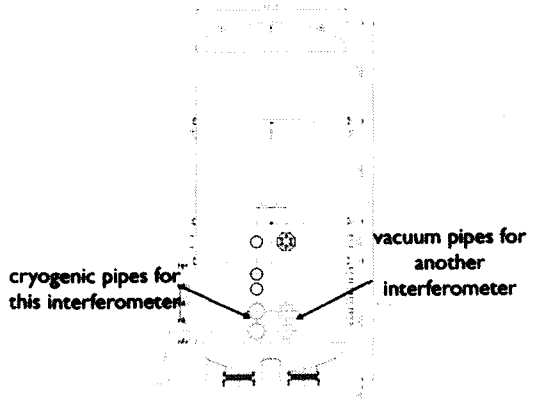

Fig. 6. Front view of the cryostat. Four ducts for the laser beams are shown. Height of the cryostat is 7200 mm. The main beam goes through the height of 1000 mm from the floor level.

side view of two systems, respectively. Table 2 summarizes the dimensions of the cryostat. The volume of the inner shield is determined by the size of the mirror suspension. The volume of the room-temperature area depends on the design of the SAS. The maximum scale of the cryostat design needs consideration of the transportation from the mine entrance to the site.

11.3. Result of the CLIO cryostat and Heat estimation

Fundamental techniques for the LCGT cryogenic system have been developed in the construction of CLIO. Figure 11 shows the result of a cooling test of the CLIO cryogenic system, and that our requirement is satisfied. Based on the result of CLIO, we can estimate the heat load of the LCGT cryogenic system. Table 3 gives an evaluation of the heat load in the CLIO cryogenic system and an estimation of LCGT. Since the heat load

Item	Value of LCGT	Value of CLIO
Height of the cryostat	7200	2500
Diameter	3000	
Width		1500
Depth		920
Height of the inner shield	2000	800
Width	1460	
Depth	1000	
Diameter		800
Diameter of the cryogenic pipe	300	400
Diameter of the radiation shield	250	300
Length of the cryogenic pipe	20 m	5 m
Height of the beam axis	1000	800

Table 2. Dimensions of the cryostat.

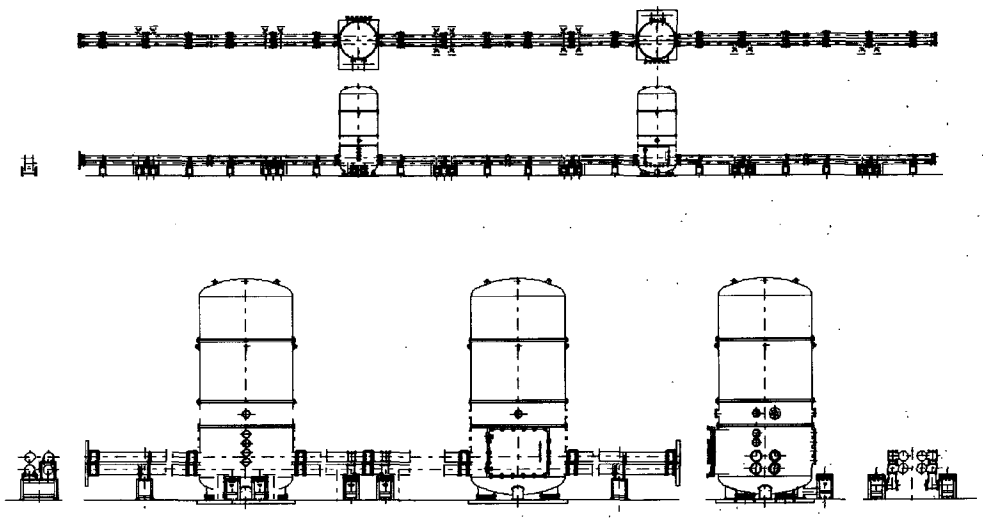

Fig. 10. Full side view of two cryogenic systems.

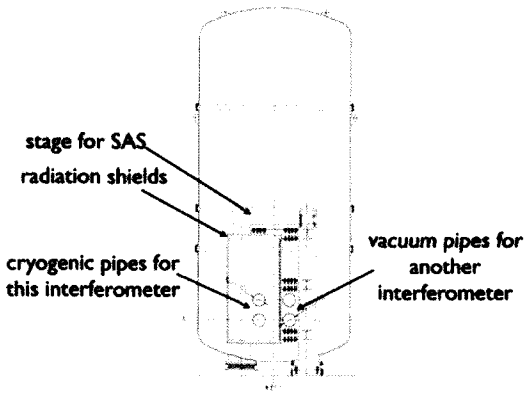

Fig. 7. Inside view of the cryostat. Radiation shields and two laser beams are introduced. Another two laser beams pass through the vacuum pipe in the cryostat.

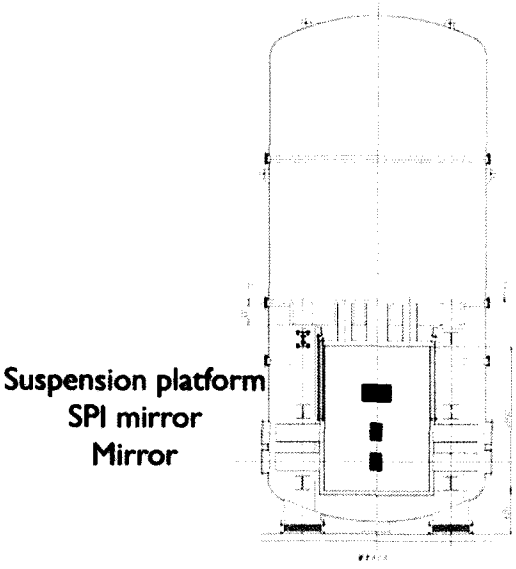

Fig. 8. Side view of the cryostat.

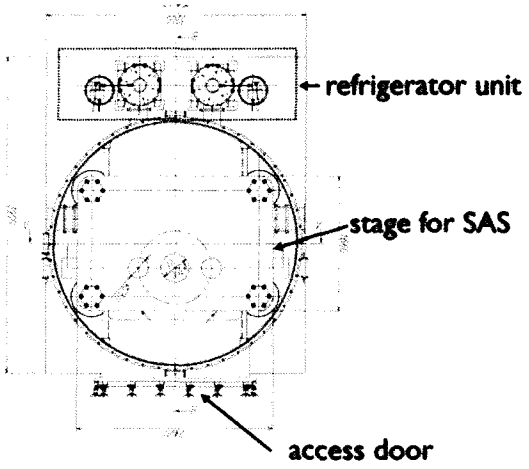

Fig. 9. Top view of the cryostat. Two sets of refrigerator units are shown. We can access the inner shield from a side access door.

Item	CLIO	LCGT
Inner shield	0.6 - 0.9 W	2 W =1 W + 1 W
Outer shield	16 - 20 W	80 W = 20 W × 4
Cryogenic pipe	22 - 25 W	83 W = 25 W × 3.3

Table 3. Heat load in the CLIO system and the LCGT system. The heat load in the CLIO system is evaluated from the achieved temperature of the refrigerators. The heat load of the inner shield consists of the shield, itself, and heat from the mirror of 1 W. The heat in the outer shield and the cryogenic pipe is dominated by radiation. Therefore, it is proportional to the surface area of the shield. "4" and "6.6" are the ratios of the surface area for each item.

of LCGT is not small, multi-use of the refrigerators is needed to satisfy the estimated cooling power. Table 4 summarizes the parameters of the refrigerators.

We measured the vibration at the stage in the CLIO cryostat with refrigerators in operation. Figure 12 shows the result of the vibration measurement[1]. We confirmed that the refrigerator is compatible with the laser interferometer.

The vacuum system for the CLIO system consists of a 1000 L turbo-molecular pump and a rotary pump; 10^{-5} Pa has achieved.

11.4. Summary

We have designed the LCGT cryogenic systems based on knowledge and experience from the development of CLIO. Even though the heat load in LCGT is larger than tht in CLIO, we confirmed that a multi-use of the pulse-tube refrigerators can overcome this problem.

Bibliography

[1] K. Yamamoto, Private communication.

Refrigerator	cooling power	number for each system	Total number for LCGT
4K 2 stage pulse-tube refrigerator	1 W at 4 K	2	16
4K 2 stage pulse-tube refrigerator	30 W at 40 K		
80 K pulse-tube refrigerator	100 W at 80 K	4	32

Table 4. Parameters of the refrigerators. Note that each cryostat has four cryogenic pipes.

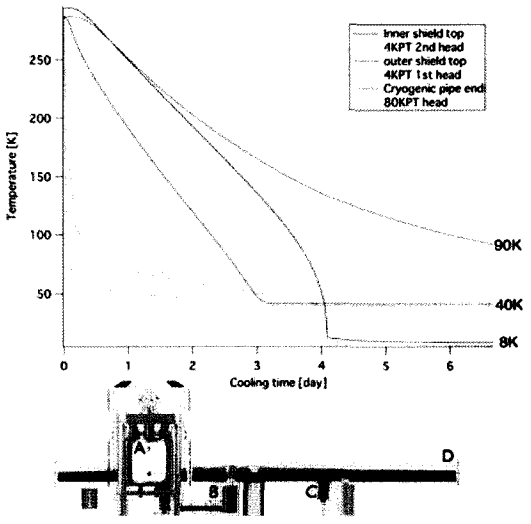

Fig. 11. Temperature changes with time in the CLIO cryogenic system. The figure in the bottom is an inside view of the system. The measurement point of "Inner shield top" and "Outer shield top" are "A" in the figure. "4KPT 2nd head" and "4KPT 1st head" are "B". "80KPT head " is "C". "Cryogenic pipe end" is "D". The graph shows that the system satisfies the requirement.

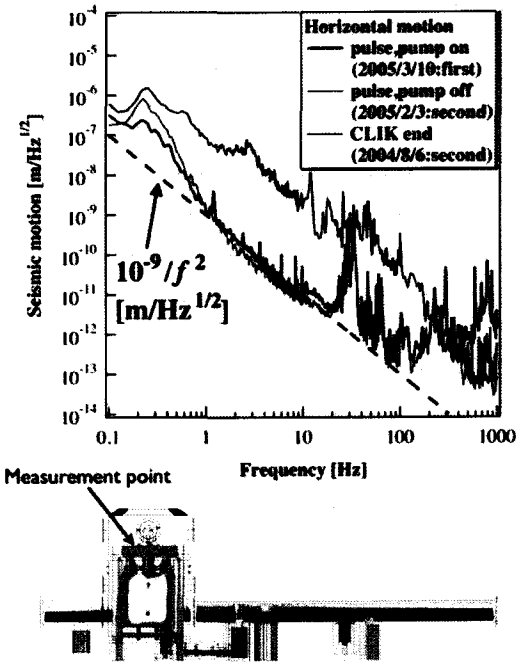

Fig. 12. Seismic vibration at the suspension stage in the CLIO cryostat in Kamioka mine. The red and blue lines show the seismic motion with and without operating the pulse-tube refrigerators and the vacuum pump. The solid black rep curve represents the vibration in the end tank of CLIK (Cryogenic Laser Interferometer located in Kashiwa (suburb of Tokyo)). The seismic vibration in the Kamioka mine is 100-times less than that of Kashiwa. The refrigerators did not increase the vibration below 200 Hz.

12. Heat link design

[Author: UCHIYAMA, Takashi]
ICRR, Univ. of Tokyo, Kashiwa, Chiba 277-8582

12.1. Heat link

The main mirrors of the interferometer are always heated. In order to keep the mirrors at 20 K, heat must be taken away continuously, and thermal conduction is the only method. Therefore, heat links from the mirror to the radiation shield in the cryostat (see section on cryogenic systems) is necessary. Figure 1 shows a schematic view and symbol view of the LCGT suspension system. In order to design the heat link, we must know how much heat is transferred and how much the mirror is vibrated by the mechanical noise induced by the heat links.

Laser absorption dominates the heat in the mirror. The absorption consists of absorption in the substrate and in the coating. Table 12.1. shows corresponding parameters for evaluating the heat production and the heat transfer. Obviously, the near mirror is much more heated than the end mirror. Therefore, we designed heat links for the near mirror. The design is to decide the number, diameter and length for the heat link wire. High-purity (99.9999%) aluminum wire is used for the heat link wire. Figure 2 shows the thermal conductivity[1].

Figure 3 shows the current design of the heat links. Figure 4 shows the seismic noise. We make a point mass model of the mirror suspension, as shown in Fig. 1, and evaluate the seismic noise in three degrees of freedom. Cross coupling of vertical (Z) to the light axis (X) and the perpendicular (Y) to the light axis (X) is assumed to be 1%. The seismic motion of the site is represented as $10^{-9}/f^2[\mathrm{m}/\sqrt{\mathrm{Hz}}]$. SPI is the active vibration isolation, and has an important roll for the heat link. Figure 5 shows the effect of SPI, a vibration isolation ratio of 40 dB in the light-axis direction is assumed.

We have designed heat links that satisfy the requirement for sensitivity and to cool the mirror with sufficient margin. The current project, Cryogenic Laser Interferometer Observatory, adopts "U"-shape heat links. It will provide much information to finish the heat-link design for LCGT.

Item	Value
Diameter of the mirror	250 mm
Thickness	150 mm
Laser absorption ratio	20 ppm/cm
Laser absorption in the coating	0.1 ppm
Laser power in front of the power recycling mirror	75W
Power recycling gain	11
Finesse	1550
Absorption in the substrate	250 mW
Absorption in the coating	40 mW
Heat in the near mirror	290 mW
Heat in the end mirror	40mW

Table 1. Heat production in the mirrors by laser light absorption.

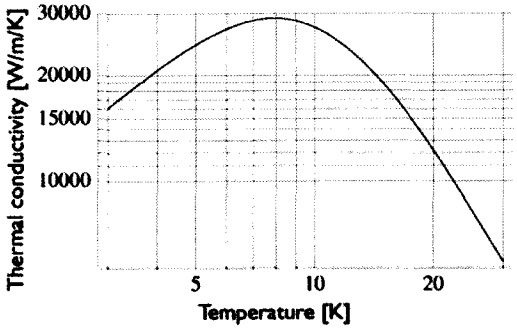

Fig. 2. Thermal conductivity of high purity (99.9999%) aluminum wire.

Bibliography

[1] K. Kasahara et al., J. Cryo. Soc. Japan. **39** 25 (2004).

[2] T. Uchiyama et al., Phys. Lett. A. **273**, 310 (2000).

[3] T. Uchiyama et al., Phys. Lett. A. **242**, 211 (1998).

[4] T. Tomaru et al., Phys. Lett. A. **301**, 215 (2002).

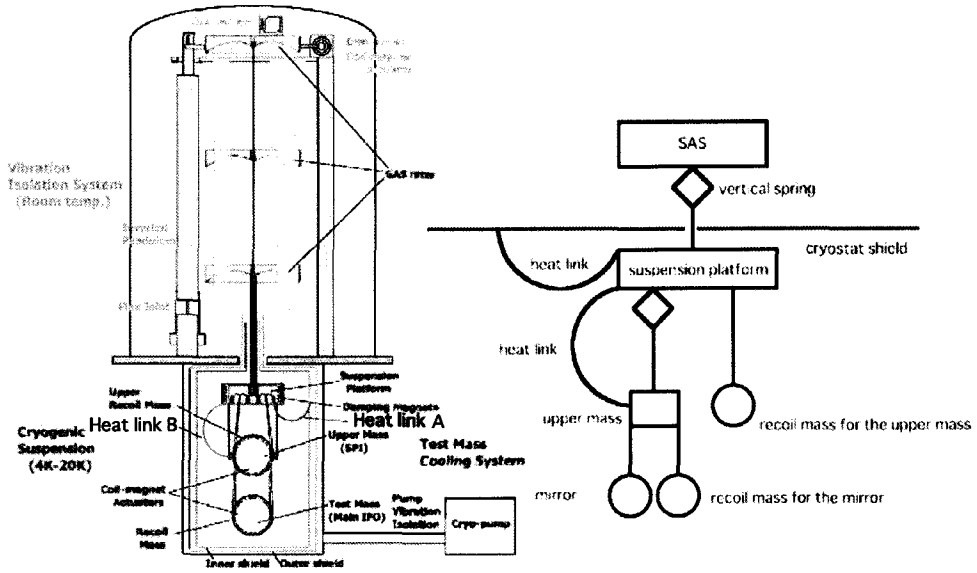

Fig. 1. Schematic view and symbol view of the LCGT suspension system. The triple mirror suspension system in the cryogenic area is suspended from an SAS vibration isolation system. The mirror suspension consists of five masses. "U" and "C" shape heat linksare assembled. The roll of the heat link is to transfer heat. It is, however, heat link also transfers vibration. Therefore, we must take into account any mixing of vibration at the suspension platform. Especially, the heat link A requires a perfect design, because the radiation shield vibrates as much as the ground. Theupper mass is the mirror for the Suspension Point Interferometer (SPI). SPI is a kindof active vibration isolation, and cause vibration due to the heat links calmdown.

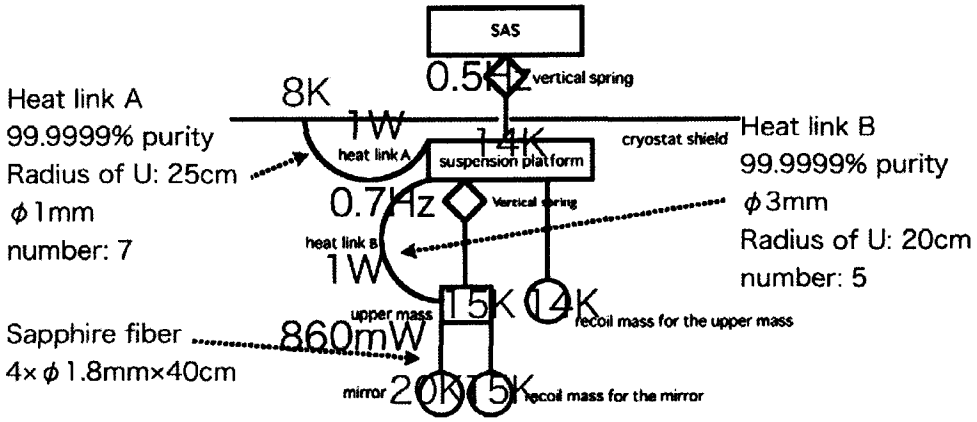

Fig. 3. Current design of the heat link. All heat paths from the mirror to theradiation shield have a capacity of transferring heat of about 1W. Since theestimated heat is 290 mW in the near mirror, this design has about a 200% safetymargin. Four sapphire fibers are used as the final suspension. The sapphire fibersprovide high mechanical Q pendulum of 10^8 and high thermalconductivity[2][3][4]. Each recoil mass that houses actuators for mirror control is suspended by aluminumwires.

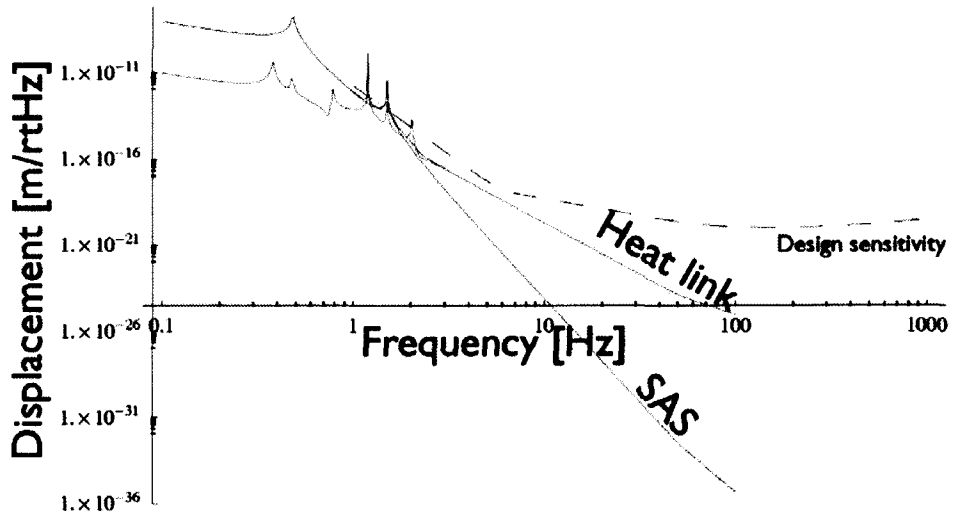

Fig. 4. Seismic noise of LCGT. There are two routes for the seismic motion to reachthe mirror. One is the route through the SAS from the ground. Another one comes fromthe radiation shield through the heat links. In order to estimate the total seismicnoise, we evaluate the seismic noises due to both routes and then make a square rootsum. The line "Heat link" and "SAS" show the seismic noise due to the vibration ofthe radiation shield and the ground seismic motion, respectively. Vibration at theradiation shield is assumed to be the same as the ground. Transfer function of SASis assumed the proper one. The total seismic noise level at 10 Hz is $2 \times 10^{-20}\mathrm{m}/\sqrt{\mathrm{Hz}}$, and is dominated by the vibration that comes from the radiationshield. The LCGT design sensitivity at 10 Hz is $6 \times 10^{-19}\mathrm{m}/\sqrt{\mathrm{Hz}}$, so this noise is 30-times smaller.

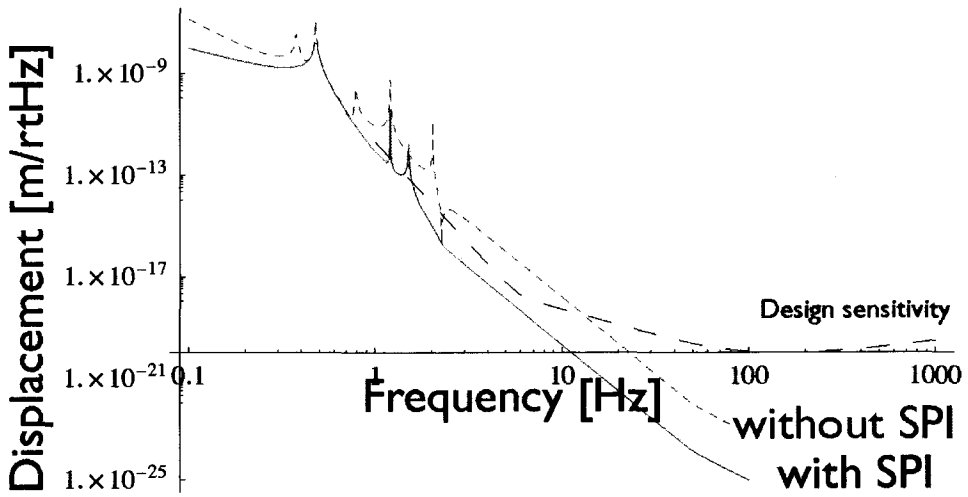

Fig. 5. Seismic noise with and without SPI. The attenuation ratio of SPI is 40 dB only in the light axis direction. The figure shows the importance of SPI. With SPI, vertical motion dominates the seismic noise. Without SPI, vibration in the lightaxis dominates. This is the reason why different resonant peaks appear with and without SPI.

13. Cooling System

[Author: TOMARU, Takayuki]
KEK, 1-1 Oho, Tsukuba, Ibaraki, 305-0801

13.1. Design and Specification

A technical issue for the cooling system is to make the cooling consistent with the vibration-isolation of the mirrors. Figure 1 shows a schematic view of the LCGT cooling system. Conduction cooling is a promising technique to cool the mirrors below 20 K in the high-vacuum system of LCGT. Heat conduction of sapphire suspension fibers is used to cool the mirrors[1, 2], and heat links made of pure metal wires[3] are attached to the pendulum. Since the attachment of the heat link wires to the pendulum reduces the performance of vibration-attenuation of the pendulum, it has to be prevented by introducing a suspension point interferometer (SPI, see SPI section) and a vibration isolator for the heat links (see Cryogenic Suspension section).

A cryocooler is also a promising device to cool the mirrors while keeping a long observation time of LCGT. Cryocoolers are required to have both sufficient cooling power and a small vibration level. The specifications for the LCGT cooling system are noted in the following.

13.1.1. Cooling Power

Figure 2 shows the estimated heat load in a cryogenic area of LCGT. The heat loads to the 8K area, the 100 K area and the 100 K beam duct are 0.82 W, 8.2 W and 80 W, respectively. When a safety factor of 2 is taken, the required cooling powers of the cryocoolers are 2 W for the 8 K area, 100 W for the 100 K area and 60 W for the 100 K beam duct. For cooling of the 8 K and the 100 K areas, the 2nd cold-stage (4 K stage) and the 1st cold-stage (40 K stage) of a 4 K cryocooler are used, respectively. To cool the 100 K beam duct, an exclusive 100 K cryocooler is introduced.

13.1.2. Vibration Level

Vibration of the cryostat has to be at the seismic vibration level in Kamioka mine (LCGT site). The seismic vibration level in Kamioka mine is about $10^{-9}/f^2\,[\mathrm{m/Hz^{1/2}}]$ in a frequency range of more than 1 Hz. Therefore, the specification of the cryocooler vibration level is $10^{-9}/f^2\,[\mathrm{m/Hz^{1/2}}]$.

13.2. Present Technology

13.2.1. Cryocooler

As typical 4 K cryocoolers, there are a Gifford-McMahon (GM) type[4] and a pulse-tube (PT) type[5]. GM cryocoolers are widely used in science and industries, and are reliable for long operation. The typical cooling power of a 4 K GM cryocooler is 1 W at the 4 K stage (2nd stage) and 40 W at the 40 K stage (1st stage). PT cryocoolers have recently been used in practice. It is expected that their vibration levels are smaller than those of GM cryocoolers, since PT cryocoolers have no mechanically moving parts in the cold-head; in contrast, GM cryocoolers have a mechanical piston (displacer). The typical cooling power of a 4 K PT cryocooler is 0.5 W at the 4 K stage and 15 W at the 40 K stage.

Since there was no precise measurement of vibrations for these cryocoolers, we investigated the vibration levels of these commercial cryocoolers to design the LCGT cooling system[6]. From this measurement, we showed that these cryocoolers had two types of vibrations; the whole cold-head vibration come from the reaction of a displacer and a motor to drive a valve, and the cold-stage vibration come from an elastic deformation of the cylinder due to the oscillation of working gas. We also found that the cold-head vibration of a PT cryocooler was two orders of magnitude smaller than that of a GM cryocooler, although the cold-stage vibration was almost the same level (10 μm at an operating frequency of 1 Hz) for both cryocoolers. Even in the case of a PT cryocooler, its vibration level was three orders of magnitude larger than the specification for the LCGT cryocooler.

13.2.2. Development of Small Vibration Cryocooler System for the CLIO

13.2.2.1. **Concept** Based on the above study, we have already developed a small-vibration cryocooler system, which has a comparable vibration level with the seismic vibration in Kamioka mine[7, 8]. This cryocooler system is used in a prototype cryogenic interferometer of the LCGT, called CLIO. Figures 3 and 4 show our small-vibration cryocooler system.

SRP-052A, manufactured by Sumitomo Heavy Industries Ltd., was used as the basic PT cryocooler.

To reduce the cold-head vibration of the PT cryocooler, we introduced a rigid frame to support the cold-head, named 'support frame'. The cold-head was mounted on a support frame and a welding bellows was connected between the cold-head and the cryostat. A rotary valve unit, which could generate large vibrations, was not attached to the cold-head directly, but was fixed onto an independent heavy table (rotary valve table). A connecting tube between the cold-head and the rotary valve unit was also fixed on the rotary valve table. Flexible tubes from the compressor were converted to rigid pipes, and connected to the rotary valve unit. The pipes were also clamped onto the rotary valve table.

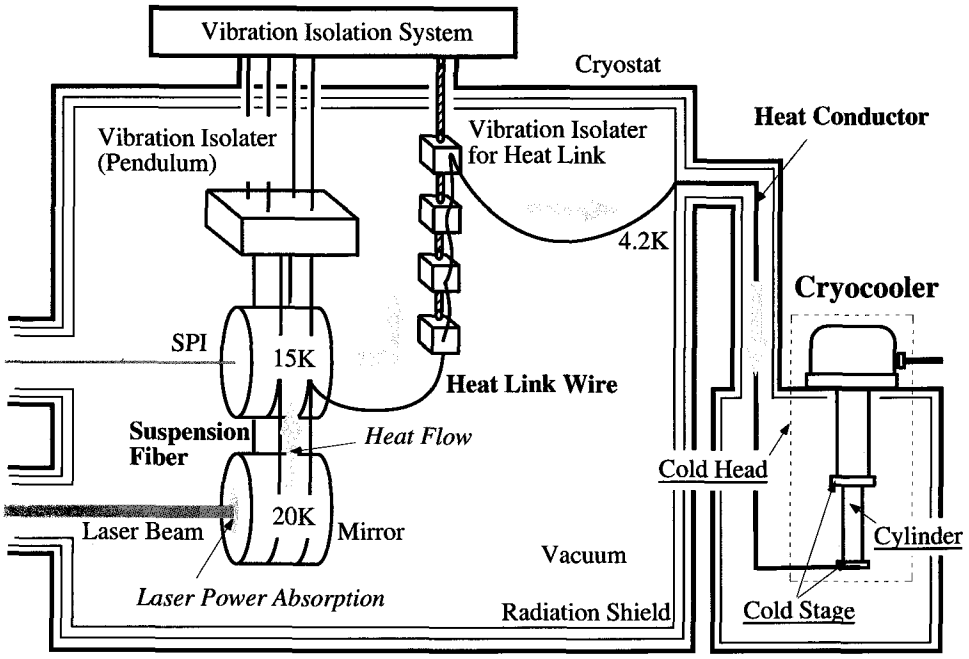

Fig. 1. Schematic view of the LCGT cooling system.

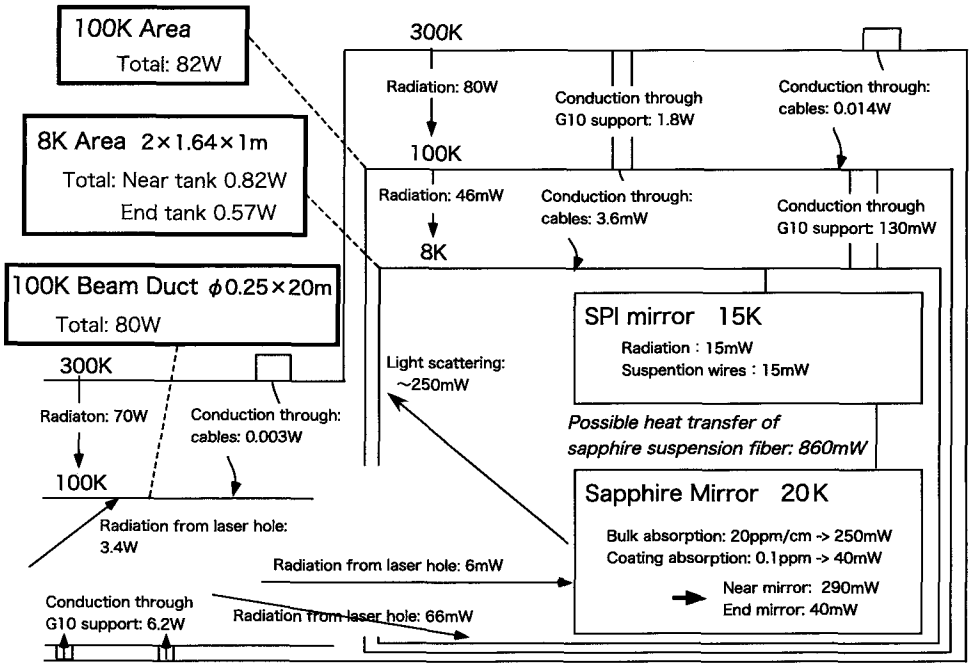

Fig. 2. Estimated heat load in the cryostat.

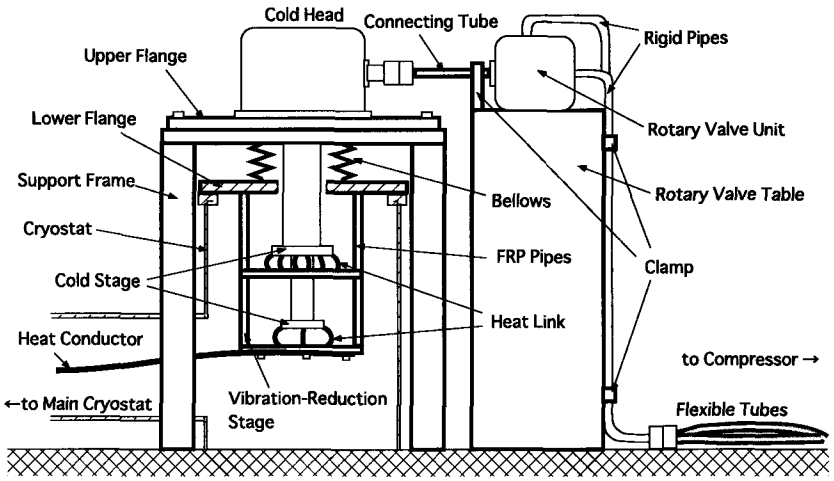

Fig. 3. Schematic view of a small vibration cryocooler system based on an commercial PT cryocooler.

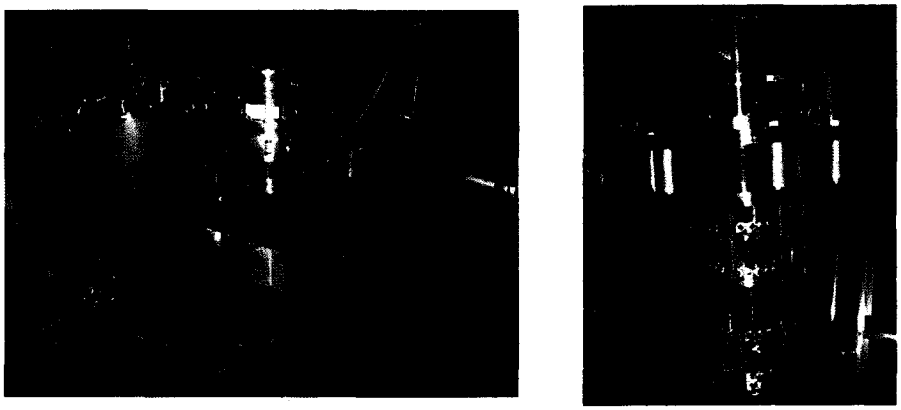

Fig. 4. Photograph of a small vibration cryocooler system. (a) Cold-head and valve unit, (b) Vibration reduction stage of the cold-stage.

To reduce the cold-stage vibration, we used a rigid table, named 'vibration-reduction stage'. The vibration reduction of the cold-stage by using the vibration-reduction stage has been reported[9]. An improved point concerning our vibration-reduction stage is that we set it under a lower flange of the bellows (named 'lower flange'), which was installed on the cryostat. Since the lower flange has been quiet, owing to being separated from the cold-head, we can expect an absolute reduction of the cold-stage vibration by the vibration-reduction stage. The vibration-reduction stage consisted of eight alumina-FRP pipes, a copper plate and about forty heat-link cables for each stage. The reason why we used alumina-FRP was that it had a smaller thermal conductivity at 4K, and a two-times larger Young's modulus than those of glass-FRP. As the heat link, we used pure aluminum stranded cables for both stages.

13.2.2.2. **Vibration Level** Figure 5 shows the measured vibration-spectra of the small-vibration cryocooler system. The cold-stage vibration of our system at 1 Hz, which comes from an elastic deformation of the cylinder due to oscillation of working gas, was reduced by three orders of magnitude from that of the basic PT cryocooler by introducing the vibration-reduction stage. The cold-head vibration over the 100 Hz frequency range[1] was also reduced by over three orders of magnitude by introducing the support frame, the soft bellows and separation of the valve unit from the cold-head. From a detail analysis, it was confirmed that a vibrational peak at around 100 Hz came from the resonance of a mount-jig of the accelerometer. Therefore, we concluded that the vibration level of our cryocooler system was almost the same as the seismic vibration level in Kamioka mine.

13.2.2.3. **Cooling Power** Figure 6 shows the measured heat-load map of the cryocooler system. For a typical heat-load condition (0.5 W for the 2nd stage and 15 W for the 1st stage), the achieved temperatures of the basic PT cryocooler were 4.0 K at the 2nd stage and 42 K at the 1st stage. On the other hand, those of the cryocooler system were 4.4 K at the 2nd stage and 44 K at the 1st stage. Therefore, the cryocooler system kept almost the same cooling power as the basic PT cryocooler.

These vibration and cooling performances of the cryocooler system were sufficient to achieve the requirements for the CLIO.

13.2.2.4. **100 K cryocooler system** A 100 K PT cryocooler system was also introduced to cool the radiation shield of the beam duct. This system consists of an 100 K PT cryocooler with one stage and the same vibration-reduction system as the 4 K cryocooler system. This cryocooler system also had almost the same vibration level as the seismic vibration level in the Kamioka mine and 60 W cooling power at 100K. These performances were sufficient for the CLIO.

[1] Floor level of the cold-head vibration of the basic PT cryocooler below 100 Hz frequency range was not the seismic vibration but the noise of an accelerometer, since sensitivity of the accelerometer was reduced to keep measurable dynamic range in this measurement.

13.2.3. Heat Conductor

Fig. 7. Heat conductor cable with large thermal conductivity and a small spring constant.

For the heat conductor between the cryocooler and the cryostat, a large thermal conductivity and a small spring constant are required. We have already succeeded to develop such a heat conductor. Figure 7 shows a photograph of the heat conductor. This heat conductor is a stranded cable consisting of 735 thin aluminum wires with $\phi 0.15$ mm in diameter and 99.999 % in purity. Since the thermal conductivities of the metals strongly depend on their purity at cryogenic temperature, The thermal conductivity of this cable reached to be 2×10^4 W/m/K at 10 K. Since the spring constant of the heat link is inversely proportional to the number of wires under the condition of a constant heat flow, it is effective to use a lot of thin wires while keeping the total cross section and the purity to reduce the spring constant of the heat links. We confirmed that the spring constant of this cable became one order of magnitude smaller than a single cable with the same cross section and the same purity. This cable was also used as heat links between the cold stage of the cryocooler and the vibration reduction stage in the cryocooler system.

13.3. Toward the LCGT

By developing the cryocooler system of the CLIO, fundamental technology of the cryocooler system for the LCGT has been established. The vibration levels of the CLIO cryocoolers have already achieved the LCGT specification. An issue for the LCGT cryocoolers is that larger cooling powers than that of the CLIO are required. For a 4 K cryocooler, a PT cryocooler with a cooling power of 1 W at 4 K stage and 50 W at 50 K stage has been developed. This 1 W PT cryocooler will be introduced to the LCGT cryocooler system, and its vibrations will be reduced by the same vibration-reduction system as the CLIO cryocooler system. By introducing two sets of 4 K

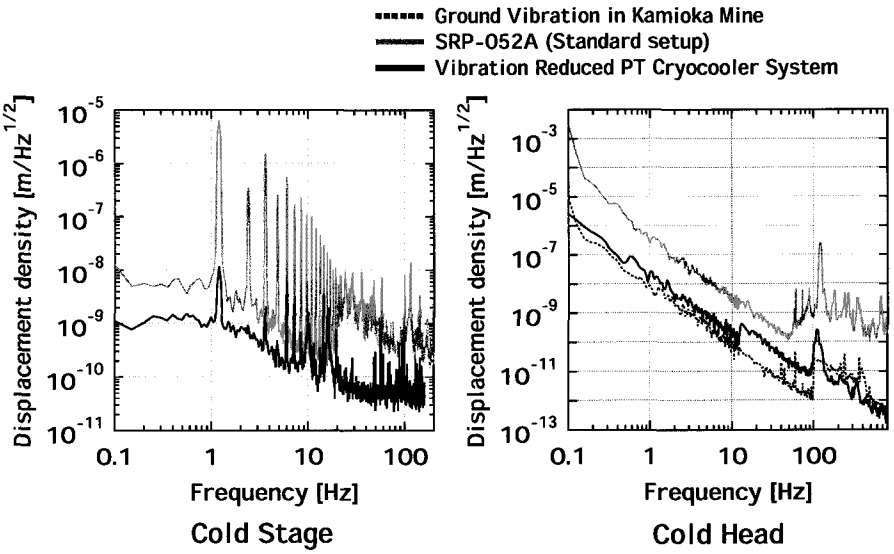

Fig. 5. Vibration-spectra of the cryocooler system. The black lines show the vibration level of our cryocooler system. The gray lines show that of based PT cryocooler (SRP-052A) and a dashed line in the graph of the cold-head shows the seismic vibration level in Kamioka mine.

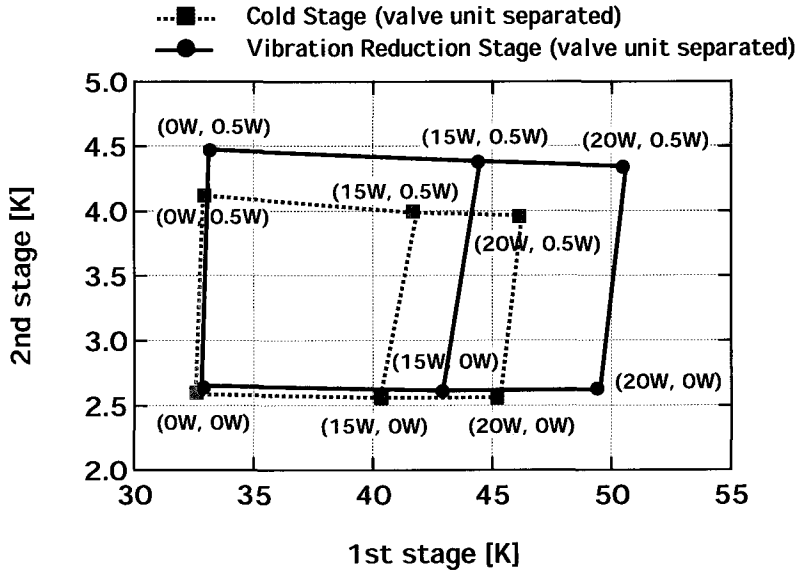

Fig. 6. Heat-load map of our cryocooler system. The black closed circles show the measured cooling powers of our system, and the gray closed squires show those of the basic PT cryocooler (cold stage). The vertical axis shows the temperature of the 2nd (4 K) stages and the horizontal axis shows the temperature of the 1st (40 K) stages. The first values in parentheses show the given heat powers to the 1st stages and the second values in parentheses show the given heat powers to the 2nd stages.

cryocooler systems, the specifications of the 2 W cooling power for the 8 K area and of 100 W cooling power for the 100 K area will be achieved. The specification of the 100 W cooling power for the 100 K beam duct will be also achievable by using two sets of 100 K PT cryocooler systems developed for the CLIO. Therefore, since eight cryostats and sixteen beam ducts will be used in the LCGT, in total sixteen 4 K cryocooler systems and thirty-two 100 K cryocooler systems will be introduced.

As mentioned above, we have sufficient technology to achieve the requirement of the LCGT cooling system.

Bibliography

[1] T. Uchiyama et al., Phys. Lett. A **242** (1998) 211.

[2] T. Tomaru et al., Phys. Lett. A **283** (2001) 80.

[3] K. Kasahara et al., J. Cryo. Soc. Japan **39** (2004) 25.

[4] Y. Ikeya et al., Cryocoolers **12**, Proc. of the 12th Int. Cryocooler Conf., (2003) 403.

[5] Xu M. Y. et al., Cryocoolers **12**, Proc. of the 12th Int. Cryocooler Conf., (2003) 301.

[6] T. Tomaru et al., Cryogenics **44**, (2004) 309

[7] T. Tomaru et al., Cryocoolers **13**, Proc. of the 13th Int. Cryocooler Conf., (2005) 695.

[8] R. Li et al., Cryocoolers **13**, Proc. of the 13th Int. Cryocooler Conf., (2005) 703.

[9] C. Lienerth et al., Proc. of ICEC **18**, (2000) 555.

14. Suspension of Cryogenic Mirrors – Application of Sapphire Bonding for Constructing Suspension Structure –

[Author: SUZUKI, Toshikazu]

KEK, High Energy Accelerator Research Organization, Tsukuba, Ibaraki 305-0801

In this report, the target of consideration is the cryogenic mirror and its suspension, which are suspended from SPI. The current design of LCGT requires a heat load of 2 W to the cryogenic mirror. Four sapphire rods with ϕ1.8 mm $\times$ 500 mm are used as heat paths for cooling. The upper end of these rods are connected to the SPI, which works as an anchoring point of low temperature as well as low vibration. One of the issues is to make a structure for suspension using ϕ1.8 mm rods, which are not elastically deformable along the cylindrical mirror. In the following, techniques of sapphire bonding for constructing the mirror suspension are described.

Items	Parameters
Mirror size	ϕ250 mm $\times$150 mm
Mirror mass	M=29.5 kg
Crystal direction	c-axis$\|\|$Cylinder axis
Operating temperature	T=20 K
Pendulum length	400 mm
Rod (fibre) diameter	ϕ1.8 mm
Number of rods	4
Crystal direction	c-axis$\|\|$Rod axis
Heat flow on the rod	$\dot{q}$ $\approx$500 mW/rod
Anchoring point	SPI at T=10 K

Table 1. Design parameters of the main mirror and the suspension rods.

14.1. Introduction

Suspension of the cryogenic mirror must work as not only a heat path of conduction cooling, but also a vibration isolator against external vibration sources. A suspension has to be made of a material with large thermal conductivity at cryogenic temperatures in order to achieve efficient heat transfer. Also, a pendulum system that consists of a mirror and the suspension is required to have a small loss of mechanical vibration for suppressing thermal noise. From this point of view, fundamental technologies of the cryogenic mirror and suspension have been developed.[1] [2] [3] Mono-crystalline α-alumina (=Sapphire) has been selected as a substrate for the mirror and material of supporting fibers. Figure 1 shows the basic configuration of the cryogenic mirror and suspension. A pair of sapphire fibers that are deformed along half of the cylindrical circumference support the weight of the mirror, and make a pendulum with high quality factor. Any heat caused by a finite absorption of intense laser light is transferred to sapphire fibers through elastic contacts between the mirror and the fibers, and is carried to a cold reservoir by the conduction of sapphire fibers.

This scheme of a cryogenic mirror and suspension is now realized for the Cryogenic Laser Interferometer Observatory (CLIO), which is a prototype for proving the system of a cryogenic mirror. [4] It is not simply applicable, however, in the case of LCGT. Figure 2 shows the minimum bending radius of sapphire fiber by elastic deformation. In the current design of LCGT, sapphire fibers with a diameter of 1.8 mm support a sapphire mirror with a radius of 125 mm. Table 1 lists designed parameters of the main mirror and the suspension rods (fibers). The diameter of the sapphire fibers is designed by a heat-generating rate inside the mirror while taking size effect of thermal conductivity of fibers into consideration.[5] According to the relation in Fig. 2, the minimum bending radius of sapphire fiber with a diameter of 1.8 mm is estimated to be R_{min} $\simeq$1400 mm, which is larger than the mirror radius.

By introducing a technique of sapphire bonding, we can avoid the R_{min} problem. In the following sections, the prospects of a constructing mirror-suspension system of LCGT are described. Two bonding techniques, which are hydroxide-catalysis bonding and direct bonding, are mainly discussed.

14.2. Sapphire-sapphire bonding

14.2.1. Hydroxide-catalysis bonding

A technique of hydroxide-catalysis bonding (HCB) was developed to obtain tight bonding between fused silica at room temperature.[7] After fine polishing ($\sim \lambda/10$) and cleaning contaminants, a small amount of an aqueous solution of potassium hydroxide appropriate to the surface area to be bonded is introduced between the fused silica surfaces and the surfaces brought together. The chemical bonding process is initiated through hydroxide-catalysed surface hydration and dehydration at room temperature. Readjustments of the pieces being joined are possible within approximately 30-40 minutes of the start of the joining process. The maximum strength of bonding is reached after several weeks. The same process of bonding is applicable to sapphire surfaces, although the tensile strength is lower than that of fused silica.[8]

A surface to be bonded does not depend on the direction of the crystal surface, because HCB is basically chemical gluing, and the process of bonding can be carried out at room temperature. This makes it possible to assemble the mirror suspension independent of the mir-

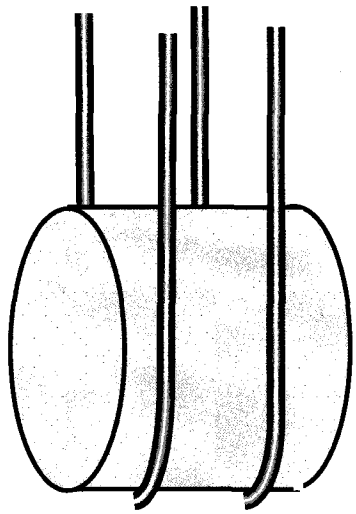

Fig. 1. Basic structure of the cryogenic mirror. Two U-shape fibers support a cylindrical mirror by elastic deformation and make a pendulum. Both the mirror and fibers are made of mono-crystalline α-alumina (Sapphire). The weight of the mirror deforms the supporting fibers and makes elastic contact. The upper ends of the supporting fibers are connected to a cold reservoir.

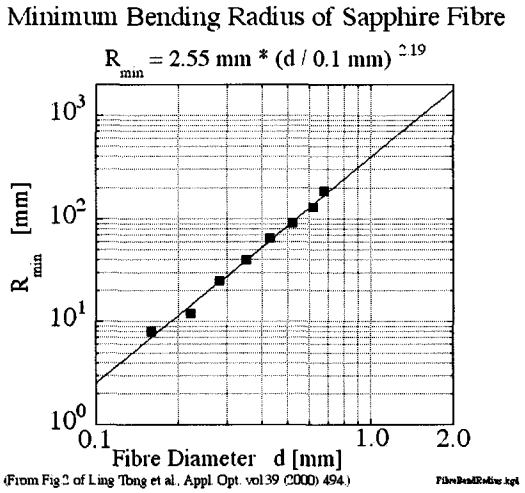

Fig. 2. Minimum bending radius, R_{min}, of the sapphire fiber at 300K. Data were taken from the Fig.2 of Ref. [6] and then re-plotted.

ror fabrication process, although HCB method remains a small amount of impurities on the bonded boundary.

14.2.2. Direct bonding

Direct bonding is a method for bonding two pieces of bulk without any bonding agent. One of the actual applications of sapphire direct bonding is making cells for treating a hydrogen fluoride solution.[9] The surfaces of the pieces of sapphire to be bonded should be of optical flatness and free from any contamination. A heat treatment under appropriate contact pressure makes the surfaces to be bonded together. This method of bonding does not always guarantee a perfect optical transparency of the bonded boundary, at present.

A similar bonding technique for various laser crystals has been developed, although details of the process have not been published.[10] These method do not leave any impurities on the bonded boundary, in principle.

One of the important points of direct bonding is that the thermal expansion of the surfaces to be bonded should be matched because of an anisotropic thermal expansion of sapphire. Figure 3 shows the thermal linear expansion of a sapphire crystal.[11]

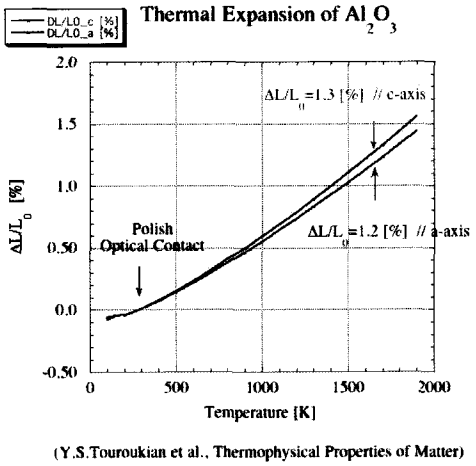

Fig. 3. Thermal linear expansion of a sapphire crystal. Recommended values in the reference of [11] are plotted. L_0 denotes the length of a specimen at T=293 K and ΔL denotes the difference of the length from L_0 at T K. At around a temperature of typical heat treatment, a difference of $\Delta L/L_0$ reaches to 0.1% between the direction of c-axis and a-axis.

Therefore, one should pay attention to adjust the direction of c-axis in each surface to be bonded when two surfaces are parallel to c-axis of each crystal. For example, two pieces of crystal could be bonded in the case of 19 degrees of difference of the c-axis, but bonding failed in the case of 35 degrees of difference. However, though bonding could occur, there remained a little slip of the bonded boundary in the case of 19 degrees of difference of the c-axis. A slip of bonded boundary affects the precision of the geometries of structure when we apply sapphire bonding for constructing the suspension of a mirror.

It has been empirically known that bonding does not depend on three-fold rotation symmetry of a plane being perpendicular to the c-axis.

In general, it is possible that two crystals can be bonded at the plane if the Bravais lattices of each crystal are related to the translation or to reflection of the plane of bonding. The former case is equivalent to a single crystal, and the latter corresponds to a twin crystal.

Figure 4 shows an example of connecting a rod to the mirror by direct bonding.

The c-axis of the mirror is parallel to the cylindrical

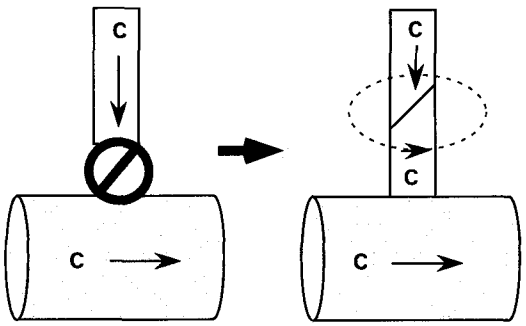

Fig. 4. Example of connecting a rod to the mirror by direct bonding. Left: The c-axes of the mirror and the rod are perpendicular to each other. The lower end of the rod can not be bonded to the side of the mirror because of anisotropic thermal expansion on the surfaces to be bonded. Right: By using planes with inclination of 45 degrees, directions of the rod and the mirror can be matched to bond. This picture sketches that only a single rod connects to the mirror for simplicity reason.

axis of the mirror to avoid any birefringence effect. The c-axis of the mirror and the rod are perpendicular to each other. We need some matching section to connect the mirror and the suspension rod by direct bonding. As shown in the right of Fig.4, it can be realized by a plane with an inclination of 45 degrees to each c-axis of two pieces of crystals.

Direct bonding is expected not only to realize a strong bonding as a bulk crystal, but also to be possible to minimize a thermal resistance on the bonded boundary. On the other hand, there may exist some complexities in the assembling and maintenance work.

14.2.3. Other methods of bonding

14.2.3.1. **Double heat treatment with chemical surface activation** The chemical treatment process make a hydrophilic layer on the bonding surface. A double heat treatment under pressure makes a tight bonding between Ti doped sapphire crystals. This method may be applicable, but the process is complicated.[12]

14.2.3.2. **Surface-activated bonding** Press contact make bonding after cleaning the surfaces by Ar-ion impact in a very high vacuum at room temperature. Successful sapphire-aluminum bonding was reported, but sapphire-sapphire bonding shows some difficulties.[13]

14.2.3.3. **Sapphire-metal bonding** The methods of brazing and soldering have been studied in between alumina ceramics and metals; however, we have not studied those methods.

14.3. Thermal conductance of bonded boundaries

We measured the thermal conductivity of samples at cryogenic temperatures in comparison with methods of direct bonding and hydroxide-catalysis bonding. The parameters of the samples are listed in Table 2. Upon mea-

Bonding	Size (mm)	Manufacturer and Grade
AFB	4×4×55	CSI, HEMEX
HCB	ϕ10×60	NGK, ...

Table 2. Description of Samples. AFB: Adhesion Free Bonding (Onyx Inc.[10]), HCB : Hydroxide-Catalysis Bonding, CSI : Crystal Systems Inc., NGK: NGK Insulators, LTD. AFB is a kind of direct bonding. For both samples, two pieces of raw materials with length of 30 mm were bonded together by each bonding method. The reason why the AFB sample has 55 mm length is a 45 degrees inclination of bonded boundary.

suring the thermal conductivity, the base temperature and the heat current were controlled by two heaters, and then temperature gradient was monitored in both the bulk and the bonded parts of the sample.[14] The thermal conductance of the bonded boundary is defined as $Y_{th} \equiv \dot{q}/\Delta T$, where ΔT denotes a difference of temperature across the boundary and $\dot{q}$ denotes a heat current flowing through the boundary. From the difference of the thermal conductivities of the bulk and the bonded part, the thermal conductance of the boundary was calculated. In this calculation, the temperature dependence of the thermal conductivity was ignored. The evaluated error from this assumption was less than 10 %. Figure 5 shows thermal conductance per area of bonded boundary.

In the Fig. 5 , Y_{th}/A looked almost constant for each bonding method around T=20 K, which is the operating temperature of the cryogenic mirror. We take Y_{th}/A=4 W/K/mm^2 for AFB and Y_{th}/A=0.3 W/K/mm^2 for HCB around T=20 K from the Figure 5.

14.4. Strength of bonding

The shear strength of the bonded boundary was measured. Samples were straight cylinders with a ϕ10 mm × 60 mm. Two of the cylinders with a ϕ10 mm × 30 mm were bonded together to make a sample. All of the bonding surfaces were parallel to a c-axis of each crystal. The aging period was about 1 month for a direct bonded sample, and about 3 years for a hydroxide-catalysis bonded sample in the atmosphere at room temperature. No thermal cycle between 300 K and cryogenic temperatures was experienced for both samples. One end of the sample was fixed, and a torque was put on the other end. The maximum torque of breaking the sample was recorded. Data were taken only at room temperature at present. Breaking occurred along the bonded boundary for the HCB sample. In the case of the direct bonded sample, about

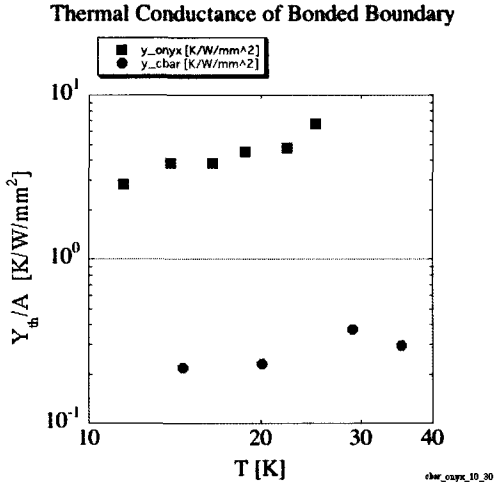

Fig. 5. Thermal conductance per area of bonded boundary in 10 K $\leq$ T $\leq$ 30 K . Solid blue squares denote Y_{th}/A of AFB and solid red circles denote Y_{th}/A of HCB where A denotes the area of bonded boundary. Data around the operating temperature of the cryogenic mirror and the suspension are plotted.

1/3 of the bonding area broke along the bonded boundary, and another 2/3 of area cracked into the substrate with about 50 degrees of inclination to the c-axis. [15]

Using the shear strength, σ_{shear}, of each method of bonding, for required area that can support the weight of the mirror when four rods are bonded on the side surface of the mirror. In this evaluation, σ_{shear} is assumed to be independent of the temperature.

Also, a difference of temperature across the bonded boundary was evaluated for each bonding method. Table 3 shows the results. In Table 3, the bonding area takes twice the minimum required area for one rod as a margin. The values of $2A_{\frac{Mg}{4}}$ in Table 3 are practically realizable when the ϕ1.8 mm rod is used. For example, consider a rectangular bonding surface with 1.8 mm width that is made by machining and polishing half of the thickness along the rod. The length of the rectangular surface needs 2.8 mm for direct bonding and 12mm for HCB in each rod, respectively.

Each suspension rod transfers a heat current of $\dot{q}$=500 mW from the mirror to the SPI. The designed temperature of the mirror is T=20 K and that of the SPI is 10 K.[2] The estimated temperature step, ΔT_B, due to the bonded boundary is much smaller than the total difference of the temperature between the mirror and the SPI for both cases. Thus boding does not affect the designed efficiency of heat transfer of the suspension.

14.5. Connection of suspension rods to the SPI

The connection of suspension rods to the SPI is an important part of the suspension system; however, the application of bonding is not planed for this part, at present. A method where two sapphire blocks cramp tightly to a sapphire fiber has been developed.[3] By this method, the mechanical quality factor of cramping can satisfy the requirement of the quality factor of the pendulum. Once mechanical cramping is established, a heat path can be added without interfering with the quality factor of the pendulum on the SPI.

*2 Refer to the Fig.(1) of the chapter "Cooling System".

14.6. Summary and Discussion

From the experimental data, a bonding area of 5.06 mm^2 is required by the method of direct bonding, and a bonding area of 22 mm^2 is required by hydroxide-catalysis bonding for supporting a quarter weight of the mirror on each suspension rod. Those values include a margin factor of 2. The estimated thermal conductance of those areas does not affect the designed thermal transfer along the suspension rods. The method of cramping suspension rods to the SPI has already been developed.

Based on the present results, it is possible to construct for a structure of the suspension system of the cryogenic mirror by applying the method of sapphire bonding. The quality factor of the suspension system will be confirmed after constructing a prototype. As mentioned before, there is an issue of how to make a consistency with a process of direct bonding and the fabrication of a high-quality mirror. If it is difficult for the suspension rod to connect to the mirror by direct bonding, we could select another way of application. It is possible to make a long U-shape suspension from straight rods and a rod with a half-circle-shape by a bonding technique. A technique of plastic deformation of sapphire already exists.[6]

Bibliography

[1] T. Uchiyama *et al.*, Phys. Lett. **A242**, 211 (1998).

[2] T. Uchiyama *et al.*, Phys. Lett. **A261**, 5 (1998).

[3] T. Uchiyama *et al.*, Phys. Lett. **A273**, 310 (2000).

[4] S. Miyoki *et al.*, Class Quant. Grav. **21**, S1173 (2004).

[5] T. Tomaru *et al.*, Phys. Lett. **A301**, 215 (2002).

[6] L. T. Tong *et al.*, Appl. Opt. **39**, 494 (2000).

[7] S. Rowan *et al.*, Phys. Lett. **A246**, 471 (1998).

[8] H.Armandula *et al.*, LIGO-G010267-R (2001).

[9] Japan Cell Co., Ltd. http://www.jpcell.co.jp/

[10] Onyx Optics Inc. http://www.onyxoptics.com/

[11] Y. S. Touloukian *et al.*, *Thermophysical properties of matter* **13**, New York : IFI/Plenum (1977).

[12] A.Sugiyama *et al.*, Appl. Opt. **37**, 2407 (1998).

[13] T.Suga, Mater. Jpn. **35**,496 (1998), in Japanese.

[14] T.Suzuki *et al.*, to be published in Int. J. Mod. Phys. A.

	Direct Bonding	Hydroxide-catalysis Bonding
Shear strength σ_{shear}	28.4 MPa	6.53 MPa
Bonding area $2A_{\frac{Mg}{4}}$	5.06 mm^2	22.0 mm^2
Thermal conductance on $2A_{\frac{Mg}{4}}$	20 W/K	6.6 W/K
ΔT_B for $\dot{q}$=500 mW	25 mK	76 mK

Table 3. Shear strength of bonding, the required bonding area and the estimated temperature step across the bonded boundary. $A_{\frac{Mg}{4}}$ denotes the minimum required area for supporting the mirror with four rods. Here, we take the bonding area as twice $A_{\frac{Mg}{4}}$ as a margin. The shear strength σ_{shear} is assumed to be independent of the temperature. ΔT_B denotes the estimated temperature step across the bonded boundary.

[15] T.Suzuki , presentation in *6th Edoardo Amaldi Conference on Gravitational Waves*, http://amaldi6.nao.ac.jp/.

15. Cryogenic Mirror

[Author: KURODA, Kazuaki]
ICRR, Univ. of Tokyo, Kashiwa, Chiba 277-8582

15.1. Requirement of LCGT Mirror

For each interferometer set, the four main mirrors and the four auxiliary mirrors that form a full SPI are made of sapphire, and other mirrors are made of synthetic silica. Although these eight pieces of mirror are set at cryogenic temperature, the basic technique of mirror production is common to the established one by TAMA and/or other gravitational wave projects. The main differences are as follows:

- Sapphire is not glass, but crystal.
- The diameter of the main mirrors is enlarged from 10 cm to 25 cm.

Sapphire crystal has, optically, a slight birefringence, which results in a constraint of making its optical axis to align with the laser beam axis, and requires some special polishing technique. The problem arising from the scale-up in diameter is common to other projects.

The parameters of the main mirror are listed in Table 15.1. The requirements of the main mirrors are summarized in the table in Appendix.

Item	Parameter
Density	4×10^3 kg/m^3
Radius	12.5 cm
Width	15.0 cm
Mass	29.5 kg
Temperature	20 K
Youngfs Modulus	4×10^{11} Pa
Poisson Ratio	0.29
Mechanical Quality Factor	10^8
Thermal expansion ratio	5.6×10^{-9} at 20 K
W/[m*K]	5.0×10^{-6} at 300 K
Specific heat J/[kg*K]	7.9×10^2 at 300 K
Thermal conductivity	40 at 300 K
W/[m*K]	2×10^4 at 20 K
Thickness of coating	5×10^{-6} m
Loss angle of coating	4×10^{-4}

Table 1. Design Parameters of the Sapphire Main Mirror.

15.2. Achieved Technique

During the course of mirror development for TAMA, we exchanged technical information with the LIGO, VIRGO, and GEO groups regarding to the substrate material, polishing, and the coating technique. The first good quality mirror was produced by Japan Aviation Electronics Industry Ltd (JAE) using an Ion Beam Sputtering (IBS) machine utilizing a Kaufmann-type ion gun. It was measured by our collaborators, who published the result of an ultra-high quality cavity with 1.5 ppm loss at 1064 nm [1]. The mirror surface micro-roughness was 0.069 nm rms and the surface flatness was much better than $\lambda/10$ at 633 nm. The high-reflectance IBS coating was a 29-layer quarter-wave Ta_2O_5/SiO_2, whose design was 4 N reflectance. The beam size of this experiment was small (0.41 mm) compared with the wider beam size that was used in a practical interferometer. R&D was consistently continued for pursuing a higher quality mirror. At the time of making the TAMA mirror, the dependence of the beam size was studied using a 20 m prototype interferometer [2]. Figure 1 shows the mapped loss distribution taken at the table-top measurement. The loss averaged on the whole surface was 40 ppm, and the measured loss was 30 ppm for a 4.4 mm beam diameter. High loss peaks came from point-like defects. The average, except for these high peaks, was 27 ppm. The origin of these point-like defects was found, which was fed back to the sputtering process. The TAMA mirror was successfully produced according to the above effort.

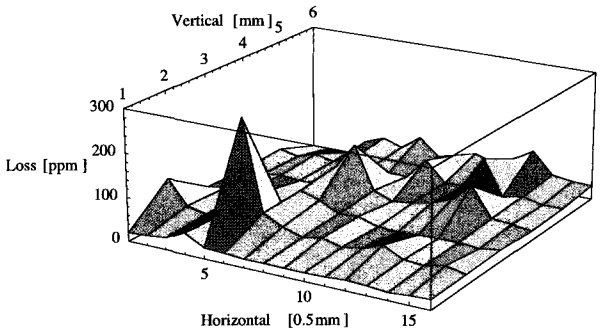

Fig. 1. Loss distribution of a high-reflective coating with low loss. The loss averaged on the whole surface was 40 ppm and the measured loss was 30 ppm for a 4.4 mm beam diameter. High-loss peaks came from point-like defects, the origin of which was surveyed and improved when the TAMA mirrors were coated.

With regard to polishing the mirrors, the performance was evaluated by using a wave-front tracing simulation in collaboration between the TAMA and LIGO [3]. The specification for imperfections of mirrors was several tens of nano-meters at low spatial frequencies and sub-angstrom at high spatial frequencies. The substrate of

the TAMA mirrors was Suprasil P10, produced by Shinetsu Quartz Products, Co. Ltd. The polishing of the four main mirrors and the beam splitter was done by JAE and the recycling mirror was polished by General Optics Inc. The surface quality of the TAMA mirrors was measured by use of Zygo GPI-XP/HR, a Fizeau interferometer adopting 633 nm wavelength light. Figure 2 shows the imperfection mapping sample images, where the images of curved mirrors (end mirror and recycling mirror) were obtained by subtracting their global curvatures. From these imperfection images power spectral densities (PSD) were calculated by FFT. Using these PSD, the wave-front tracing was applied and its result was compared with experimental result. Table 15.2. summarizes a comparison of these results. From them we are confident that the mirror polishing does not limit the objective sensitivity of TAMA.

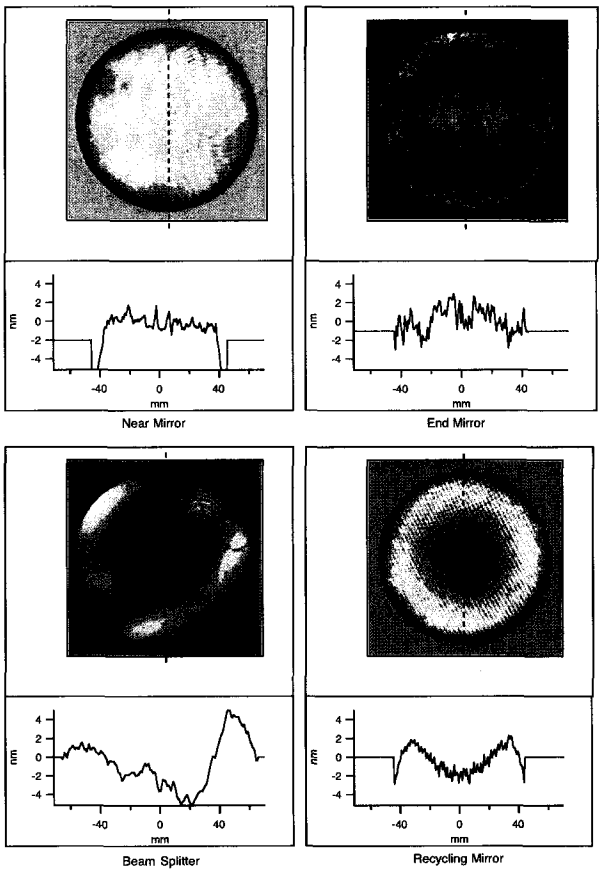

Fig. 2. Imperfection mapping sample images of the TAMA mirrors, where the images of curved mirrors (end mirror and recycling mirror) were obtained by subtracting their global curvatures.

15.3. Basic Technique on Sapphire Mirror

A characteristic of sapphire material at cryogenic temperature is that the thermal expansion rate tends to zero with decreasing temperature, and the thermal conductivity becomes fairly large with its maximum at around 20 K (in Table 15.1.). As has already reported, the cryogenic mirror is free from any thermal lens effect [4], and is also unaffected by thermal noise [5]. Therefore, Ta_2O_5/SiO_2 coating can be safely used. We have already tested the coating on a sapphire substrate, and have confirmed that its quality is almost identical to the coating on silica substrate.

The CLIO mirror was polished and coated successfully, as shown in both Table 3 and Table 4. The size of the mirror is the same as that of TAMA. CLIO construction will be finished in 2006 [6].

Substrate	sapphire
Shape	$\phi 100 \times 60$
Curvature	∞
Accuracy	Less than $\lambda/10$ PV
Guaranteed Scale	$\Phi 80$
Micro-Roughness	Less than 0.5 nm rms
Appearance	MIL 30/10
Others	Wedged

Table 3. Specification of CLIO near mirror. Two pieces of the near mirror have been polished and coated, satisfying this specification.

Substrate	sapphire
Shape	$\phi 100 \times 60$
Curvature	$R = 150 \pm 10$ m
Accuracy	Less than $\lambda/5$ PV ($\lambda/10$ targeted)
Guaranteed Scale	$\Phi 80$
Micro-Roughness	Less than 0.5 nm rms
Appearance	MIL 30/10
Others	Wedged

Table 4. Specification of CLIO end mirror. Two pieces of the end mirror have been polished and coated satisfying this specification.

15.4. Mirror Substrate

Synthetic sapphire is commercially produced, and a large bowl of sapphire satisfying the mirror size of the advanced LIGO has already been produced by Crystal Systems Inc. According to the necessity of a high quality of sapphire, several measurements are reported, and knowledge is increasing to obtain a higher quality of sapphire for laser interferometers. Referencing the previous result of measuring the birefringence of sapphire, we have developed an automatic measuring device of the birefringence of a sapphire rod sample. The objective of the machine is both inspecting the crystal quality of sapphire substrates that are purchased from companies, and estimating the optical quality of substrates. The measurement principle has already been reported [7]. Suppose that there is some imperfection of the crystal that causes optical-phase retardance between two orthogonal polarizations. The fluctuation of the magnitude of the retardance represents the magnitude of the crystal imperfections. Figure 3 represents an example of mapping

Parameter	Design (Calculated by Design)	Experiment	Simulation
Cavity reflectivity	95.7% (estimated)	96%	91.3%
Finesse in in-line arm	516	491	526
Finesse in perpendicular arm	516	512	528
Contrast	99.0% (Estimation)	98.2%	98.8%
Sensitivity $Hz^{-1/2}$ at 300 Hz	2.0×10^{-21}	1.5×10^{-20}	4.9×10^{-22}

Table 2. The result of wave-front tracing was compared with experimental result.

of the measured optical phase shift caused by the substrate. Preliminary measurements of four sapphire rods found no apparent defect inside, and the magnitudes of the imperfection represented negligibly a small birefringence. This machine can accept a large scale of sapphire rod up to 30 cm in diameter.

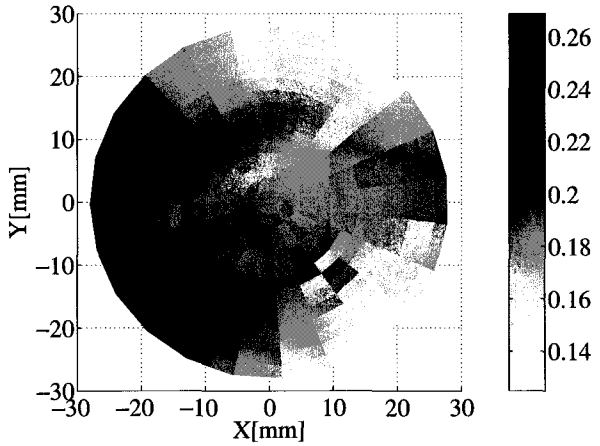

Fig. 3. Measured imperfection in terms of the retardance angle. The fluctuation of the magnitude of the retardance represents the magnitude of the crystal imperfections, which was negligibly small. The unit of numbers is radian.

15.5. R&D for LCGT Mirror

The mechanical quality of sapphire is good enough to satisfy the requirement of LCGT [8]. However, the optical loss has some room to be improved. Sapphire samples produced by Crystal Systems Inc. might satisfy the requirement by applying a heat treatment [9]. This research and development will be conducted in collaboration with the sapphire research group of LIGO.

Bibliography

[1] A. Ueda *et al.*, Optical Review **3**, 369 (1996).

[2] S. Sato *et al.*, Applied Optics **38**, 2880 (1999).

[3] T. Tomaru *et al.*, Applied Optics **41**, 5913 (2002).

[4] T. Tomaru, Doctor Thesis, The University of Tokyo (2001).

[5] K. Yamamoto *et al.*, Class. Quantum. Gravity **21**, S1075 (2003).

[6] M. Ohashi, *et al.*, Class. Quantum Grav. **20**, S599 (2003).

[7] M. Tokunari *et al.*, in *Proceedings of Amaldi6 held in Okinawa 19-23, June* (2005).

[8] T. Uchiyama *et al.*, Phys. Lett. A **242**, 211 (1998).

[9] http://ligo.caltech.edu/ gari/LIGOII/Downselect/index.shtml

16. Suspension Point Interferometer (SPI)

[Author: MIYOKI, Shinji]
ICRR, Univ. of Tokyo, Kashiwa, Chiba 277-8582

16.1. Introduction

The main purpose for considering the Suspension Point Interferometer (SPI) is that SPI is powerful to prevent seismic noise vibration toward the SPI mirrors from shaking them, especially through the heat-link wires, which are considered to be an insurance against possible malfunction of the anti-vibration system in the mirror cooling system in LCGT. The original idea of SPI was proposed by R. Drever[1]. Figure 1 shows schematic view of SPI. A pair of mirrors that form the main Fabry-Perot cavity are suspended from another pair of mirrors, which also from another Fabry-Perot cavity. If the upper Fabry-Perot cavity is controlled to be resonant using a well-stabilized laser wave length, any length fluctuation between the upper masses can be stabilized, and the resulting length fluctuation of the main mirrors is also reduced. In addition to this, because SPI has comparable a low noise length sensitivity with the main interferometer's sensitivity, the SPI control noise dose not spoil the sensitivity of the main interferometer, while the commercial vibration sensors, such as an accelerometer and so on, have much worse sensor noise.

In the LCGT mirror cooling system, as referred in the previous section, the upper masses for the main mirrors should have mechanical contact with a heat anchor position in the cryostat with a bundle of pure aluminum wires (so-called a heat link) to extract heat that is generated in the sapphire mirror. This mechanical contact becomes another seismic noise transfer path to the main mirrors, in addition to the SAS seismic noise isolation path, which is also referred to in the previous section. From the point of view of seismic noise isolation, a large number of pendulum stages below the heat anchored upper mass is desirable, while the least pendulum stage numbers (minimum is two stages including the main sapphire mirror and the heat-linked upper mass) is desirable from the point of view of minimizing the heat capacity in the cryostat and simplifying the mechanics in the cryogenic area. The necessity of SPI strongly depends on the mechanical pendulum design in the cryogenic area. At present, the compromising number of pendulum stages in the cryogenic area is three: a heat-anchored pre-isolator, a SPI mirror and the main sapphire mirror, as shown in the Figure 1 in the "Seismic Isolator" section. In this configuration, the seismic noise through the heat link can be reduced below the LCGT targeted sensitivity above10Hz with several safety factors. Because the seismic noise isolation tends to be less in practice than we expected, it is important to prepare a counter-plan to increase the margin. This is one of the reasons why SPI is taken into

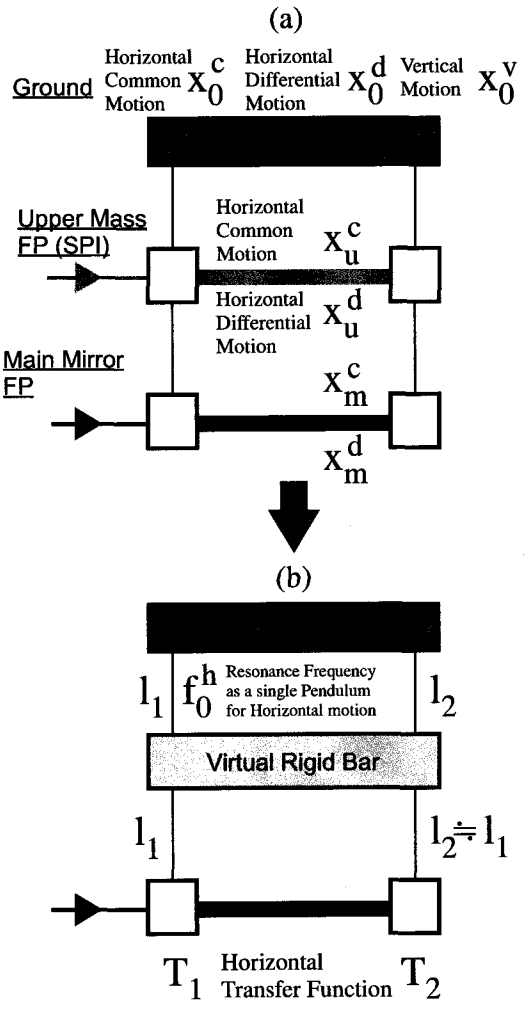

Fig. 1. Suspension point interferometer for a Fabry-Perot cavity.

account for the LCGT.

In addition to this, SPI can be another gravitational wave (GW) antenna that has comparable sensitivity with the main gravitational wave antenna for the different frequency range. Although this is still an option for LCGT, it is exciting to point out this "parallel GW interferometers".

16.2. Principle of SPI as a Seismic Noise Isolator

Firstly, consider a Fabry-Perot cavity that is constructed with a pair of double-pendulum mirrors, as shown in Figure 1. We define the transfer function between the suspension point and the each main mirror as T_1 and T_2, respectively. If the upper-mass cavity length is controlled to resonate the cavity using a well-stabilized laser wave-length, the upper masses can be considered to be one solid-body mass. In this case, the ratio between $T_1 - T_2$ and T_1 (or T_2) (we define this as Common Mode Rejection Ratio (CMRR)) becomes as shown in Figure 2.

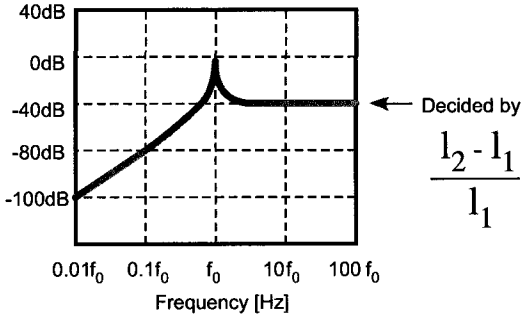

Fig. 2. Common mode rejection ratio of SPI.

CMRR above the pendulum resonance frequency becomes a constant: the ratio between the pendulum wire lengths (l_1 or l_2) below the upper masses and their difference ($dl = l_1 - l_2$). For the frequency range below the resonance frequency (f_0^h), CMRR is proportional to f^2. This means that the common-mode fluctuation between the upper-mass distance can transfer the differential length fluctuation between the main mirrors (x_m^d) by CMRR $\times\, x_u^c \times (f_0^h/f)^2 \simeq$ CMRR $\times\, x_0^d \times (f_0^h/f)^4$, where $x_u^d \sim x_u^c \simeq x_0^{d\sqrt{\text{or}}\sqrt{c}} \times (f_0^h/f)^2$. Actually, the differential motion of the upper masses is not fixed, but is just reduced to be $x_u^d/(1+G)$, where G is the control loop gain. Thus, the resulting differential motion between the main mirrors is $x_0^d/(1+G) \times (f_0^h/f)^4$. Consequently, the total amount of the main mirror differential motion (x_m^d) becomes the root sum of squares of these two contributions. In addition to this, we should consider the vertical-horizontal coupling effect, which cannot be reduced by SPI. The coupling amount is $k \times x_0^v \times (f_0^v/f)^4$, where k is a vertical-horizontal coupling constant, this value can easily spoil the SPI effect unless the vertical vibration is enough reduced.

Secondly, let's consider the Michelson interferometer (MI), which is constructed with two double pendulum

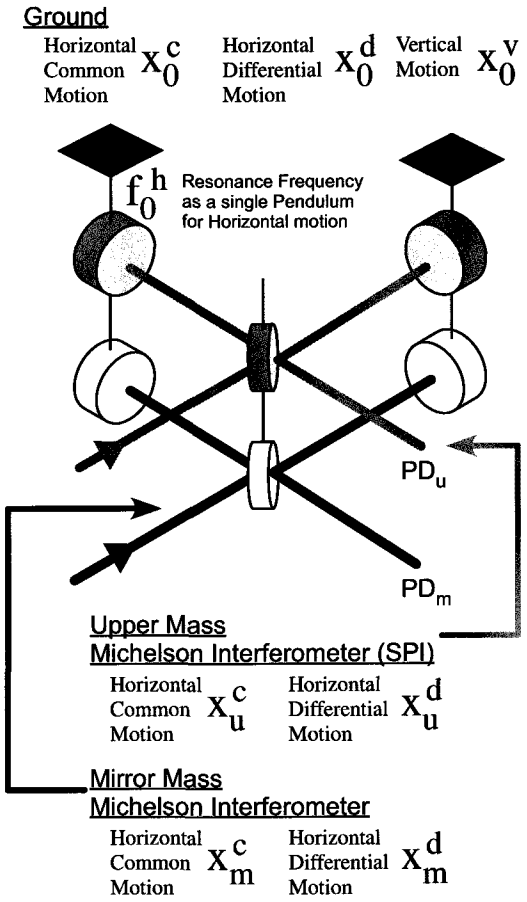

Fig. 3. Suspension point interferometer for a Michelson interferometer.

mirrors and one double pendulum beam splitter, as shown in Figure 3.

The story is almost the same as that for the Fabry-Perot cavity SPI. The differential length of the upper masses MI (x_u^d) is supposed to be controlled to keep a constant fringe at the anti-symmetric port (PDu). In this case, the differential displacement (x_u^d) at the upper masses MI is reduced to be $x_u^d/(1+G)$, where G is the loop gain for the upper masses MI fringe control. On the other hand, the common-length fluctuation of the upper masses MI (x_u^c) can transfer the differential motion of the main mirrors by a ratio of CMRR, according to the previous discussion. Totally, the differential motion of the main mirror MI (x_m^d) is the root sum of squares of $(x_u^d/(1+G) \times (f_0^h/f)^2$ and CMRR $\times\, x_u^c \times (f_0^h/f)^2$, where $x_u^d \simeq x_u^c \simeq x_0^{c\sqrt{\text{or}}\sqrt{d}} \times (f_0^h/f)^2$. Experimentally, G is bigger than 100 below 10 Hz because the control unity gain frequency can be set over 1kHz, while CMRR over f_0 is nominally about 1/100. Consequently, x_m^d is dominated by the latter term below 10 Hz, while by the former term above 10 Hz. In any case, we can reduce x_m^d by using SPI. In the same manner, we can consider the case of a locked Fabry-Perot Interferometer.

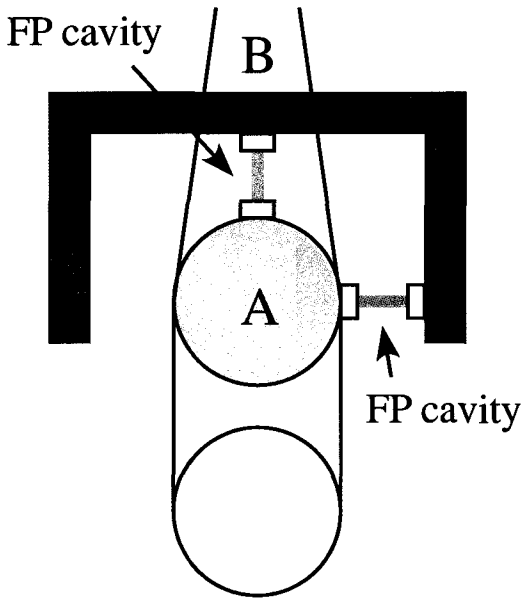

Fig. 4. Local suspension point interferometer for vertical and transverse motion reduction.

16.3. Technical Issues to introduce SPI in practice

As mentioned in the previous section, the vertical vibration should be isolated as much as the horizontal vibration to obtain horizontal vibration reduction due to SPI. One of remedies for this problem is a Local suspension Point Interferometer (LSPI). The concept of the LSPI is shown in Figure 4.

There is a Fabry-Perot cavity between a suspension platform (B) and the upper masse (A). The AC position of B and the DC position of A is controlled so as to keep the cavity resonating. LSPI configuration has been demonstrated [2][3] using electrostatic actuators, but not by the Fabry-Perot. In the same manner, the transverse vibration can also be stabilized as shown in Figure 4. Such a complicated structure and control are now under investigating at room temperature condition.

Another issue is how to keep the independent alignment control of the SPI masses and the main mirrors. Because these mirrors are directly connected with each other, cross coupling of the pitch and yaw motion between these mirrors will take place. One way to minimize the coupling of the pitch and yaw motion is to set the resonance frequency of the pitch and yaw to be as small as possible. To realize such a condition, a cross-suspension wire might be useful for the yaw motion and a single wrapping is useful for the pitch motion, as shown in Figure 5. We should, however, design a practical instrument to realize the proposed method for the sapphire mirror suspension using sapphire fibers under the cryogenic area.

The scattering light coupling between the SPI cavity and the main cavity is also one of issues to be considered.

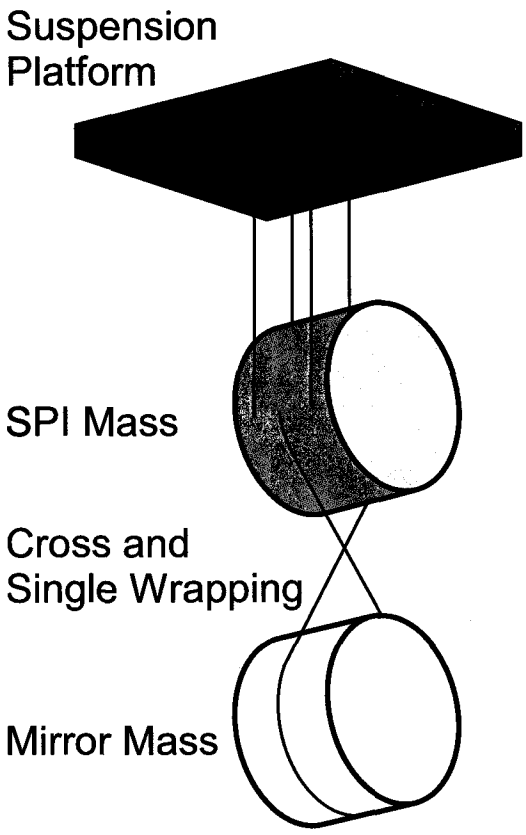

Fig. 5. One idea about how to suspend the main mirror so as to minimize the motion coupling with the upper mass. The main mirror is suspended with an x-shape single wrapping wire.

One is to use the different wave-length of light for the SPI and the main interferometer.

16.4. Toward LCGT

Conceptually, SPI is a promising configuration as the active vibration isolation system, and might become another gravitational wave interferometer that has comparable strain sensitivity with the main GW interferometer for the different observable frequency range. On the other hand, we have to put much emphasis on its R&D to realize the SPI apparatus using sapphire mirrors and sapphire suspension fibers, which are essential for LCGT. Although SPI is not indispensable at present to obtain the LCGT goal sensitivity, SPI is worth challenging to ensure sufficient seismic noise reduction and provide other GW detectors.

Bibliography

[1] R.W.P. Drever and S.J.August, Class.Quantum.Grav. **19** 2005 (2002).

[2] P.R.Saulson, Rev.Sci.Instrum. **55**(8) 1315 (1984).

[3] P.G.Nelson, Rev.Sci.Instrum. **62**(9) 2069 (1991).

17. Seismic Isolator

[Author: TAKAMORI, Akiteru]

Earthquake Research Institute, University of Tokyo, Yayoi, Tokyo 113-0032

17.1. Scope of the Seismic Isolator

The specification and design philosophy of the seismic isolator for LCGT is described in this section. 'Seismic isolator' is the interface between a test mass suspension system and the ground. Only the mechanical seismic attenuation performance of the suspension system is considered, and the other advanced techniques such as the supplemental suspension point interferometer, and the cryogenic issues, are not regarded in this section. Refer to other sections for those specific topics.

17.2. Specifications

17.2.1. Seismic Isolation in the GW Detection Band

A Kamioka mine, the planned LCGT site, is suitable for a GW detector owing to its stable ambience. Particularly, the level of seismic activity is substantially low, 100 to 1,000-times quieter than that of the TAMA300 site below 50 Hz. According to actual measurements in the mine, the spectra of the ground acceleration is very smooth, with no critical structure (peak) in this band. The nominal ground displacement has been modeled as

$$x_s = \frac{10^{-9}}{f^2} \quad [\mathrm{m}/\sqrt{\mathrm{Hz}}] \tag{26}$$

in the frequency domain, where f, x_s are the frequency and the power spectral density of the ground displacement. This model has been determined from observations, and is valid between 100 mHz to several tens of Hz. Below this frequency, the value is considered to be as a constant in other similar models, so we assume $10^{-7}\mathrm{m}/\sqrt{\mathrm{Hz}}$ for lower frequencies.

As the design criterion, above 10 Hz, the most critical GW observation band of LCGT, the sensitivity of the interferometer should be determined by the fundamental limit from the radiation pressure by the photons stored in the main arm cavities and the shot noise. To realize this condition, the effect of seismic disturbances must be sufficiently attenuated below the radiation pressure. This yields the critical design requirements for the performance of the seismic isolators. We define the specifications as:

- Seismic noise becomes 100-times smaller than radiation pressure noise at 10 Hz.
- Seismic noise decreases quicker than the radiation pressure noise at higher frequencies. i.e. the frequency dependency needs to be steeper than $1/f^2$.

To achieve these specifications, we need more than two stages of passive isolators with better than a -150 dB attenuation ratio at 10 Hz, since the ground motion level is about $10^{-11}\mathrm{m}/\sqrt{\mathrm{Hz}}$ at the Kamioka site, while the estimated radiation pressure noise is $3\times10^{-19}\mathrm{m}/\sqrt{\mathrm{Hz}}$ at this frequency.

17.2.2. Seismic Isolation in Low-Frequency Band

The required isolation performance to secure the LCGT target sensitivity is briefly described in the previous section. The isolation below the GW detection band (below 10 Hz) is considered here.

As can be seen in the above model, the power of seismic activity is localized at low frequencies. On the other hand, typical seismic isolation systems (i.e. normal pendulum) have excellent isolation performance at higher frequencies, above 10 Hz. Therefore, the displacement of the suspended optics with respect to inertial coordinates is mainly contributed by the low-frequency components. Even with the microseismic peak around 200 - 300 mHz, excited by coastal activities, the ground motion level in Kamioka mine is in the order of $10^{-6}\mathrm{m}/\sqrt{\mathrm{Hz}}$. It is about 1/10 of the motion observed at the TAMA site. By introducing low-frequency seismic isolators, it is possible to take full advantage of this extremely stable seismic environment, to achieve a high duty cycle of the interferometer. The threshold velocity of the main arm cavity mirrors to lock the LCGT interferometer within 10 seconds is roughly estimated to about 0.5μm/s. In order to suppress the residual velocity of suspended mirrors (integrated above 100 mHz) down to 1μm/s, the required attenuation at 100 mHz is about -20 dB. Also, mechanical resonances should be efficiently damped to avoid large excitation that exceeds the threshold velocity. Specification for low frequency attenuation:

- -20 dB attenuation at 100 mHz.

17.3. Seismic Attenuation System (SAS)

The Seismic Attenuation System (SAS) is a low-frequency seismic isolator that realizes the specifications described in the previous section. It consists of low frequency mechanical filters and local control subsystems.

17.3.1. SAS Mechanics

The low frequency isolation of SAS is achieved by a series of harmonic oscillators, an inverted pendulum (IP) and Geometric Anti-Spring filters (GAS filters) suspended from the IP (figure 1).

IP is a horizontal ultra-low frequency pre-isolator. The IP working principle is illustrated in figure 2. An IP leg is connected to the ground via an elastic joint (flex joint),

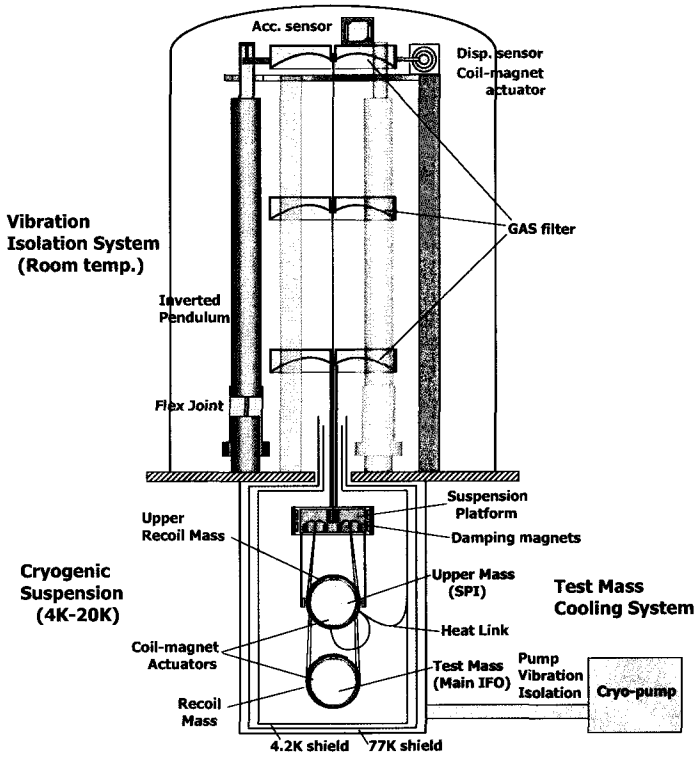

Fig. 1. Schematic view of LCGT SAS. An SAS tower consist of an IP and three MGAS filters, followed by a triple pendulum.

and a payload is suspended from the top of the leg. When the payload displaces horizontally from the equilibrium point, the IP leg rotates about the bending point of the flex joint. An elastic restoring force generated by the joint is partially compensated by the projection of the gravity force, which is proportional to the horizontal displacement, too. As a result of the compensation, the effective spring constant of the system becomes

$$k_{eff} = \frac{k_\theta}{l^2} - \left(\frac{m}{2} + M\right)\frac{g}{l}, \tag{27}$$

where k is the rotational spring constant of the joint, M and m are the mass of the payload and the leg, respectively, l is the length of the leg, and g is the gravitational acceleration. By adjusting the payload mass, the leg length and other parameters, one can obtain an extremely small spring constant i.e. very low-frequency resonance. Although the joint elastic force could be completely compensated by the gravitational anti-spring force under ideal conditions, in real instruments, a too-small restoring force unveils non-linear effect, mainly caused by material friction, which makes the system difficult to deal with. In our R&D so far, 30 mHz has been identified as the practical low-frequency limit. Incidentally, the required -20 dB attenuation at 100 mHz that ensures easy lock acquisition of the interferometer will be realized with this resonant frequency. The attenuation saturation at higher frequencies due to the momentum of inertia of the IP leg can be minimized by re-distributing

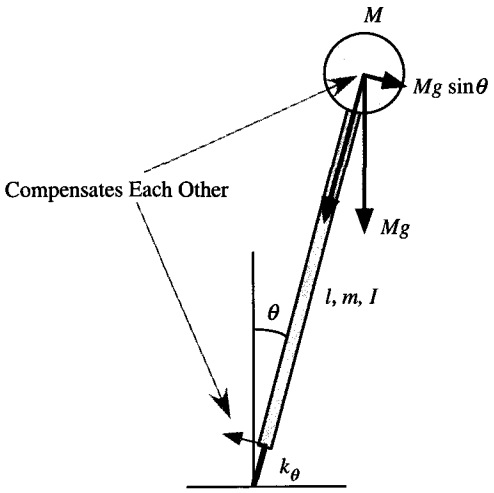

Fig. 2. IP working principle.

the mass along the leg with attached counter weights. In our prototype tests, an IP with 30 - 40 mHz resonance, which works as an ideal harmonic oscillator up to 5 Hz, with the saturation plateau at -75 dB, was achieved. The extreme softness of the IP realizes not only supreme low-frequency isolation, but also highly efficient positioning of the suspended optics.

A series of GAS filters, which isolate the vibration in all six degrees of freedom, is suspended from the IP. The

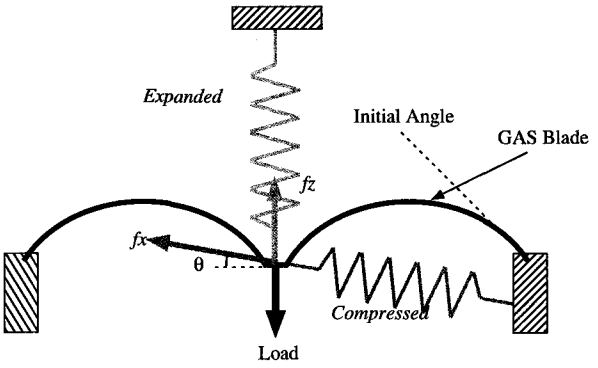

Fig. 3. GAS working principle. A GAS blade is interpreted as a combination of virtual vertical (blue) and horizontal (green) linear springs.

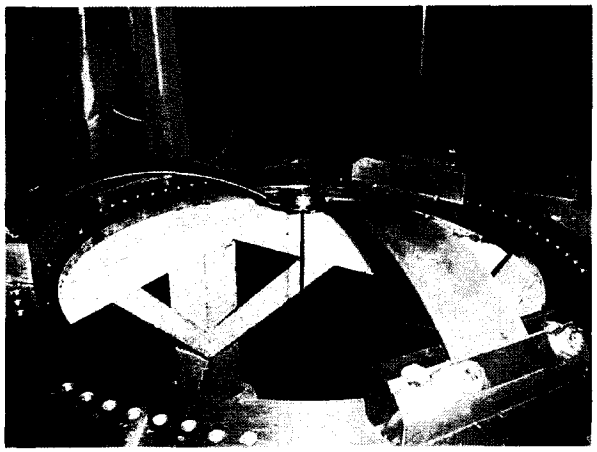

Fig. 4. Prototype GAS. Three monolithic GAS blades hold 50 kg payload. This prototype was tuned down to 200 mHz.

working principle of the GAS is shown in figure 3. GAS is a simple, horizontally compressed cantilever spring to produce vertical and horizontal restoring forces. A payload is held by two or more blades so that it moves only in the vertical direction. The GAS blades are largely bent beyond the linear region, but they can be regarded as liner springs near their equilibrium point (working position). When the payload moves away (up or down) from the working position, the vertical component of the GAS spring force pulls it back to the equilibrium, while the vertical projection of the horizontal compressive force pushes it away. Those two forces are both proportional to the payload displacement. Therefore, the compressive force causes an anti-spring effect to reduce the effective vertical stiffness. The advantage of GAS is that it is able to hold a heavy (in the order of 100 kg) payload while keeping compact profile (about 10 cm) for a low-frequency spring. In prototype tests, we achieved about 200 mHz of resonant frequency by a purely passive GAS[3].

The equilibrium position of GAS drifts in the vertical direction due to the applied stress and temperature change. To minimize the effect of stress, GAS blades are made of Marval8 maraging steel alloy, which has a high shear strength (73 GPa). Also, the shape of the blades is designed so that the shear stress distributes uniformly along them. Thermal drift is dominated by the change of an elastic constant of the material. We observed a 0.5 mm/K drift in a prototype filter. In the stable environment of the Kamioka mine, less than 0.5 mm of drift is expected, and this is smaller than the nominal beam centering precision. The thermal drift causes a negligible change of the vertical resonant frequency.

All fundamental resonant frequencies in six degrees of freedom of a GAS filter can be tuned below 1 Hz, by suspending it with a single wire that is attached close to the level of the center of mass of the filter. Therefore, a GAS filter works as a-low frequency isolator in any direction. To obtain further attenuation, one can cascade filters (multiple stage isolation). Just like the IP, GAS isolation performance deviates from that of an ideal harmonic oscillator, due to the momentum of the inertia and internal resonances of the blades and suspension wires. According to experiments and theoretical models, the vertical isolation performance saturates at around 10 Hz at the level of -60 dB. In the horizontal direction, the first internal mode of the suspension wire is located around a few tens of Hz, which degrades the attenuation above this frequency.

17.3.2. SAS Control

Low-frequency resonances of the SAS mechanics need to be damped appropriately to minimize the residual motion of the optics for stable operation of the interferometer. For this purpose, an active damping system is implemented in SAS[4]. Since the IP has extremely small stiffness, all translational modes and some rotational modes of the suspended filters and mirror suspension recoil effectively to the IP. By detecting the IP motion induced by the recoil from the lower stages, and compensating it by applying external forces, the kinematic energy of those modes can be dissipated. By using accelerometers, one can control the motion of IP with respect to the inertial coordinates at AC frequencies (inertial damping). However, since accelerometers are insensitive at low frequencies, they are not suitable for drift suppression. For this reason, supplemental position sensors are introduced for DC positioning to maintain long term stability. This control scheme has been successfully demonstrated in our prototype experiment and in the VIRGO interferometer. Since the damping force is applied to the IP stage, no stringent noise reduction is required to actuators. Usual voice-coil actuators are suitable for their large range and capacity. In addition to the above-described local control for damping purpose, the SAS control needs to be inte-

*3 Recent development of AS with active (electric) anti-spring realized below 100 mHz resonant frequency.

*4 Other damping systems will be implemented in the mirror suspension subsystem. Some resonances in the subsystem do not recoil effectively to the IP, but those could be damped by the local damper.

grated with the global interferometer control. The low-frequency component of the interferometer control signal can be fed back to actuators at IP, the mirror suspension top stage, and mirror level. Especially, the IP resonant frequency is substantially lower than that of other modes, it is fairly easy to design a low-frequency servo (10 mHz to 100 mHz) at this level. Controlling the mirror position at the IP level reduces the range requirement to the interferometer length control in order to suppress inevitable control electronic noises.

17.4. History and Status of SAS R&D

The SAS project had been launched to develp a passive seismic attenuation system for the next-generation GW detectors, such as LCGT and Adv-LIGO, under the international collaboration between TAMA, LIGO and other institutions. The basic concept of SAS is based on the Super Attenuator for VIRGO interferometer, with substantial improvements in the mechanics and the control system. TAMA SAS, the SAS designed to fit into TAMA300 detector, has been studied since 2000. The critical components, such as the IP and the monolithic GAS filter, were developed and tested at the California Institute of Technology by 2001. Then, two prototype SAS towers were installed into the 3m Fabry-Perot cavity at the University of Tokyo to demonstrate their ability to maintain stable interferometer operation, together with their passive low-frequency attenuation properties and the active damping scheme was validated (figure 5). Following the prototype experiments, four towers are being installed into the TAMA300 detector starting in August 2005. This upgrade is aimed to improve the stability of the detector and its sensitivity at low frequencies. The SAS active control is implemented with a commercial digital controller, and it will be validated in TAMA[5]. The operation of SAS in the real scale interferometer is also a good opportunity to collect crucial information to finalize the design of SAS for LCGT.

17.5. LCGT SAS Performance in LCGT Sensitivity

The topology of the SAS designed for LCGT (LCGT SAS) is shown in figure 1. It consists of an IP, three cascaded monolithic GAS filters (filter0, filter1, filter2: from top to bottom), and a test mass suspension subsystem. The suspension subsystem is a triple pendulum that includes a mirror for a supplemental interferometer as well. The top stage of the suspension subsystem (suspension platform) is suspended from filter 2 via a single metal wire. There is a box that is collocated with the platform houses several coil-magnet actuators to control the platform position and orientation. The coil box is connected to the bottom filter via a rigid steel tube. The passive isolation performance of the LCGT SAS has been computed with a rigid-body model. In this model, the resonant frequencies of the IP and GAS filters are assumed as 30 mHz and 500 mHz, respectively. Including

*5 The prototype SAS and VIRGO SA are controlled with custom made VIRGO digital controllers.

Fig. 5. SAS prototype in the 3m Fabry-Perot cavity.

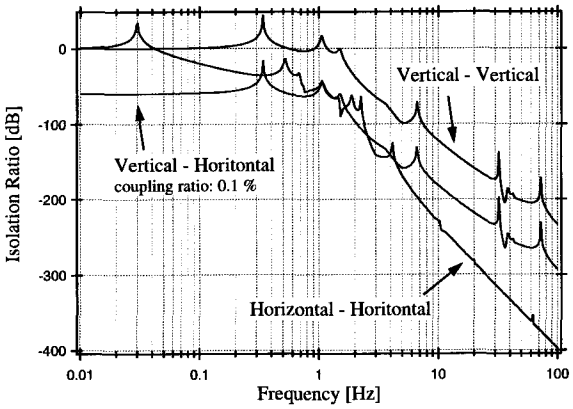

Fig. 6. Estimated transfer functions for LCGT SAS.

those resonant frequencies, all mechanical parameters are determined arbitrarily, and not optimized. The effect of the active damping is not taken into account. Figure 6 shows the computed transfer functions from ground to the test mass, in the horizontal-horizontal, vertical-vertical, and vertical-horizontal (cross-coupling) paths. The assumed cross-coupling ratio is 0.1%. Due to the isotropy of seismic motion, the vertical - horizontal cross-coupling dominates the mirror motion above a few Hz. Using the model transfer functions and the ground motion (equation (26)s), the LCGT test mass motion has been estimated and is shown with the other interferometer noises in figure 7. The plot shows that the estimated seismic noise is smaller than the radiation pressure noise below 10 Hz, with a safety margin of over 50. The margin depends on the cross-coupling ratio, and 0.1% is a relativly small assumption. An extra safety margin could be easily obtained by adding another stage of the GAS filter.

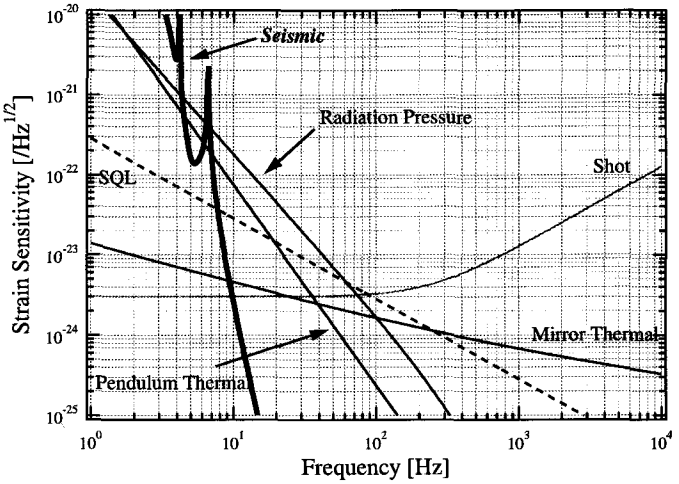

Fig. 7. Noise estimation for LCGT. Seismic noise (green) is derived from the computed transfer function (figure 6) and the seismic motion model.

17.6. Considerations for LCGT SAS

Although the techniques used in SAS ha been matured and fully validated in prototype interferometers, there are other issues that need to be considered to design the LCGT SAS.

17.6.1. Cryogenic and Vacuum Compatibility

For cooling efficiency, most of the SAS should be located at room temperature, and only the suspension subsystem including the suspension platform should be inside the 4.2 K radiation shield for easy installation and maintenance. The stage between the test mass and the platform is the mirror for the supplemental interferometer, and it is chilled by the heat link from the 4.2 K radiation shield. In order to attenuate the vibration transmitted from the radiation shield to the suspended mass, the heat link should be anchored to other isolated masses. For example, the heat link could be hooked to the reaction masses for the main and supplemental interferometer control, and to the suspension platform. The routing of the heat link should be decided by considering an acceptable level of the recoil mass motion and the vibration of the radiation shield. To reserve the cooling power, the heat link should be attached to those masses with adequate thermal insulators. The wire that connects the suspension platform to the filter 2 is the interface between the cryogenic and the room temperature parts. This wire needs to be in a material that has poor thermal conductivity. Maraging steel seems to be a suitable material because it has relatively low conductivity (about 25 W/m/K) for a metal, and has high tensile strength that allows small wire diameter (i.e. small thermal conductivity). The effect of a large thermal gradient in the wire may cause mechanical shot nois,e and it requires further study.

Most of the SAS is made of stainless steel, with some other steel alloys and insulators (either plastics or ceramics). Those materials are basically UHV compatible.

17.6.2. Other Considerations

Some protection to secure the optics from dropping is required. This could be done by implementing a 'catcher' that minimizes the distance of fall, as done in TAMA300. Since the laser power stored in the LCGT cavities is substantially high, it is also necessary to install baffles that protect the mirror suspension wires and a watchdog system that monitors large excitations of the test mass oscillation. The vacuum chambers and the cryogenic shieldings should be designed to allow easy access to SAS and the suepended optics for maintenance purpose.

Bibliography

[1] A. Takamori, PhD Thesis, University of Tokyo, (2002).

[2] G. Losurdo, PhD Thesis, Scuola Normale Superiore di Pisa (1998).

[3] A. Bertolini, PhD Thesis, Univrsita' di Pisa, (2000).

[4] G. Cella, R. DeSalvo, V. Sannibale, H. Tariq, N. Viboud, and A. Takamori, *Nucl. Instrum. Meth., A*, **487**, 652, (2002).

[5] M. Beccaria, *et al.*, *Nucl. Instrum. Meth., A*, **394**, 397, (1997).

[6] M. Barton, *et al.*, *LIGO Document*, **T990075-00**, (1999).

[7] A. Takamori, *et al.*, *LIGO Document*, **T000009-00**, (1999).

[8] G. Losurdo, *et al.*, *Rev. Sci. Instrum.*, **72**, 3653, (2001).

18. Data Processing

[Author: TATSUMI, Daisuke]

National Astronomical Observatory of Japan, Mitaka, Tokyo 181-8588

18.1. Overview

The data-processing system consists of the following systems as listed in Table 1. Figure 1 shows a schematic view of the data processing system.

The data-acquisition systems are completely independent of two interferometers of LCGT. The main data-acquisition system records the most important signals for GW detection. On the other hand, for detector-diagnosis and environmental monitoring, the data-acquisition stations (hereafter it is called DAQ station) record several signals that come from eight areas of our facility. The raw-data archive collects and stores the data from two interferometers. For GW signal searches, the data in an interest frequency region is extracted by a pre-analysis server and then is compressed for saving the storage volume. A correlation-analysis and a veto-analysis are computed on this server online. The time information system, the network and the firewall are required for the precise time information and data transfer. Finally, the data-analysis server is used for GW signal searches by LCGT collaborators. It has a huge computing power and has a role of interface between huge amount of data and many researchers.

`Main data-acquisition system`	2 sets
`Data-acquisition station`	16 sets
`Time information system`	1 set
`Pre-analysis server`	1 set
`Raw-data archive`	1 set
`Network / Fire-wall`	1 set
`Data-analysis server`	1 set

Table 1. Subsystems for Data-processing system.

18.2. Requirements and Current Status

The data-processing requires technical progresses to satisfy the several requirements for LCGT. We emphasize on key features by comparison to that of TAMA and evaluate their feasibility.

There are several requirements for the data-acquisition: wide dynamic range, fast sampling frequency and enough channels to record many signals.

The dynamic range of the signal is required to be wider than 120 dB. It corresponds to a 20-bit resolution of an analog-to-digital converter (ADC). A TAMA specification of 84 dB (14-bit resolution) had a potential for the first detection of GW signals. As for gravitational wave astronomy, it is important to measure the GW amplitudes more precisely. Therefore, the stricter requirement of 120 dB is necessary. The required sampling frequency can be satisfied by a 24-bit ADC with a 100 kHz sampling. However, the effective resolution of such ADC is limited by 20-bit or less. This will be improved further until the beginning of the LCGT operation. To collect a lot of signals, 16 sets of ADC and computers, which are called DAQ station, are placed on an appropriate location in a facility as illustrated in Fig. 1.

Parameterization	LCGT design	TAMA
Dynamic Range	$\geq$ 120 dB	84 dB
Sampling Rate	32768 Hz	20000 Hz
Number of Channels	32	8
	1024	64
	512	64

Table 2. Key requirements of the data-acquisition.

Parameterization	LCGT design	TAMA
Data Transfer Rate	40 MB/sec	0.36 MB/sec
	126.6 GB/hour	1 GB/hour
Hard Disk	$\geq$ 100 TB	5 TB
Media	$\geq$ 100 GB/tape	20 GB/tape

Table 3. Key requirements of the data-storage.

Due to increasing number of channels, a capability of data storage should be improved. The data storage is required to store data of over one-month. A minimum requirement is set to be 100 TB which corresponds to 800 hours of data. This requirement is archived by adopting RAID-disk clusters. Each RAID-disk will be applied a suitable RAID level (0, 5 or 5+1) to optimize the disk performance such as an access speed and/or redundancy.

Data-transfer rate of 40 MB/s, which is by 100 times faster than that of TAMA, is also required. Recent technologies provides a sufficient speed for disk access, disk interface and network. For example, Ultra ATA/133 disk can transfer data with 133 MB/sec in principle. In the year of 2007, a new specification of 750 MB/s will be available. The disk-interface also has several choices: Fiber Channel and Ultra 320 SCSI have a data-transfer rate of 200 and 320 MB/s, respectively. About network (internet), we discuss later.

Although the disk space will be more than 100 TB, it is insufficient to store all data from several years' observation. Therefore, the data need to be duplicated to appropriate tape media. In TAMA, DLT tapes of 20 GB (in no

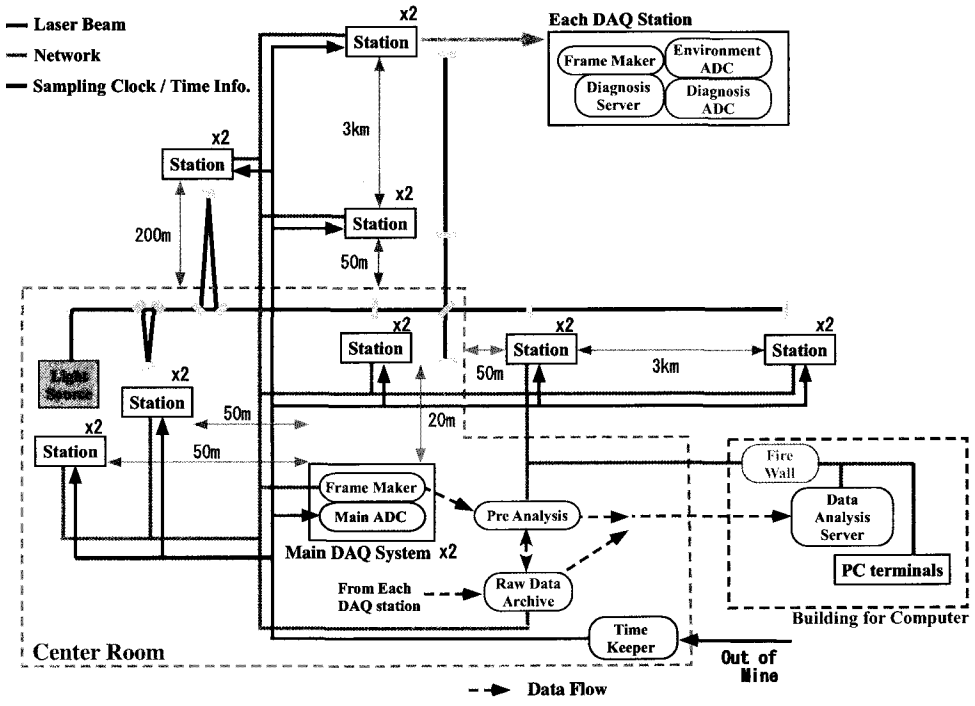

Fig. 1. Schematic View of Data Processing System

compression mode) have been used. However, this tape capacity is insufficient, since LCGT makes over 120 GB of data per hour. It corresponds to continuously spending 6 tapes per hour. It is very difficult to handle or manage such a huge number of tapes. Super DLT600 and LTO Ultrium 3 are available for LCGT and have a capability of 300 and 400 GB/tape in no compression mode. They allow us to handle only several tapes per day. Higher capacity tapes are anticipated with a reasonable cost in a few years.

Parameterization	LCGT design	TAMA
Time Resolution	≤ 0.01 μsec	0.01 μsec
Signal	10 MHz IRIG-B123 1 PPS	10 MHz IRIG-B123
Distance	≤ 5 km	10 m

Table 4. Key requirements of time-information system

The time-information system comprises the global positioning system (GPS) and sampling clock generators as used in TAMA. There are two differences between TAMA and LCGT. One is that each DAQ system should be synchronized, since we need several DAQ stations to record many signals. The other is that precise time information should be transferred into the mine and should be distributed to each DAQ station.

To synchronize the sampling clocks, a reference clock of 1 PPS (pulse per second) is used from a GPS receiver. Each clock of different sampling frequency can be synchronized by the timing of 1 PPS signal. By choosing a file length to be 1 second or its integral multiple, it is easy to combine data files of different sampling clock in this scheme.

To obtain time information in the mine, it is important that the signal transfer of long distance together with keeping precise timing. By comparison with several schemes of the transmission, a GPS antenna extension system is adopted to connect the GPS antenna and the GPS receiver. It consists of a down-converter at the GPS antenna and an up-converter at the RF input of the GPS receiver. To provide high fidelity signal-transmission, the converter pair is in phase-locked. This technique uses the identical reference for up and down conversion, which eliminates a frequency error. By using a fiber optics, it has a transmission distance of 8 km at the maximum. Each GPS receiver, which is located at nine areas (one for the main DAQ system and eight for DAQ stations) in the site, supplies sampling clocks, 1 PPS signals, and time encoded signals of IRIG-B123.

Parameterization	LCGT design	TAMA
Transfer Rate		
within Firewall	≥ 1 Gbps	10 Mbps
over Firewall	≥ 100 Mbps	1 Mbps
Internet Connection	Super-SINET	Super-SINET

Table 5. Key requirements of network / firewall.

The network infrastructure should have a capability of high data transfer rate of more than 1 Gbps. In TAMA, an effective transfer rate of 10 Mbps was available by introducing gaga-bit Ethernet technology. The technology of such a high-speed internet connection is well established by Super-SINET (Science Information Network) of Japan. The global network has a speed of 10 Gbps and is used for the data distribution to TAMA collaborators. Within a few years, Kamioka observatory of ICRR will be connected to the Super-SINET.

Parameterization	LCGT design	TAMA
Pre-Analysis	200 GFLOPS	5 GFLOPS
Data Analysis	1 TFLOPS	60 GFLOPS

Table 6. Key requirements of computing power.

The pre-analysis server makes pre-processed data for each GW search. The computing power needs more than 200 GFLOPS [6]. Some correlation analysis between noises and online veto analysis, which are well studied in TAMA, are also processed in this server. Even for personal computer, its computing power is more than 1 GFLOPS. Beowulf cluster can easily satisfy such requirement.

For the main data-analysis server, a required computing power is estimated to be 1 TFLOPS. This server is mainly used for GW search of inspiraling compact star binary. The search is assumed to be independent for each detector, and covers mass-region from 0.8 to 100 $M_{\odot}$. Because it takes 0.94 TFLOPS at the maximum, we set the minimum requirement to be 1 TFLOPS. One of the highest computing power machine is an Earth simulator of Japan and has 35.8 TFLOPS: as of June 2005, Blue Gene has the world best record of 136.8 TFLOPS. There is no technical problem to obtain a computer of 1 TFLOPS.

When we need more computing power to search wider mass-region and to search another GW sources, a GRID computing technology can be employed. Its studies are in progress by researchers of High Energy Accelerator Research Organization (KEK), National Institute of Advanced Industrial Science and Technology (AIST) and University of Tokyo in Japan. In collaboration with these groups, we will be able to obtain more powerful computing capability in future.

18.3. Summary

All requirements for the data processing are available with the current technology. Future progress of technologies will make cost reduction or give us more redundant system.

*6 FLOPS: Floating point number Operations Per Second

19. Time Schedule of Program

LCGT is to be constructed in 5 years, and 2 years commissioning is planed. Table 1 gives time schedule for each part of LCGT along with the estimated budget. We consider an important limiting factor of the time schedule for each part. Tunnel-digging determines the time span of the construction, because the whole two years should be devoted due to work in the limited space of the tunnel. After tunnel construction with wall-painting and floor-furnishing is finished, the vacuum system will be introduced. The building housing the computer system for data-taking outside of the tunnel can be independently constructed from the tunnel digging. The production speed of the vacuum ducts does not limit the time schedule according to the high capacity of the production facility of a company. In place of production, the limited capacity of transportation should be considered for the construction of the vacuum system. This is because the access road to the entrance of the tunnel is narrow, and we have snow in the winter season. The facility is to be completed in 4 years, and the optical system will be installed in the last year.

Our planned 5-year construction with 2 years commissioning is reasonable based on the experience of TAMA.

Item	2006	2007	2008	2009	2010	2011	2012	Cost (Thousand Yen)
Tunnel	$\Longrightarrow$	$\Longrightarrow$	$\Rightarrow$					3,396,000
Buildings		$\Longrightarrow$	$\Rightarrow$					500,000
Vacuum	$\longrightarrow$	$\longrightarrow$	$\rightarrow\Rightarrow$	$\Rightarrow$				5,250,000
Optics	$\longrightarrow$	$\longrightarrow$	$\longrightarrow$	$\rightarrow\Rightarrow$	$\Rightarrow$			925,420
Laser	$\longrightarrow$	$\longrightarrow$	$\longrightarrow$	$\Rightarrow$				802,780
Cryo-Suspension	$\longrightarrow$	$\longrightarrow$	$\longrightarrow$	$\Rightarrow$				2,630,000
Anti-vibration	$\longrightarrow$	$\longrightarrow$	$\longrightarrow$	$\Rightarrow$				230,000
Main Mirror	$\longrightarrow$	$\longrightarrow$	$\longrightarrow$	$\longrightarrow$	$\Rightarrow$Install			300,000
Data-taking			$\longrightarrow$	$\longrightarrow$	$\Rightarrow$Install			200,000
Observation						$\Longrightarrow$	$\Longrightarrow$	600,000
							Total	14,834,2000

Table 1. Construction Schedule of LCGT. 5-year construction with 2 years commissioning is reasonable by the experience of TAMA. The symbol ($\Longrightarrow$) represents the installation work at the tunnel site and the symbol ($\longrightarrow$) means the work including R&D at other places than the tunnel site.

20. Manpower Organization

The LCGT project is formed by many researchers who belong to many different organizations and universities. Among these organizations, the directors of ICRR, NAOJ, and KEK made a MOU in 1994 to promote research for the detection of gravitational waves. The research community of gravitational waves that was originally loosely connected formed a unified solid collaboration at the beginning of the TAMA project. After TAMA, new people have joined to form the LCGT collaboration. Any experimental researcher who is actively conducting gravitational wave experiment in Japan belongs to the LCGT collaboration at this time. MOU has been revised every two years, and in the most recent revision, the director of NAOJ has agreed to transfer the manpower of NAOJ to ICRR at the time of budget approval, and the director of KEK made a promise to support LCGT in the sense of manpower. Figure 1 shows the organization chart for the construction of LCGT. The technical advisory committee is conceived to be a permanent advisory board of LCGT at the time when its funding is approved.

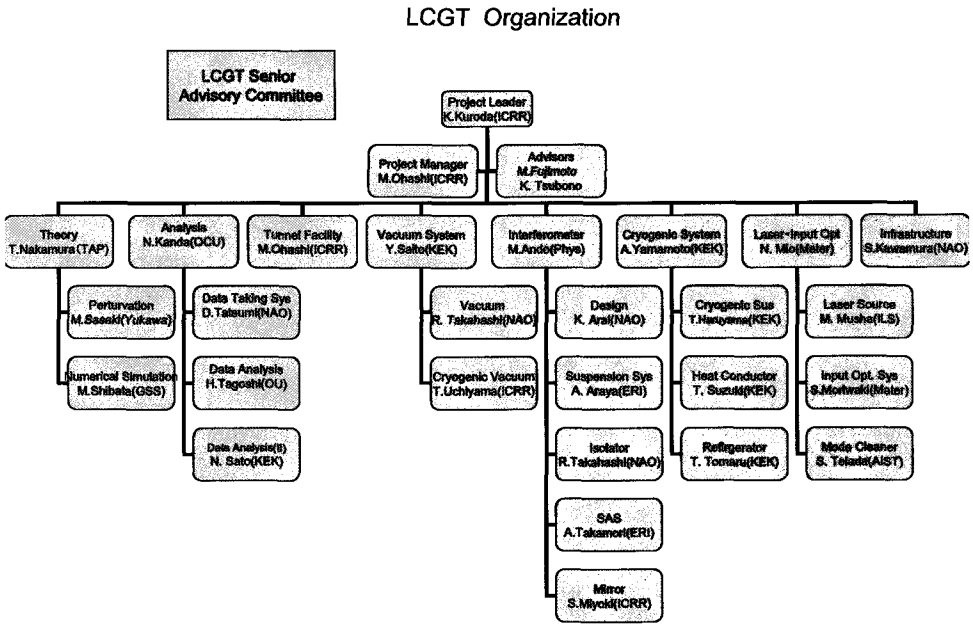

Fig. 1. Manpower organization of LCGT. All researchers listed here are permanent staff belonging to various organizations or institutes. Permanent staffs mean that they are responsible for making contracts with companies. The abbreviations are as follows: TAP, Theoretical Astrophysics Group (Department of Physics)Kyoto U, Yukawa, Yukawa Institute (Kyoto U), GSS, Department of General System Study (Graduate school /College of Arts and Sciences)UT, OU, Osaka University, OCU, Osaka City University, ERI, Earth Quake Research Institute(UT), Phys, Department of Physics (School of Science)UT, ILS, Laser Science Center (University of Electro-Communications), Mater, Department of advanced material sciences (Graduate school of Frontier Sciences) UT, AIST, National Institute of advanced industrial Science and Technology.

The staff members presented in Table 1 are not sufficient to proceed the construction of LCGT. Figure 2 shows how we plan to hire pos-doc people each year. We recognize that the above manpower is the minimum body necessary for constructing, managing and maintaining the LCGT facility.

Man power plan: Left; Permanent staff, right; PD, ( ) existing number

Year	Infra		Tunnel		Vacuum		Optics		Laser		Mirror		Suspension		Isolator		Data		Analysis		Staff	PD
	NAO		ICRR		KEK(NAO)		Phys(ICRR)		Mater		ICRR		ICRR(KEK)		ERI		NAO		OCU(OSA)		in total	in total
1	0	0	1 (1)	0	2 (2)	1	8 (2)	4	1 (1)	1	1 (1)	1	6 (5)	2	2 (2)	1	2 (2)	2	5 (2)	5	25 (18)	12
2	0	0	1 (1)	0	2 (2)	1	4 (2)	4	1 (1)	2	2 (1)	1	7 (5)	4	2 (2)	1	2 (2)	2	5 (2)	5	26 (18)	15
3	0	0	1 (1)	0	2 (2)	1	4 (2)	8	1 (1)	2	2 (1)	1	7 (5)	5	2 (2)	3	2 (2)	2	6 (2)	15	27 (18)	37
4	1 (1)	0	1 (1)	0	2 (2)	1	6 (2)	16	1 (1)	3	1 (1)	1	7 (5)	5	2 (2)	3	3 (2)	4	8 (2)	18	32 (19)	41
5	2 (2)	0	1 (1)	0	0	1	6 (2)	16	1 (1)	5	1 (1)	1	7 (5)	2	2 (2)	3	3 (2)	4	8 (2)	20	31 (18)	35
6	2 (2)	0	1 (1)	0	0	1	4 (2)	4	0	1	0	0	2 (5)	1	1 (2)	1	3 (3)	2	18 (3)	13	31 (18)	23
7	2 (2)	0	1 (1)	0	0	1	4 (2)	4	0	1	0	0	2 (5)	1	1 (2)	1	3 (3)	2	18 (3)	17	31 (18)	27

Fig. 2. We plan to hire pos-doc people each year.

21. Collaboration with other groups

During TAMA construction, we made several research agreements with LIGO, VIRGO, GEO and ACIGA. LCGT succeeds all of these agreements, and has been revised to make stronger collaborative research.

22. Appendix

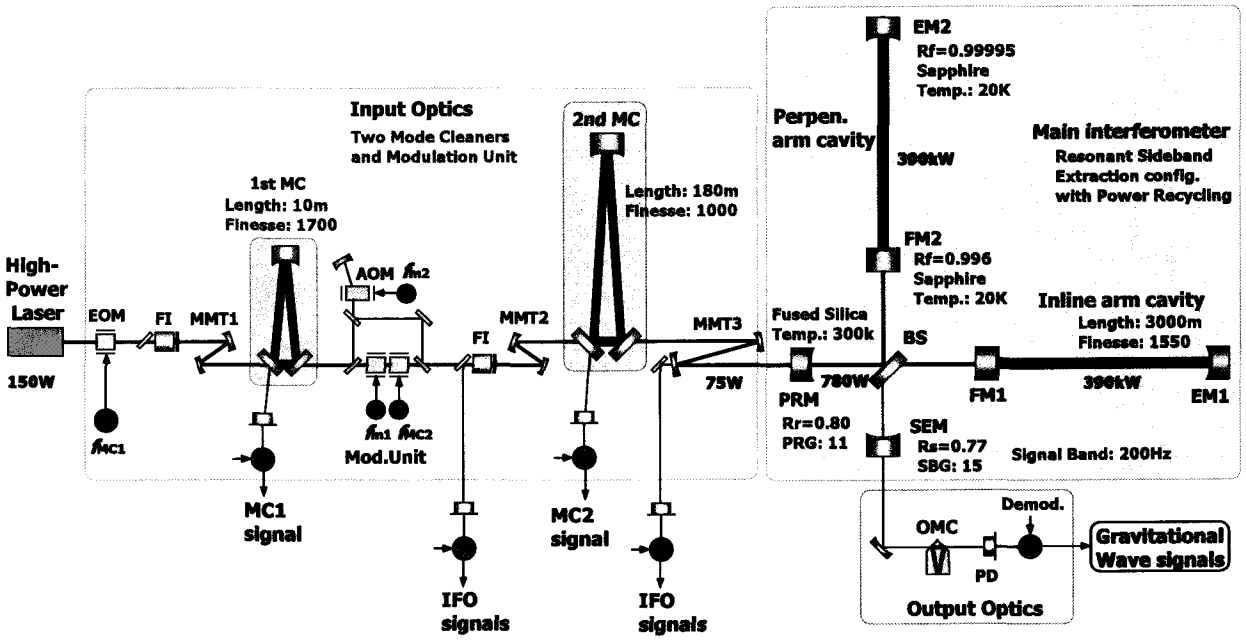

Fig. 1. Optical layout of one interferometer of LCGT including the main interferometer part, the laser source, the input optics, and the output optics.

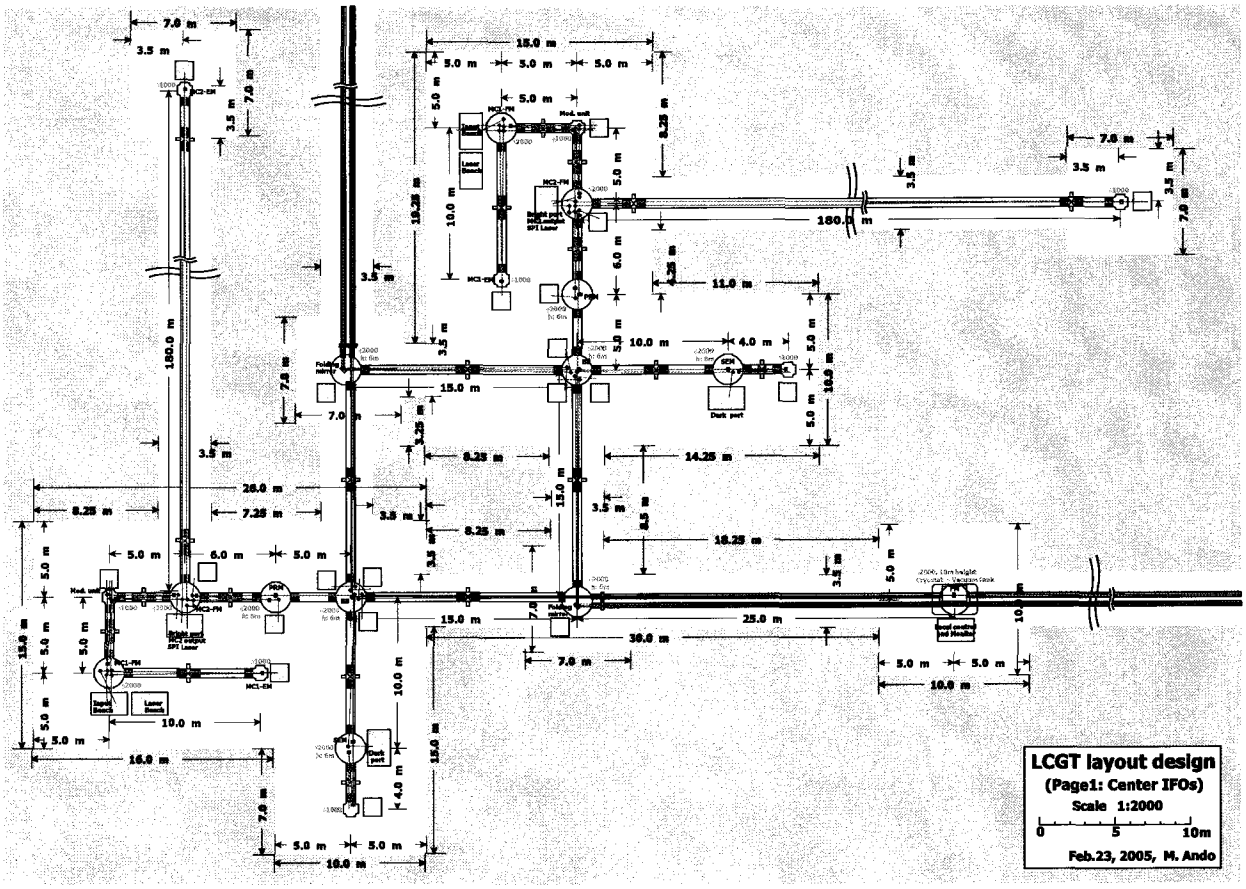

Fig. 2. Layout of optical pieces in the center room of LCGT.

	TAMA Achieved	TAMA Design	LCGT Requirement
1.1			
1.1 Output Power	9.5 W	10 W	150 W
1.2 Power of Radiation Pressure	12 kW Photon Pressure	10 kW Photon Pressure	400 kW Photon Pressure
1.3 Frequency/Phase Noise	10^4/f Hz/rHz(Free Run) 5×10^[-5] Hz/rHz(Stabilized)	5×10^[-6] Hz/rHz	3.9×10^[-8] Hz/rHz@100Hz(Stabilized)
1.4 Intensity Noise	10^-5/f^(1/5) 1/rHz(Free Run) 3×10^[-8] /rHz(Stabilized)	10^[-8] /rHz	1.8×10^[-8] /rHz@100Hz(Stabilized)
1.5 Beam Jitter	0.19mm_EM	0.5mm rms @EM	TBD
2			
2.1 Gain	4.2	10	10
2.2 Noise added by Recycling	Intensity noise by gain change	Effect resulting from RM control	Must be negligible
2.3 Stability	0.3%rms	Less than 10%	2.5×10^[-8] Hz/rHz
3			
3.1 Beam Direction	(Stabilized) 3×10^[-12] m/rHz at 20Hz 、1×10^[-17] m/rHz at 100Hz	(Original) 2×10^[-7] m/rHz at 20Hz、1×10^[-11] m/rHz at 100Hz 、 1×10^[-13] m/rHz @1000Hz、 (Stabilized) 1×10^[-16] m/rHz at 20Hz、	3×10^[-9] @20Hz
3.2 Other directions	the same as the beam direction	the same as the beam direction	3×10^[-7] @20Hz
3.3 Couplings	1/10(mainly due to the stack)	1/100	10^[-2]
3.4 Newtonian Noise	3×10^[-18] m/rHz@20Hz	3×10^[-18] m/rHz@20Hz	3×10^[-18] m/rHz@20Hz
3.5 Actuator Noise	Designed to be free	Free from Earth magnetism	Less than what is estimated along the beam axis
3.6 Long period Seismic Noise	100μm	10μm(without active isol)	Needed a wide dynamic range
4			
4.1 Roughness	1.794nm_rms (The objective of TAMA is achievable by simulation)		0.3nm
4.2 Form factor	P(f)=10^(-22)*f^(-1.75) (The objective of TAMA is achievable by simulation)		P(f)=10^(-22)*f^(-1.75) Simulation needed
4.2a Thermal Deformation	Negligible	Negligible	0.1¥pm0.02% for unifrom deformation
4.3 Accuracy of form factor	λ/40(Zygo GPI-XP/HR)		
4.4 Energy dissipation	Substrate Absorption a few ppm/cm Coating absorption 0.1ppm Coating scattering 30ppm (5ppm for the region of diameter less than 1mm)	*Substrate Absorption a few ppm/cm. Coating* Absorption less than 50ppm	Substrate Absorption 20ppm/cm Coating Absorption 0.1ppm Coating Scattering less than 10ppm
4.5 Quality of Substrate	Suprasil-P10 (Shinetsu Co. Ltd)	Synthetic Silica	
Impurity	1ppm		Less than 1ppm
Bubbles	Bubble grade O(DIN58927)		Not detectable
Imhomogeneity	Striae Free for all direction		0.2ppm for each axis
Birefringence	complex reflectivity 2nm/cm		Less than 50ppm/cm
4.6 Q-values			
Without actuators nor suspension	3x10^6	10^6	More than 10^{8}
With actuators and suspension	10^5	10^5	10^{8}
4.7 Heat Flow (Cryogenic Mirror)	1.38 W/m/K		500mW (400mW internally)
4.8 Thermal Deformation	Thermal Lensing		TBD
4.8a Deformation(Cryogenic Mirror)	Curvature shrinks by 0.1%		Curvature change should be less than 0.1%
4.9 Deterioration with time	Less than 1ppm/month at atmospheric pressure		0.024ppm/day at cryoigenic temperature for 30cm diameter, 20m length radiation shield in 10^-6 Pa, which degrades Recycling Gain by 10% for a year.
Deterioration of coating		None	Neglible compared with cryogenic deposition, None
4.10 Spatial dependence of Finesse	Reflectivity of 4N mirror is σ=8ppm(5mmX5mm)	Less than 10ppm	Reflectivity should be less than 8ppm/5mm^2

Fig. 3. Technical Requirements of LCGT (Laser, Recycling, Seismic Noise, and Mirror &Coating)

	TAMA Achieved	TAMA Design	LCGT Requirement
5 Thermal Noise			
5.1 Mirror	6×10^[−20] m/rHz@300Hz		4.8×10^[−21] m/rHz@100Hz
5.1a Thermoelastic Noise	1.8×10^[−21] m/rHz@300Hz		2.8×10^[−21] m/rHz@100Hz
5.2 Coating	9×10^[−20] m/rHz@300Hz		3.9×10^[−21] m/rHz@100Hz
5.3 Suspension			
5.3.1 Pendulum mode	2.1×10^[−20] m/rHz@300Hz		2×10^[−19] m/rHz@10Hz
5.3.2 Vertical vibration modes	10^[−22] m/rHz以下		1.2×10^[−21] m/rHz@10Hz
5.3.3 Violin modes	The lowest frequency > 500Hz		The loweset frequency ＞100Hz
5.4 Through actuators	4×10^[−22] m/rHz@300Hz		6×10^[−21] m/rHz@100Hz
6 Vacuum			
6.1 Time scale of ecvacuation	300 hr @ 10^[−5]Pa	150 hr @ 10^[−5]Pa	Equivalent to TAMA
6.2 Leakage	2×10^[−9] Pa･l/s	Less than measurable limit	Less than measurable limit
6.3 Attainable vacuum	2×10^[−6] Pa	1×10^[−6] Pa	2×10^[−7] Pa
6.4 Dust	Not detected	None	None
6.5 Carbonate	not detected at (<10^[−8]Pa)	None at measurable limit	Equivalent to the design of TAMA
6.6 Residual gas composition	H2O 7.1×10^[−6] Pa	Less than 10^[−5] Pa in total	Equivalent to the design of TAMA
6.7 Refractive index noise by residual ga	Measured by Xe	Less than 1×10^[−21] m/rHz	Less than 1×10^[−21] m/rHz
6.8 Continuous gas release	1×10^[−8] Pa m^3/(sm^2)	1×10^[−8] Pa m^3/(sm^2)	Equivalent to the design of TAMA
6.9 Abrupt gas release	10^[−4] Pa･hour/1month	None at measurable limit	None at measurable limit
7 Control			
7.1 Servo gain	10^8(f<1Hz), UGF=1kHz	10^8(f<1Hz), UGF=1kHz	10^8(f<1Hz), UGF=1kHz
7.2 Length control	4 degrees of freedom(L−, L+, l−, l+) (differencial) Magnet-Coil force, Thermal Control (In phase) Laser frequency, magnet-coil force, thermal control	4 degrees of freedom(L−, L+, l−, l+) (differencial) Magnet-Coil force, PZT (In phase) Laser Frequency, Magnet-Coil force, PZT	5 degrees of freedom(L−, L+, l−, l+, ls) (differencial) Magnet-Coil force, Thermal Control, PZT (In Phase) Laser Frequency, Magnet-Coil force, Thermal Control, PZT
7.3 Control of other degrees of freedom	Alignment Control (10 degrees of freedom) −Magnet-Coil force Correction of beam centering for alignment Length control for Perpendicular FP arm(2 degrees of freedom)	Alignment Control (10 degrees of freedom) −Magnet-Coil force Length control for Perpendicular FP arm(2 degrees of freedom)	Alignment Control(12 degrees of freedom) −Magnet-Coil force, PZT Length control for Perpendicular FP arm(2 degrees of freedom)
7.4 Distorsion from Gaussian	M^2=1.01(1.47in)	M^2 nearly equal to 1	M^2 nearly equal to 1
7.5 Stability	24hrContinuous operation without power recycling, 8hr operation with power recycling 90% running efficiency achieved at DT6. 120hr continuous operation, running efficiency more than 99% by LISM at Kamioka		24 hr continuous operation Running efficiency more than 90%
8 Detector			
8.1 Number of photo detectors	4 for Dark Port	4 for Dark Port	4−32
8.2 Equivalent Thermal noise	100mK		TBD
9 Others			
9.1 AC/EM interference			
9.2 Cosmic Ray	Under estimati0on		Under Estimation
9.3 Sound	Monitored result applicable to coincidence analysis		Monitored result applicable to coincidence analysis

Fig. 4. Technical Requirements of LCGT (Thermal Noise, Vacuum, Interferometer, and Detector)